

AD A119296

HDL-TR-1978

AUGUST 1982

Calculations of Second Breakdown in Silicon Diodes

by Alford L. Ward

BEST
AVAILABLE COPY



U.S. Army Electronics Research
and Development Command
Harry Diamond Laboratories
Adelphi, MD 20783

DIS. FILE COPY

Approved for public release; distribution unlimited.



SEP 16 1982



SEP 16 1982

**BEST
AVAILABLE COPY**

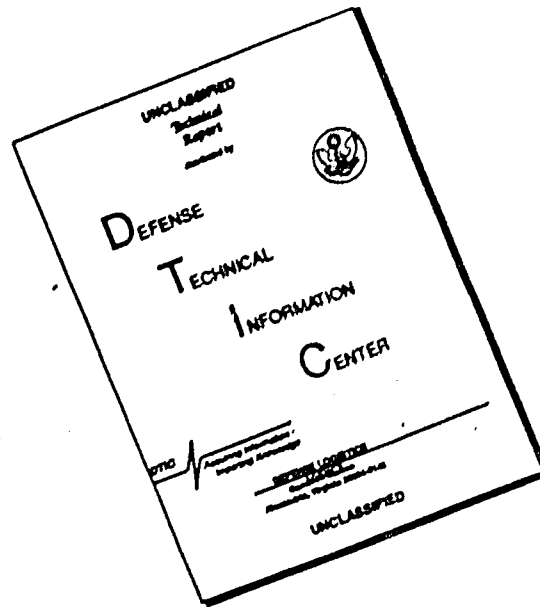
The findings of this report are not to be construed as an official
statement of the Army, and are subject to disavowal by other
authorized documents.

Reproduction of this report is prohibited without the express
written consent of the Army, and is prohibited by law.

Destroy this report when it is no longer needed. Do not return
it to the originator.

**BEST
AVAILABLE COPY**

DISCLAIMER NOTICE



THIS DOCUMENT IS BEST QUALITY AVAILABLE. THE COPY FURNISHED TO DTIC CONTAINED A SIGNIFICANT NUMBER OF PAGES WHICH DO NOT REPRODUCE LEGIBLY.

UNCLASSIFIED

SECURITY CLASSIFICATION OF THIS PAGE (When Data Entered)

REPORT DOCUMENTATION PAGE		READ INSTRUCTIONS BEFORE COMPLETING FORM
1. REPORT NUMBER HDL-TR-1978	2. GOVT ACCESSION NO. AD-A19296	3. RECIPIENT'S CATALOG NUMBER
4. TITLE (and Subtitle) Calculations of Second Breakdown in Silicon Diodes		5. TYPE OF REPORT & PERIOD COVERED Technical Report
		6. PERFORMING ORG. REPORT NUMBER
7. AUTHOR(s) Alford L. Ward		8. CONTRACT OR GRANT NUMBER(s)
9. PERFORMING ORGANIZATION NAME AND ADDRESS Harry Diamond Laboratories 2800 Powder Mill Road Adelphi, MD 20783		10. PROGRAM ELEMENT, PROJECT, TASK AREA & WORK UNIT NUMBERS Program Ele.: 62120 DA Project: 1L162120AH25
11. CONTROLLING OFFICE NAME AND ADDRESS U.S. Army Materiel Development and Readiness Command Alexandria, VA 22333		12. REPORT DATE August 1982
		13. NUMBER OF PAGES 129
14. MONITORING AGENCY NAME & ADDRESS (if different from Controlling Office)		15. SECURITY CLASS. (of this report) UNCLASSIFIED
		15a. DECLASSIFICATION/DOWNGRADING SCHEDULE
16. DISTRIBUTION STATEMENT (of this Report) Approved for public release; distribution unlimited.		
17. DISTRIBUTION STATEMENT (of the abstract entered in Block 20, if different from Report)		
18. SUPPLEMENTARY NOTES HDL Project: X750M0 DRCMS Code: 612120H250011 PRON: 1FOR0012011FA9		
19. KEY WORDS (Continue on reverse side if necessary and identify by block number) Second breakdown Silicon diode Diode switching Electrothermal model Space charge Negative resistance Avalanche Thermal injection Ionizing radiation		
20. ABSTRACT (Continue on reverse side if necessary and identify by block number) An electrothermal model computer program is described and used to study the basic physical mechanisms that initiate second breakdown. It is shown that space charge in the reverse-biased diode causes a negative resistance to develop, which in turn leads to filamentation and damage. Various doping profiles are studied. Thermal injection currents are shown to be important for time greater than the thermal time constant. High forward currents and		

DD FORM 1473
1 JAN 73

EDITION OF 1 NOV 65 IS OBSOLETE

UNCLASSIFIED

1 SECURITY CLASSIFICATION OF THIS PAGE (When Data Entered)

UNCLASSIFIED

SECURITY CLASSIFICATION OF THIS PAGE(When Data Entered)

20. Abstract (cont'd)

reverse switching into avalanche are calculated. The effects of ionizing radiation are presented. The analogy of the stages of second breakdown with glow and arc discharges in gases is found to be useful.

Accession For	
NTIS	<input checked="" type="checkbox"/>
DTIC	<input type="checkbox"/>
Other Agency	<input type="checkbox"/>
Availability Codes	
Avail and/or, OF	
File #	
DTIC	
COPY	
2	

UNCLASSIFIED

2 SECURITY CLASSIFICATION OF THIS PAGE(When Data Entered)

CONTENTS

	<u>Page</u>
1. INTRODUCTION	13
2. FORMULATION OF COMPUTER PROGRAM	14
2.1 Basic Equations	14
2.2 Supplementary Equations	15
3. MATERIAL PARAMETERS FOR SILICON	18
4. PROCEDURES AND DISCUSSION	21
5. TYPICAL REVERSE-BIAS STATIC CHARACTERISTICS	25
5.1 Current Regimes	26
5.2 Diode Profiles	28
6. DYNAMIC CHARACTERISTICS	32
6.1 Constant dV/dt	32
6.2 Constant Overvoltage	34
7. TEMPERATURE DEPENDENCE	34
7.1 Isothermal Calculations	34
7.2 Accuracy of Isothermal Calculation	37
7.3 Silicon-on-Sapphire Diode	38
8. THERMAL INJECTION CURRENTS	40
8.1 Initial Discussion	40
8.2 Calculations of Thermal Injection Currents	42
9. VARIATION OF DIODE WIDTHS AND DOPING DENSITIES	46
9.1 Varying Doping Densities	46
9.2 Varying Widths	48
9.3 Whole Families	49
10. DIFFERING DOPING PROFILES	52
10.1 One-Sided Diodes	53
10.2 Two-Sided Diodes	55
10.3 Linearly Graded Diodes	56
10.4 Other Doping Profiles and Discussion	57

CONTENTS (Cont'd)

	<u>Page</u>
11. EXTENDING THE TIME SCALE	58
11.1 Procedure	58
11.2 Simulation of 1N4148	59
12. IONIZING RADIATION	66
12.1 Two Examples	66
12.2 Discussion	68
13. DISCUSSION OF NEGATIVE RESISTANCE	70
14. AVALANCHE OSCILLATIONS	71
14.1 Background	71
14.2 Calculations	72
14.3 Experimental Measurements	81
15. FORWARD BIAS CHARACTERISTICS	87
15.1 Zero Current	87
15.2 Static Characteristics	90
16. REVERSE SWITCHING TRANSIENTS	98
16.1 Low-Voltage Switching	98
16.2 Switching into Avalanche	99
17. FURTHER DISCUSSION	102
18. SUMMARY AND RECOMMENDATIONS	107
18.1 Summary	107
18.2 Recommendations	108
ACKNOWLEDGEMENTS	109
LITERATURE CITED	111
SYMBOLS AND ACRONYMS	115
DISTRIBUTION	119

FIGURES

	<u>Page</u>
1. Temperature variation of electron and hole velocities as function of electric field	20
2. Punch-through factor defined	24
3. Typical variation of resistivity with temperature	25
4. Static current density versus voltage characteristic for 4- μ m N-type diode doped to $5 \times 10^{15} \text{ cm}^{-3}$	27
5. Current density as function of overvoltage for various assumed breakdown voltages, V_{B1}	27
6. Distribution of number density for diode of figure 4	29
7. Field distributions corresponding to current densities in figure 6	29
8. Distribution of ionization rates across N-type diode	29
9. Maximum ionization rates as function of current density	30
10. Integrals of α , β , and $\alpha\beta$ across diode as function of current density for P-type diode; dynamic characteristic of diode	30
11. Static current density versus voltage characteristic for P-type diode	31
12. Characteristic for diode with PTF = 1	31
13. Dynamic characteristics calculated with labeled rates of voltage rise compared with calculated static characteristic	32
14. Variation of voltage with time for diode of figure 13	32
15. Log-log plots of excess voltage and current as function of dV/dt for diode of figure 13	33
16. Excess voltage plotted as function of dV/dt for N-type diode	33
17. Log-log plot of time to breakdown versus overvoltage for P-type diode	34
18. Dynamic characteristics of P-type diode of figure 13 at different temperatures	35

FIGURES (Cont'd)

	<u>Page</u>
19. Change of dynamic characteristics with temperature for 10- μm diode doped to $N = 4 \times 10^{15} \text{ cm}^{-3}$	36
20. Rate of temperature rise for silicon diodes as function of current density	36
21. Plot of overvoltage as function of rate of rise of applied voltage	37
22. Variation of field profiles with temperature distribution	38
23. Measured and calculated current-voltage characteristics for silicon-on-sapphire diode with temperature (K) as parameter	39
24. Assumed variation of J_0 with temperature	41
25. Calculated dynamic characteristics for 4- μm P-type and N-type diodes, each doped to $5 \times 10^{14} \text{ cm}^{-3}$	43
26. Characteristics for diode of figure 25(a) with bulk temperature (K) as parameter	44
27. Second breakdown voltage as function of temperature for diode of figure 26	44
28. Calculated dynamic characteristics for 4- μm P-type diode, doped to $5 \times 10^{15} \text{ cm}^{-3}$, as function of J_0	45
29. Plots of V_{B2} for 4- μm diodes as function of J_0	45
30. Second breakdown voltages for diode of figure 28 as function of temperature	46
31. Characteristics of 4- μm P-type diode with doping level in cm^{-3} as parameter	47
32. Distributions of electric field across diode of figure 31	47
33. Field distributions across $P = 2 \times 10^{16} \text{ cm}^{-3}$ diode for various current densities	48
34. Characteristics of N-type diodes doped to $3 \times 10^{15} \text{ cm}^{-3}$	48
35. Field distributions across $3 \times 10^{15} \text{ cm}^{-3}$ diodes of various widths of figure 34 at low current densities	49

FIGURES (Cont'd)

	<u>Page</u>
36. First and second breakdown voltages as function of doping density	50
37. Comparison of measured and calculated V_{B1} variation with doping density	50
38. Same breakdown data as figure 36, but plotted against diode width and with doping density as parameter	51
39. First breakdown voltages plotted as parameter for variations in both diode width and doping density	51
40. Calculated V_{B1} as function of doping density for various diode widths, from equations (33) and (34)	52
41. Maximum field at breakdown as function of doping density	52
42. Calculated characteristics for abrupt one-sided diodes	53
43. Carrier densities for N-type diode of figure 42	53
44. Field distributions corresponding to carrier profiles of figure 43	54
45. Field distributions for P-type diode which is complementary to diode of figure 44	54
46. Characteristics of symmetric two-sided diodes doped to $1 \times 10^{17} \text{ cm}^{-3}$ for four diode widths	55
47. Carrier densities for symmetric two-sided diode doped to $1 \times 10^{17} \text{ cm}^{-3}$ showing doping profile, electron densities, and hole densities	56
48. Field distribution corresponding to densities of figure 47 ...	56
49. Characteristics of three families of linearly graded diodes ..	57
50. Carrier densities for 5- μm diode with linear doping gradient of $1 \times 10^{20} \text{ cm}^{-4}$	57
51. Field distributions corresponding to current densities of figure 50	57
52. Method of obtaining current and voltage versus time curves from static characteristics	60

FIGURES (Cont'd)

	<u>Page</u>
53. Power to breakdown versus breakdown time for diode of figure 52	61
54. Calculated static characteristic for 12- μ m N-type diode doped to $3 \times 10^{15} \text{ cm}^{-3}$, simulating 1N4148	62
55. Derivation of current versus time and voltage versus time for 1N4148	63
56. Thermal time constants and thermal resistance of silicon as function of distance	64
57. Comparison of calculated and experimental breakdown power for 1N4148 diode	65
58. Comparison of calculated and measured breakdown currents for 1N4148 diode	66
59. Calculated characteristics of 4- μ m N-type diode doped to $5 \times 10^{14} \text{ cm}^{-3}$ with ionizing radiation as parameter	67
60. Current and voltage as function of time for half-cycle sinusoidal applied voltage pulse shown	67
61. Calculated current, voltage, and power for same diode with $V_a = 120 \text{ V}$ and exposed to ionizing radiation pulse described in text	68
62. Illustration of diode stability in negative differential resistance region	71
63. Various avalanche oscillations calculated for simulated 1N4148 diode	72
64. MULTIPATT current oscillations calculated for 300 K, $V = 232 \text{ V}$, $R_g = 50 \Omega$, and $C = 1 \times 10^{-12} \text{ F}$	73
65. Distribution of electrons across diode during current growth stage	74
66. Variation of IMPATT frequency with current density at indicated temperatures	75
67. Typical relaxation oscillations	76
68. Plots of oscillation period and frequency	78

FIGURES (Cont'd)

	<u>Page</u>
69. Plots of $\ln(1 + x)$ and of $0.8\sqrt{x}$ as function of x	80
70. Calculated values of negative resistance, inductance (L), and LI as function of V_a	80
71. Calculated time constant (L/ R) and growth constant (λ) as function of V_a	80
72. Typical pulsed avalanche oscillation observed in 1N645	81
73. Frequency of oscillations in 1N645 as function of C	82
74. Calculated static characteristics for simulation of 1N645	83
75. Calculated oscillations for 1N645 simulation	83
76. Voltage and current oscillations calculated for 1N645	83
77. Change of frequency with temperature	84
78. Diode temperature in time and space for run of figure 77	85
79. Variation of frequency with current density for several diodes	86
80. Observed change of frequency of relaxation oscillation with temperature in 1N645	86
81. Field distributions for step junctions with zero current flow	88
82. Junction field for step junctions with zero current flow as function of doping level	89
83. Field distribution for linearly graded junction with zero current flow	89
84. Distribution of carriers during turn-on transient	91
85. Distribution of field during turn-on transient	91
86. Voltage and current turn-on transients	92
87. Forward characteristics for several diode widths	93
88. Forward characteristics for 12- μ m PIN diode for recombination lifetimes of 1, 10, and 100 μ s	93

FIGURES (Cont'd)

	<u>Page</u>
89. Field and carrier distributions for $\tau = 1 \mu\text{s}$	94
90. Field and carrier distributions for $\tau = 10 \mu\text{s}$	94
91. Field and carrier distributions for $\tau = 100 \mu\text{s}$	95
92. Maximum field as function of current density for three recombination lifetimes	96
93. Comparison of field and carrier distributions calculated with and without avalanche multiplication	96
94. Carrier density at position where electron and hole densities are equal	97
95. Maximum field as function of equal carrier density at that position	97
96. Maximum field as function of equal carrier density for 3- and 4- μm diodes	97
97. Forward characteristics for 12- μm diode at different temperatures	97
98. Current decay during reverse switching of 12- μm PIN diode	99
99. Charge distributions during reverse recovery of diode of figure 98 with 15 V applied	99
100. Field distributions during reverse recovery, corresponding to data of figure 99	100
101. Current densities during reverse switching into avalanche for 12- μm PIN diode	100
102. Dynamic current density versus voltage curves for 12- μm PIN diode	101
103. Calculated phase angle as function of current density, determined from superimposed ac signal of frequency in GHz	102
104. Impedance as function of current calculated at frequency labeled	102
105. Inductance as function of current density determined from figures 103 and 104, assuming resonance with device capacitance	102

FIGURES (Cont'd)

	<u>Page</u>
106. Static characteristics of 12- μm N-type diodes	103
107. Characteristics of 12- μm N-type diode doped to $3 \times 10^{15} \text{ cm}^{-3}$ at 400 K	106
108. Field distributions for current density/voltage points as numbered in figure 107	106
109. Distribution of electron and hole densities for numbered points of figure 107	106
TABLE 1.--Breakdown Data for 4- μm Diodes Doped to $5 \times 10^{15} \text{ cm}^{-3}$, Diodes Area = $1 \times 10^{-4} \text{ cm}^2$	35

1. INTRODUCTION

The phenomenon of second breakdown was first reported in diodes by Tauc and Abraham¹ and in transistors by Thornton and Simmons.² The name second breakdown has been chosen because the first appearance of micro-amperes of current in a reverse-biased diode was called breakdown. Experimentally, second breakdown is generally identified by an abrupt decrease of voltage and/or a sudden increase of current after a time of relatively constant current and voltage. If not prevented by current limiting in the external circuit, second breakdown usually leads to device damage. Second breakdown is of particular interest to individuals in the power semiconductor community, in the electromagnetic pulse (EMP) community,³ and, increasingly, to those in the integrated-circuit community.

Since the first reports, there has been a controversy over whether electronic or thermal processes are predominant in the initiation of second breakdown. A comprehensive review and bibliography of early papers has been given by Schafft.⁴ Two more recent reviewers are Kalab⁵ and Dickhaut.⁶ A few other recent contributions will be cited later in this report.

In 1976, Ward⁷ described an electrothermal model of second breakdown. The computer program used in this model was originally written for study of electrical breakdown in gases,⁸ modified for study of

¹J. Tauc and A. Abraham, *Thermal Breakdown in Silicon P-N Junctions*, *Phys. Rev.*, 108 (1957), 936-937.

²C. G. Thornton and C. D. Simmons, *A New High Current Mode of Transistor Operation*, *IRE Trans. Electron Devices*, ED-5 (January 1958), 6-10.

³L. W. Ricketts, J. E. Bridges, and J. Miletta, *EMP Radiation and Protective Techniques*, John Wiley and Sons, New York (1976).

⁴H. A. Schafft, *Second Breakdown--A Comprehensive Review*, *Proc. IEEE*, 55 (August 1967), 1272-1278.

⁵B. Kalab, *Analysis of Failure of Electronic Circuits for EMP Induced Signals--Review and Contribution*, Harry Diamond Laboratories, HDL-TR-1615 (August 1973).

⁶R. H. Dickhaut, *Electromagnetic Pulse Damage to Bipolar Devices, Circuits and Systems (Magazine)*, 10 (April 1976), 8-21.

⁷A. L. Ward, *An Electro-Thermal Model of Second Breakdown*, *IEEE Trans. Nucl. Sci.*, NS-23 (December 1976), 1679-1684.

⁸W. Börsch-Supan and H. Oser, *Numerical Computation of the Temporal Development of Currents in a Gas Discharge Tube*, *J. Res., National Bureau of Standards*, 67B (January 1963), 41-60.

electrical processes in semiconductors,⁹ and finally modified to include study of thermal effects⁷ important in second breakdown. Other papers¹⁰⁻¹² on second breakdown have followed. It is the purpose of this report to unify these publications with additional material into a single comprehensive study of the basic physical processes in the initiation of second breakdown in silicon diodes.

2. FORMULATION OF COMPUTER PROGRAM

2.1 Basic Equations

The one-dimensional continuity equations for electrons and holes, respectively, in a semiconductor are

$$e \partial n / \partial t = -\partial J_- / \partial x + \alpha J_- + \beta J_+ - R, \quad (1)$$

$$e \partial p / \partial t = \partial J_+ / \partial x + \alpha J_- + \beta J_+ - R, \quad (2)$$

where x and t are the space and time coordinates, e is the electron charge, n and p are the electron and hole number densities, α and β are the ionization coefficients for electrons and holes, and R is the recombination rate. The electron and hole current densities, J_- and J_+ , are given by

$$J_- = ne\mu_-E - eD_-(dn/dx), \quad (3)$$

$$J_+ = pe\mu_+E + eD_+(dp/dx), \quad (4)$$

where μ_- and μ_+ are the electron and hole mobilities, D_- and D_+ are the diffusion coefficients, and E is the electric field.

Space-charge effects are determined by the one-dimensional Poisson equation

⁷A. L. Ward, *An Electro-Thermal Model of Second Breakdown*, *IEEE Trans. Nucl. Sci.*, NS-23 (December 1976), 1679-1684.

⁹J. L. Scales and A. L. Ward, *Effects of Space Charge on Mobility, Diffusion, and Recombination of Minority Carriers*, *J. Appl. Phys.*, 39 (February 1968), 1692-1700.

¹⁰A. L. Ward, *Studies of Second Breakdown in Silicon Diodes*, *IEEE Trans. Parts and Hybrids Packag.*, PHP-13 (December 1977), 361-368.

¹¹A. L. Ward, *Calculations of Second Breakdown*, *IEEE Trans. Nucl. Sci.*, NS-24 (December 1977), 2357-2360.

¹²A. L. Ward, *Doping Profiles and Second Breakdown*, *Proceedings, 1979 Electrical Overstress/Electrostatic Discharge Conference, Denver, CO (1979)*, 25-77. Reliability Analysis Center, Rome Air Development Center, EOS-1, 109-115.

$$dE/dx = e(n - p + N)\kappa\epsilon_0, \quad (5)$$

where κ is the dielectric constant for the semiconductor, ϵ_0 is the permittivity of free space, and $N(x)$ is the distribution of net fixed charge. The sign convention in equations (1) through (5) is chosen so that E , J_- , and J_+ are all normally positive quantities.

The one-dimensional thermal diffusivity equation is

$$\rho c \frac{\partial T}{\partial t} = JE + k_T \frac{\partial^2 T}{\partial x^2} + \frac{\partial k_T}{\partial T} \left(\frac{\partial T}{\partial x} \right)^2, \quad (6)$$

where T is the temperature, J the total current density, ρ the semiconductor density, c the heat capacity, and k_T the thermal conductivity.

It may be shown from equations (1) through (5) that the total current density,

$$J = J_- + J_+ + \kappa\epsilon_0 (dE/dt), \quad (7)$$

is a constant in space. This merely expresses current continuity in one dimension. The accuracy of the calculations may be monitored by the constancy of J across the diode.

2.2 Supplementary Equations

The cathode ($x = 0$) to anode ($x = d$) distance is divided into M equal intervals of width Δx . Initial ($t = 0$) arrays of $M + 1$ values must be given for n , p , and T , and a similar array given for the fixed charges, $N = N_D - N_A$, where N_D is the net number density of donors and N_A is the net number density of acceptors.

Two boundary conditions are required for equations (1) and (2): the electron current density at $x = 0$ and the hole current density at $x = d$. Alternately, the number densities can be given and the current densities calculated from equations (3) and (4). At present, the boundary currents are constant in time.

The boundary condition for equation (5) is supplied by the total voltage across the diode. The initial voltage across the diode must be given, and that for later times is determined by the external circuit. Optional external circuits are available, but for this report, the diode, shunted by a capacitance, C , is in series with a load resistance, R_s , and a voltage source, $V(t)$. The voltage source may be constant in time, have one discrete step, or have an incremental sinusoidal variation. The last option allows a constant dV/dt value to be closely approximated.

Equations (1) through (5) have been solved by difference equations whose stability has been discussed by Börsch-Supan and Oser.⁸ Stability conditions require that the time step Δt be less than the dielectric relaxation time, $\tau = \kappa\epsilon_0/\sigma$, where σ , the conductivity, is given by

$$\sigma = e(p\mu_p + n\mu_n) = J/E .$$

To an excellent approximation,⁹ any uncompensated charge in a semiconductor will die out exponentially with the time constant τ . A second stability condition requires that the time step be less than twice the $R_C C$ time constant of the external circuit. Also, accuracy of calculations (and usually stability) require that Δt be chosen less than the transit time of the fastest particle across Δx . A constant $F \leq 1$ is chosen and we set

$$\Delta t = F(\Delta x)/v_{\max} , \quad (8)$$

where v_{\max} is the maximum value of v_- or v_+ at any space point. A final stability condition is that the change in E in the distance Δx must be less than E itself. This condition is usually violated when $E(x)$ changes sign. If the negative field is of short duration, or if the boundary between negative and positive field is moving, the calculations quickly recover. However, if negative fields persist, the calculations are halted.

It has been shown¹³ that the difference equation representations of equations (1) and (2), with only the conduction current density terms included (that is, neglecting the diffusion components of eq (3) and (4)) introduces a diffusion factor that is a realistic analogy to particle diffusion. The magnitude of the diffusion is given by

$$D/\mu = (1 - F)V/2M , \quad (9)$$

where V is the diode voltage, F is defined in equation (8), and $M = d/\Delta x$ is defined at the beginning of this section. The derivation assumes that the field is a constant. Most calculations have been made with $M = 50$ or 100 . For these values, D/μ is usually found to be greater than

⁸W. Börsch-Supan and H. Oser, Numerical Computation of the Temporal Development of Currents in a Gas Discharge Tube, *J. Res., National Bureau of Standards*, 67B (January 1963), 41-60.

⁹J. L. Scales and A. L. Ward, Effects of Space Charge on Mobility, Diffusion, and Recombination of Minority Carriers, *J. Appl. Phys.*, 39 (February 1968), 1692-1700.

¹³A. L. Ward, Effect of Space Charge Upon the Transport of Charge Carriers, *J. Appl. Phys.*, 35 (March 1964), 469-474.

e/kT , the value required by the Einstein relation, where k is the Boltzmann constant. Choosing larger values of M greatly increases the cost of calculations. Since diffusion is simulated by the difference equations, the diffusion terms of equations (3) and (4) are omitted. The parameter F is chosen to be close to unity if the time step satisfies stability conditions. For most calculations, $0.1 < F < 0.9$.

Stability conditions require that Δt be less than the dielectric relaxation time, τ . For semiconductor material of interest, τ is of the order of picoseconds. However, the thermal time constant for most diodes is microseconds, depending largely upon the distance to the heat sink. This disparity of electrical and thermal time constants has made it impractical to include the two heat conduction terms in equation (6) in the computer program. Therefore, only the heat source term, JE , on the right side of equation (6) has been programmed. The impact of this approximation is negligible for the time scale imposed by computation cost.

To solve equations (1) through (6), the cycle is as follows. The initial values of $n(x)$, $p(x)$, and $N(x)$ are used to calculate dE/dx from equation (5). Setting $E(0) = 0$, $\int E dx$ is evaluated. Then the field at each grid point is adjusted by a constant increment in order that $\int E dx = V$, the desired voltage across the diode. Knowing $E(x)$, all field-dependent quantities, such as $J_-(x)$, $J_+(x)$, $\alpha(x)$, $\beta(x)$, $\mu_-(x)$, and $\mu_+(x)$, may be calculated. These quantities are then used to calculate new values of $n(x)$, $p(x)$, and $T(x)$ at the time Δt , with equations (1), (2), and (6), respectively. The average current density is calculated from equation (7) and, with the given diode area, the total current flowing in the diode is determined. This current then is used to obtain an adjusted voltage across the diode due to the action of the external circuit, as for example the IR_s drop across the external resistor, R_s . This completes one time cycle.

The form of the recombination rate in equations (1) and (2) in the computer program was chosen to be

$$R = eR'(np - n_i^2)/n_i \quad (10)$$

where n_i is the carrier density of intrinsic material and R' is the volume rate of electron hole recombination. This form for the recombination rate was chosen for its versatility. The usual expressions using minority carrier lifetimes, τ_n and τ_p , are much more complex in that they are functions of the doping density. Equation (10) reduces to the usual minority carrier lifetime equation when the excess minority carrier number density is small compared to the doping density. The result⁹ is that

⁹J. L. Scales and A. L. Ward, *Effects of Space Charge on Mobility, Diffusion, and Recombination of Minority Carriers*, *J. Appl. Phys.*, 39 (February 1968), 1692-1700.

$$\tau_n = n_i/R'p_o, \quad \tau_p = n_i/R'n_o, \quad (11)$$

where n_o and p_o are the majority carrier densities. Thus, the minority carrier lifetime is a function of n , p , n_o , and p_o as desired. R' needs only to be adjusted for the quality of the material or to simulate gold doping, for example. Note from equation (10) that thermal generation of carriers exceeds the recombination when the np product is less than n_i^2 .

3. MATERIAL PARAMETERS FOR SILICON

The most critical material parameters for semiconductor breakdown studies are the ionization coefficients. The ionization coefficients, defined as the number of electron-hole pairs created by collisions per centimeter of travel, are given by

$$\alpha = A_1 \exp(-A_2/E), \quad (12)$$

$$\beta = B_1 \exp(-B_2/E), \quad (13)$$

where A_1 and B_1 are empirical constants. Most of the calculations reported herein use those measured by Van Overstraeten and DeMan.¹⁴ The computer program allows different empirical constants to be used above a fixed value of E . The constants used were generally chosen as follows:

$A_1 = 7.03 \times 10^5$	for all E ,
$A_2 = 1.23 \times 10^6$	for all E ,
$B_1 = 1.582 \times 10^6$	$E \leq 4 \times 10^5$ V/cm,
$B_1 = 6.75 \times 10^5$	$E > 4 \times 10^5$ V/cm,
$B_2 = 2.036 \times 10^6$	$E \leq 4 \times 10^5$ V/cm,
$B_2 = 1.693 \times 10^6$	$E > 4 \times 10^5$ V/cm.

The temperature variation of the ionization coefficients was based on the measurement of Crowell and Sze.¹⁵ They found variation for both

¹⁴R. Van Overstraeten and H. DeMan, Measurement of the Ionization Rates in Diffused Silicon p-n Junctions, *Solid-State Electron.*, 13 (1970), 583-608.

¹⁵C. R. Crowell and S. M. Sze, Temperature Dependence of Avalanche Multiplication in Semiconductors, *Appl. Phys. Lett.*, 9 (September 1966), 242-244.

A_1 and A_2 with temperature, but the variation of A_2 was small and irregular, while that of A_1 was larger and more regular. Therefore, only the variation of A_1 was used. A_1 is reduced by 0.2 percent for each degree increase above 300 K. No measurements are available for the temperature dependence of the hole ionization coefficients, so an equal decrease was assumed.

A second material parameter of importance is the variation of carrier mobility with field, temperature, and doping level. The variation of the carrier mobilities with field is given by equations of the form

$$\mu = \mu_0(1 - C_1E) , \quad E \leq C_4 , \quad (14)$$

$$\mu = C_2E^{-1/2}(1 - C_3E^{-3/2}) , \quad E > C_4 , \quad (15)$$

where μ_0 is the low field mobility and the constants C_i may be considered empirical. Each maximum velocity is also bounded by maximum values, which are included in the input data. The low field mobilities were taken from Sze¹⁶ and are $\mu_0 = 1500$ cm/V-s for electrons and $\mu_0 = 600$ cm/V-s for holes. There is a further option in the computer program to interpose a transition range between two given field values where equations (14) and (15) are used. The expression is a power series in E and the parameters are calculated internally to insure continuity of v and dv/dE at the end points. Several expressions have been used in the calculations, but the expressions used most often give the velocity versus field curves given in figure 1. The low field mobility decreases with increasing temperature. The temperature variation given by Sze¹⁶ is that the electron mobility varies as $T^{-2.5}$ and the hole mobility as $T^{-2.7}$. The variation of the saturated drift velocities with temperature is less than for the low field mobility. The variation chosen was based on the measurements of Duh and Moll¹⁷ and of Canali et al.¹⁸ The variation of drift velocity with field at elevated temperatures is also shown in figure 1.

¹⁶S. M. Sze, *Physics of Semiconductor Devices*, Wiley-Interscience, New York (1969), 39-41, 57-59, 121-126.

¹⁷C. Y. Duh and J. L. Moll, *Electron Drift Velocity in Avalanche Silicon Diodes*, *IEEE Trans. Electron Devices*, ED-14 (January 1967), 46-49.

¹⁸C. Canali, G. Majni, R. Minder, and G. Ottaviani, *Electron and Hole Drift Velocity Measurements and Their Empirical Relation to Electric Field and Temperature*, *IEEE Trans. Electron Devices*, ED-22 (November 1975), 1045-1047.

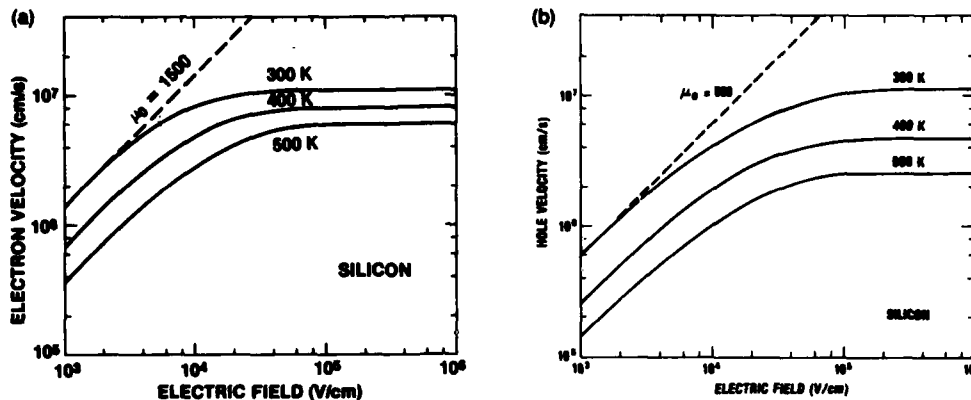


Figure 1. Temperature variation of (a) electron and (b) hole velocities as function of electric field.

There is also an option in the computer program to vary the drift mobilities as a function of doping level. The variation follows that given in Sze.¹⁶ However, measurements of saturation velocities as a function of doping level and of temperature have not been made. Just as the variation of the saturation velocities with temperature is less than that of the low field mobilities, one should expect that the variation with doping level should be less for the saturated velocities. For this reason, the option to vary the mobilities with doping level has not been used for second breakdown studies where saturation velocities are predominant.

The variation of the intrinsic density with temperature was chosen as

$$n_1^2(T) = 2 \times 10^{20} (T/300)^3 \exp[(E_g/k)(300^{-1} - T^{-1})] \quad , \quad (16)$$

where E_g is the band gap energy of silicon. The variation of the injected (thermally generated) current density with temperature was assumed to be the same as for $n_1^2(T)$, since $np = n_1^2$ and the majority carrier density is fixed by the doping level. Since the effective thermally injected current is determined by both thermal generation and particle diffusion, the calculated saturated current density for the ideal diode equation is in poor agreement with measurements. For this reason a value of room temperature thermal injection current, J_0 , of 1×10^{-7} A/cm² was chosen for each boundary. The minority electron current density injected at the cathode boundary is designated J_{no} and the minority hole current density injected at the anode boundary is

¹⁶S. M. Sze, *Physics of Semiconductor Devices*, Wiley-Interscience, New York (1969), 39-41, 57-59, 121-126.

designated J_{po} . As stated, $J_{no} = J_{po} = J_o = 1 \times 10^{-7}$ A/cm was chosen at room temperature and was varied with temperature as $n_i^2(T)$, as given in equation (16), for higher temperature runs.

The other silicon material properties are taken from Sze.¹⁶ They are

dielectric constant	11.8
density	2.328 g/cm ³
energy gap at 300 K	1.12 eV
minority carrier lifetime	2.5×10^{-3} s
specific heat	0.7 J/gC
thermal conductivity at 300 K	1.45 W/cmC

4. PROCEDURES AND DISCUSSION

Before we present the results of the computer calculations it is useful to further discuss the formulation, the procedures, and the limitations of the computer program.

First, consider the continuity equations, (1) and (2). If $\partial n/\partial t = \partial p/\partial t = 0$, then a steady-state condition prevails. The steady-state equation for electrons, neglecting recombination, is

$$\partial J_-/\partial x = \alpha J_- + \beta J_+ \quad (17)$$

Since, for silicon, the ionization constant for electrons is of an order of magnitude greater than for holes, we may, as an approximation, neglect β compared to α . Then, for a constant field, one obtains

$$J_-(x) = J_o \exp(\alpha x) \quad .$$

This shows that for a PIN diode, where the field is constant, we should expect the electron current density to increase exponentially across the diode at low currents, where space charge can be neglected. This approximation will be shown to be surprisingly good for the high field region of other diodes, also. Since $dE/dt = 0$ in the steady state, $J_+(x) = J - J_-(x)$, from equation (7).

¹⁶S. N. Sze, *Physics of Semiconductor Devices*, Wiley-Interscience, New York (1969), 39-41, 57-59, 121-126.

The steady-state solution of the continuity equations determines the static current density versus voltage characteristic for the device. The static characteristic separates the high-voltage region, where currents increase with time, from the low-voltage region, where currents decrease with time. In dynamic calculations with a constant applied voltage and neglecting heat generation, a point of the static characteristic is attained after a period of time.

Since steady-state calculations are much simpler and cheaper than dynamic calculations, it may be suggested that they should be used in conjunction with dynamic calculations. This was done by the author in studies of breakdown in gases. However, the difference in accuracy between the two programs made the static program of little use in supporting the dynamic program. Therefore, the static program was not modified to supplement the dynamic program for semiconductor calculations.

A second useful approximation to the continuity equations considers the case where $\partial J/\partial x$ is small and may be neglected. We then have the approximation that

$$e \partial n / \partial t = \alpha J_- = \alpha e v_- . \quad (18)$$

Again we consider the constant field case so that α and v are constant. The solution to this equation is that

$$J_-(t) = J_-(0) \exp(\alpha v t) .$$

This shows that the current in a diode will initially grow exponentially with a time constant of $(\alpha v)^{-1}$. This technique has been used with much greater accuracy by Holway.¹⁹

It is also useful to consider some approximate solutions to the thermal diffusivity equation, equation (6). For times short compared to the thermal time constant (τ_{th} , defined later), the terms of equation (6), including the spatial derivatives of T with x , are small, and

$$\frac{dT}{dt} \approx \frac{JE}{\rho c} . \quad (19)$$

This expression defines an adiabatic calculation.

¹⁹L. H. Holway, Jr., *Electron-Hole Avalanches with Constant Ionization Coefficients*, *IEEE Trans. Electron Devices*, ED-26 (June 1979), 991-993.

For the one-dimensional approximation, where the heat source is planar and all heat flows to a heat sink at a distance, L , which is at a temperature T_0 , the junction temperature, T_j , as a function of t is

$$T_j = T_0 + \theta P [1 - \exp(-t/\tau_{th})] , \quad (20)$$

where θ is the thermal resistance and P is the power dissipated. Thermal resistance is defined from the junction temperature in the steady state,

$$T_j = T_0 + \theta P . \quad (21)$$

The thermal time constant is found to be

$$\tau_{th} = \rho c L^2 / k_T , \quad (22)$$

and

$$\theta = L / k_T A , \quad (23)$$

where A is the diode area. Combining equations (22) and (23),

$$\theta / \tau_{th} = (\rho c A L)^{-1} . \quad (24)$$

The rate of temperature rise is found from equation (20) to be

$$dT_j / dt = (P\theta / \tau_{th}) \exp(-t/\tau_{th}) . \quad (25)$$

Since $P = IV$, we find, with the use of equation (24),

$$\begin{aligned} dT_j / dt &= (IV / AL\rho c) \exp(-t/\tau_{th}) \\ &= (JE / \rho c) \exp(-t/\tau_{th}) . \end{aligned} \quad (26)$$

Comparing equation (26) with (19), we see that the heat conduction processes reduce the rate of temperature rise by the exponential time function of τ_{th} .

One further useful thermal coefficient is the thermal diffusivity, $D_{th} = k_T / \rho c$, analogous to the electrical diffusion coefficient. The distance that heat diffuses in a given time, t , depends on the geometry, but in general is given by $\sqrt{D_{th} t}$.

It was mentioned in section 2 that stability conditions require that Δt be less than the dielectric relaxation time, $\tau = \kappa \epsilon_0 / \sigma$. Since τ is inversely proportional to the number densities, computations increase in cost for higher doping levels. For this reason, only the high field

regions are simulated. Generally, the maximum doping at the boundaries is set at about $1 \times 10^{17} \text{ cm}^{-3}$ or greater. This allows the field at the boundaries to be well below that for which the velocity starts to saturate, which in turn is more than an order of magnitude below the avalanche field. Calculations made with higher doping levels at the boundaries show little difference if the above criteria are observed. With the use of a practical number of distance steps ($M = 50$ to 100), it is often found that negative fields are calculated near the boundaries of high doping levels. In this case, the negative fields are eliminated by reducing the doping levels at the boundaries. Then, at higher currents, with their resulting space-charge field distortion, the doping levels may again be increased to observe the above criteria.

The cost of running the program on an IBM 370/168 computer varies with doping density, diode widths, and other factors. A typical cost is \$10 per nanosecond of problem time. This precludes problem times over a few tens of nanoseconds. However, it will be shown that longer problems may often be treated in reasonable approximation.

One important factor in junction diode physics is the punch-through factor, PTF. A diode is termed punched through if the field extends from the junction completely through the low doping region into the high doping region. Some investigators term this effect in diodes reach-through and use the term punch-through for transistors. However, the term punch-through is used unanimously for IMPATT diodes, and is so used in this report. The PTF is considered equal to the ratio of (1) the distance from the junction to where the field extrapolates to zero at breakdown to (2) the maximum depletable width, W , i.e., the width of the low doping region. Therefore, $\text{PTF} = 1$ for a diode whose high field region just reaches the high doping boundary region at breakdown. For the same width diode, the $\text{PTF} > 1$ for a diode doped more lightly and the $\text{PTF} < 1$ for a more heavily doped diode. The definition of PTF's is illustrated in figure 2. Punch-through factors may be extended to two-sided diodes and linearly graded diodes, using the appropriate nonlinear extrapolation in the latter.

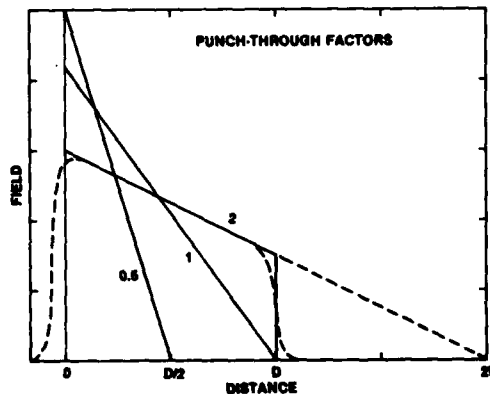


Figure 2. Punch-through factor defined. Curved dashed lines show field distribution of non-ideal device.

Most junction diodes are one-sided; that is, one side has a much lower doping level than the other. One-sided diodes either may be abrupt, with steps in the doping profile, or diffused, where the doping changes gradually. Diffusion profiles may be given²⁰ either by the complementary error function or by the Gaussian distribution according to the experimental procedure used. Either distribution gives approximately an exponential falloff at a distance from the surface. Most calculations have been made for exponential decreases in doping from each boundary added to a constant N- or P-type doping. The diodes are designated N type for a P^+NN^+ doping profile and P type for an N^+PP^+ doping profile. Two-sided diodes, either abrupt or linearly graded, will also have high doping regions, decreasing exponentially from the boundaries.

Many thermal models of second breakdown use the variation of resistivity with temperature. This variation is shown in figure 3. However, resistivity no longer is meaningful when the mobility becomes a function of field. As shown in figure 1, this occurs for fields above about 1×10^3 V/cm. In silicon, the velocity of electrons becomes saturated at fields only about one-tenth of the avalanching field. Therefore, the use of resistivity variation with temperature to study second breakdown is inaccurate. Further, many authors term the decrease of resistivity with temperature as a negative resistivity. This is a misnomer. Current contraction follows directly from a true negative resistance, but not from a negative temperature coefficient. This will be discussed further in later sections.

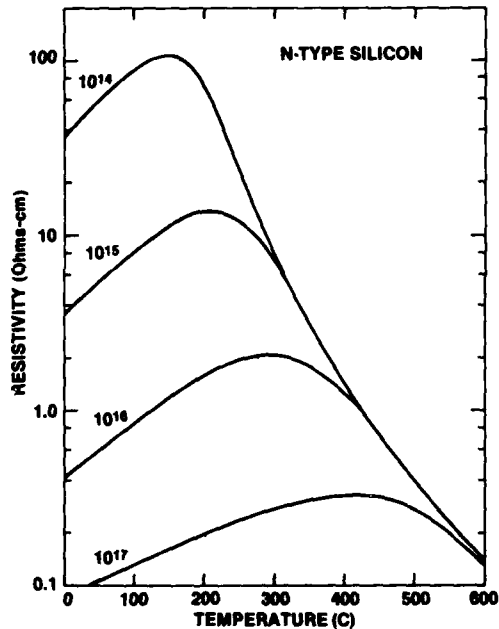


Figure 3. Typical variation of resistivity with temperature. Parameter is doping level in cm^{-3} .

5. TYPICAL REVERSE-BIAS STATIC CHARACTERISTICS

Quasi-static current density versus voltage characteristics have been calculated point by point for typical N- and P-type diodes. The prefix quasi has been used to indicate some slight current decrease as the temperature rises. Initial conditions for the calculations are

²⁰A. S. Grove, *Physics and Technology of Semiconductor Devices*, John Wiley and Sons, New York (1967), 44-52, 194-201.

either space-charge free, i.e., the mobile charges equal the fixed charge at all points, or the equilibrium condition of a previous calculation. Generally, quasi-equilibrium is obtained in a few tenths of a nanosecond of problem time.

5.1 Current Regimes

The results are presented more clearly by dividing the current density (J) range into four regimes as defined below. These regimes will be exemplified for an N-type diode at room temperature (300 K). The total diode width is 4 μm . Each of the P^+ and N^+ regions is 0.5 μm , and the 3- μm N-region is doped to $5 \times 10^{15} \text{ cm}^{-3}$. The boundary between the N and N^+ region is arbitrarily set at where the dopin. level, N , is doubled. The device is punched through at breakdown. A doping level of 7×10^{15} is required for $\text{PTF} = 1$.

The regime below $J = 1 \times 10^3 \text{ A/cm}^2$ for this diode is designated the space-charge-free (SCF) or the single-avalanche regime. Since $J_0 = 1 \times 10^{-7} \text{ A/cm}$ for this calculation, the current multiplication factor for this region reaches a maximum of 1×10^{10} . In the SCF regime, the current increases exponentially with voltage as shown in figure 4. The data are fitted to the equation

$$J_{\text{SCF}} = J_{10} \exp[(V - V_{B1})/V_{10}] \quad , \quad (27)$$

where $J_{10} = 0.4 \text{ A/cm}^2$, $V_{B1} = 79 \text{ V}$, and $V_{10} = 0.41 \text{ V}$.

The second regime is the space-charge-limited (SCL) regime and extends from 1×10^3 to $8 \times 10^3 \text{ A/cm}^2$. For a punched-through diode, the best fit to this regime has been found to be that J varies as the square of the voltage above V_{B1} . This is shown for this diode in figure 5 for three values of V_{B1} . The PTF of this diode is about 1.4 and the best fit is between slopes $M = 2$ and $M = 1.6$. For higher PTF's, the best fit is usually $M = 2$. The dashed curve labeled J_1 in figure 4 is

$$J_1 = 50(V - 79)^2 \text{ A/cm}^2 \quad .$$

The current density falls below the exponential increase with voltage because of the space charge of the mobile electrons. The space charge decreases the magnitude of dE/dx , increasing the field away from the junction. When the field near the NN^+ junction reaches the avalanche field, the current rises above the SCL value. This third J regime is designated the double-avalanche regime and extends from $J = 8 \times 10^3$ to $2.3 \times 10^4 \text{ A/cm}^2$. In the double-avalanche regime the current exceeds the SCL current by another exponential increase with voltage. This extra current is labeled J_2 in figure 4 and is given by

$$J_2 = 4.6 \times 10^{-1} \exp[(V - 79)/1.69] \quad .$$

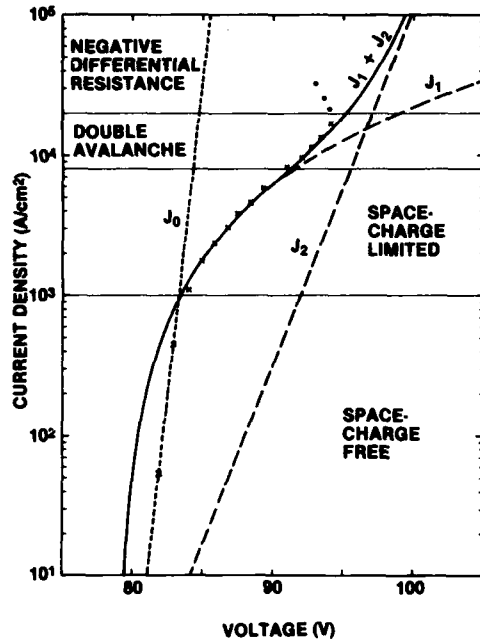


Figure 4. Static current density versus voltage characteristic for 4- μm N-type diode doped to $5 \times 10^{15} \text{ cm}^{-3}$. Points are computed data and curves are analytic fits as described in text.

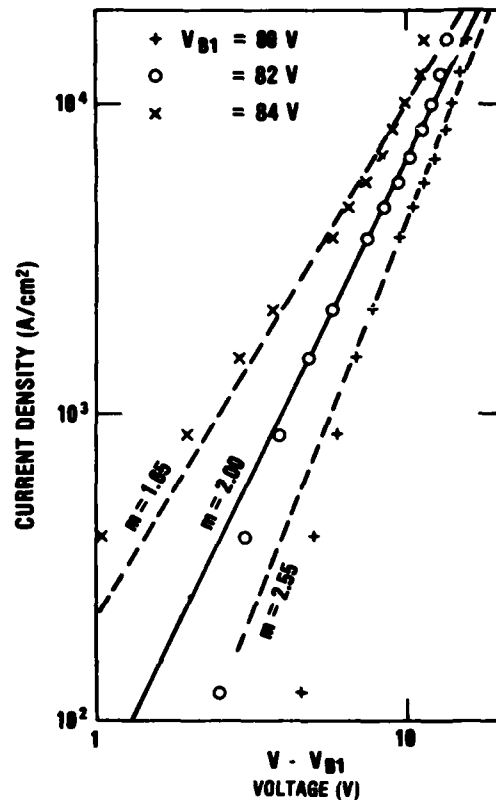


Figure 5. Current density as function of overvoltage for various assumed breakdown voltages, V_{B1} . Slope of each straight line is indicated.

The current in the SCL current regime can be rewritten as

$$J_{\text{SCL}} = (V - V_{B1})^2 / R_{\text{SC}} V_{B1} A, \quad (28)$$

where A is the diode area and R_{SC} is the space-charge resistance. V_{B1} is included in the denominator of equation (28) in order to retain the correct dimensions for R_{SC} . It will be shown later that, for diodes not punched through at breakdown, the current is proportional to the excess voltage above V_{B1} . Both cases may be included in a single expression:

$$J_{\text{SCL}} = (V - V_{B1})^{1+m} / R_{\text{SC}} V_{B1}^m A, \quad (29)$$

where $m = 0$ for $\text{PTF} \leq 1$ and $m = 1$ for $\text{PTF} > 1$. For $m = 0$, R_{SC} is often called the surge resistance, but space-charge resistance is more inform-

ative. For $m = 1$, the justification of calling R_{sc} the space-charge resistance follows from the near continuity of R_{sc} as the PTF changes from below to above unity.

The J-V characteristic reaches infinite slope (zero resistance) at $J = 2.3 \times 10^4$ A/cm and $V = 94.5$ V. The regime above this current density is the negative-differential-resistance (NDR) regime, and it is usually impossible to calculate steady-state conditions in this regime. The points shown in figure 4 for the NDR regime are average values for dynamic characteristics with increasing and with decreasing currents.

5.2 Diode Profiles

Figure 6 shows the electron- and hole-density distributions for currents in the SCL and double-avalanche regimes. Figure 7 shows the corresponding field distributions. Note that in the double-avalanche regime the mobile electron density exceeds the sum of the doping level and the hole density. This results in a change in the sign of dE/dx and a field minimum. The existence of double avalanching is shown more dramatically in figure 8, where αJ_- and βJ_+ are plotted across the diode. αJ_- is the rate of increase in charge density due to ionization by electrons, as may be seen from equation (1). Similarly, βJ_+ is the increase due to ionization by holes. Although α exceeds β by a factor of ~ 10 , βJ_+ usually exceeds αJ_- at some position, since generally J_+ exceeds J_- sufficiently in the p doping region. Plots of $J_-(x)$ and $J_+(x)$ are essentially proportional to $n(x)$ and $p(x)$, respectively, except in the N^+ and P^+ doping regions. The proportionality follows since the particle velocities are saturated in the N region. Figure 9 shows plots of αJ_- at the PN junction as a function of current density. Also shown is the value at the NN^+ junction, defined to be where $N(x)$ is twice the N region doping. αJ_- increases approximately linearly with J at the PN junction, since the junction field is almost constant as J increases. However, αJ_- increases with the 3.3 power of J at the NN^+ junction as a result of the increasing field. For $J > 1.5 \times 10^4$ A/cm, αJ_- is greater at the NN^+ junction than at the P^+N junction.

When $\alpha = \beta$, the criterion for breakdown is

$$\int_0^d \alpha dx = \alpha_{AVE}^d = 1 \quad (30)$$

This criterion is still often used as a breakdown criterion in silicon, although α ranges approximately 10 times greater than β in silicon. Plots of α_{AVE}^d and β_{AVE}^d as a function of J are shown in figure 10. It is seen that α_{AVE}^d is much greater than unity. A good approximation to breakdown is that the product of α_{AVE}^d and β_{AVE}^d is equal to one.

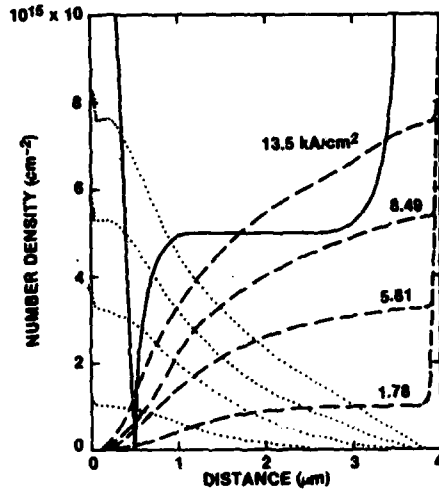


Figure 6. Distribution of number density for diode of figure 4. Doping profile is given by solid lines, electrons by dashed lines, and holes by dotted lines. Parameter is current density.

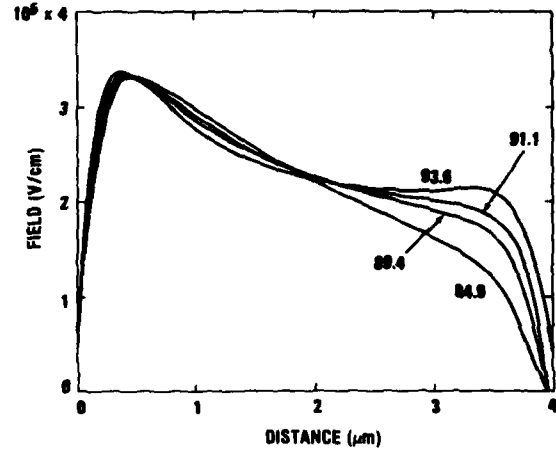


Figure 7. Field distributions corresponding to current densities in figure 6. Diode voltage is parameter.

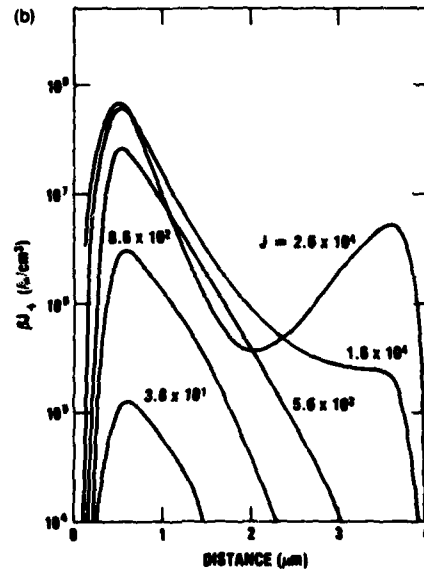
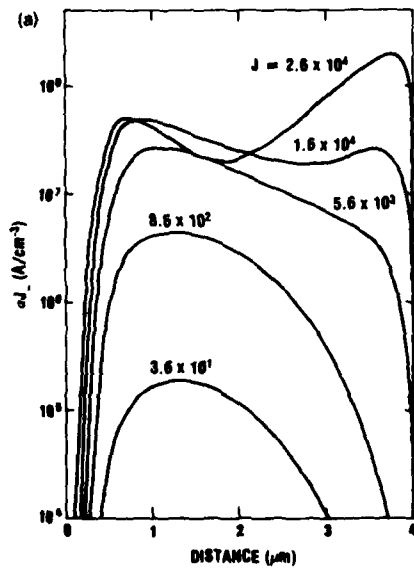


Figure 8. Distribution of ionization rates across N-type diode: (a) ionizations by electron collisions, and (b) ionizations by hole collisions. Parameter is current density in A/cm².

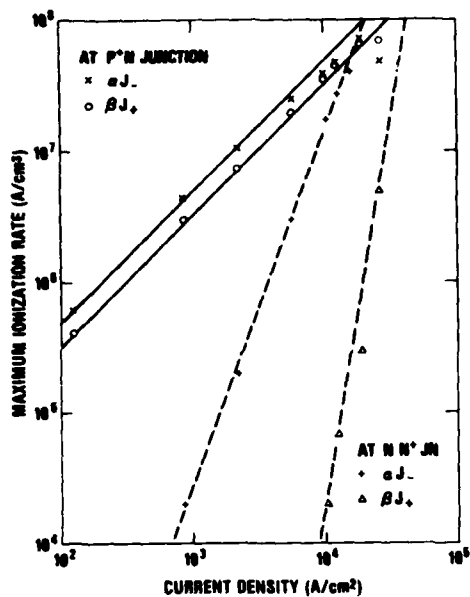


Figure 9. Maximum ionization rates as function of current density. Solid lines are drawn with a slope of 1.0. Rates for NN^+ junction (dashed curves) are not maxima, except at highest current densities.

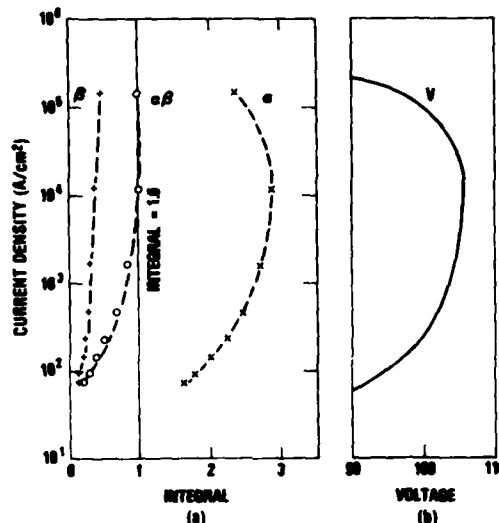


Figure 10. (a) Integrals of α , β , and $\alpha\beta$ across diode as function of current density for P-type diode. (b) Dynamic characteristic of diode, calculated with $dV/dt = 2 \times 10^{10}$ V/s.

Complementary N-type and P-type diodes have the same doping levels, diode width, and area. Calculations of quasi-static characteristics for the complementary P-type diode with a doping level of $5 \times 10^{15} \text{ cm}^{-3}$ and a $4\text{-}\mu\text{m}$ width yield a first-breakdown voltage V_{B1} of 80 V compared to 79 V for the N-type diode. The maximum voltage was 101.5 V at 1.6×10^4 A/cm compared to 94.5 V at 2.3×10^4 A/cm for the N-type diode. The maximum voltage will be designated the second breakdown voltage, V_{B2} . The difference in V_{B2} for the two diodes is 7 V compared to a difference of 1 V in V_{B1} . This indicates that the P-type diode has a greater space-charge resistance than does the N-type. From equation (28), with an assumed area of $1 \times 10^{-4} \text{ cm}^2$, the calculated value of R_{sc} for the N diode is 2.5Ω and for the P diode, 6.6Ω .

For the same $4\text{-}\mu\text{m}$ width diode, a doping level of $1 \times 10^{16} \text{ cm}^{-3}$ gives a PTF of about 0.7; that is, the field at breakdown extrapolates to zero at about 0.7 of the depletable width. For the P diode, $V_{B1} = 62$ V and $V_{B2} = 101$ V at 1.5×10^4 A/cm². Note that whereas V_{B1} is 17 V lower than that for the same width diode doped to $5 \times 10^{15} \text{ cm}^{-3}$, the values of V_{B2} are essentially the same. The static characteristic of this diode is shown in figure 11. This time, a linear scale is used to show that the current rises linearly with voltage above V_{B1} . A surge resistance can be defined in the conventional manner and is determined to be 23.8Ω for a diode of $1 \times 10^{-4} \text{ cm}^2$ area.

It has been shown that good analytical fits to the computer data can be made with $J \propto (V - V_{B1})$ for diodes with $PTF < 1$ and with $J \propto (V - V_{B1})^2$ for $PTF > 1$. How good are the fits for $PTF \approx 1$? For the 4- μm width diode, a doping of $7 \times 10^{15} \text{ cm}^{-3}$ gives $PTF \approx 1$. Figure 12 shows a dynamic J-V characteristic calculated for the P diode. The calculation was made with an applied voltage rising at the rate of $1 \times 10^{10} \text{ V/s}$. This technique greatly reduces the cost of calculation. It will be shown in a following section that this rate of rise gives a maximum error of about 1 V at any current density up to V_{B2} . Also shown in figure 12 is the fit of three analytic expressions. Dotted curve "0" is the exponential variation of current in the SCF region of $J < 5 \times 10^2 \text{ A/cm}$. The fit to equation (27) gives $J_{10} = 1.0 \text{ A/cm}$, $V_{B1} = 73.4$, and $V_{10} = 0.36 \text{ V}$. Solid curve "1" is the best fit to $J \propto V - V_{B1}'$, and the dashed curve "2" is the best fit to $J \propto (V - V_{B1}'')^2$. The analytic expressions are

$$J = 410(V - 77) \text{ and}$$

$$J = 10(V - 67)^2 .$$

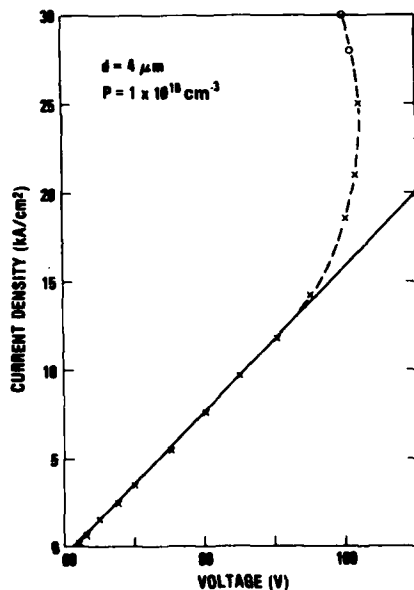


Figure 11. Static current density versus voltage characteristic for P-type diode. Diode width is 4 μm and doping level is $1 \times 10^{16} \text{ cm}^{-3}$.

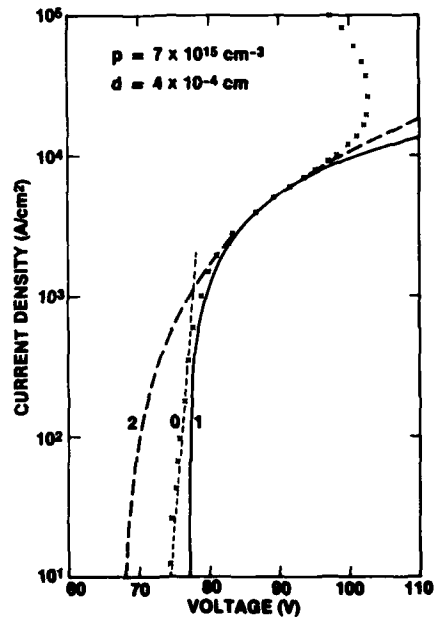


Figure 12. Characteristic for diode with $PTF = 1$. Individual points were calculated with $dV/dt = 1 \times 10^{10} \text{ V/s}$. Equations for analytic curves are given in text.

It may be noted that V_{B1} from equation (27) is intermediate between V_{B1}^i and V_{B1}^n . Again assuming $A = 1 \times 10^{-4} \text{ cm}^2$, R_{SC} calculated from equation (29) is found to be 24.4Ω for $m = 0$ and 14.9Ω for $m = 1$. Considering that $PTF = 1$ is a worst case for each expression, there is a reasonable fit by both expressions in the SCL region, which extends to about $8 \times 10^3 \text{ A/cm}^2$. An additional exponential term extends the fit into the double avalanche as shown previously. As expected, curve "1" is the better fit at lower J values, since the depleted region widens a little, and curve "2" is a better fit at higher J values, since no further widening of the depletion region is possible. For engineering analysis, it seems satisfactory to use $J \propto V - V_{B1}^i$ for $PTF \leq 1$ and $J \propto (V - V_{B1}^n)^2$ for $PTF > 1$. If a greater accuracy is desired, an intermediate value of m between 0 and 1 may be used for $PTF \approx 1$.

6. DYNAMIC CHARACTERISTICS

6.1 Constant dV/dt

A series of calculations has been made with varying constant rates of rise of the applied voltage, dV/dt . The initial charge distributions were chosen to give space-charge neutrality and the initial voltage somewhat below V_{B1} . Calculations were made for the complementary diodes discussed in section 5: $d = 4 \mu\text{m}$ and doping of $5 \times 10^{15} \text{ cm}^{-3}$. The dynamic characteristics are compared with the static characteristic in figure 13. The initial transients from the rather high initial currents are not shown, since they would tend to confuse the figure. The variation of voltage with time for four values of dV/dt is shown in figure 14. In order to allow the useful information to be displayed on a shorter time scale, zero time in this plot was chosen to be the first time that V_{B1} (80 V) was attained. Both figures 13 and 14

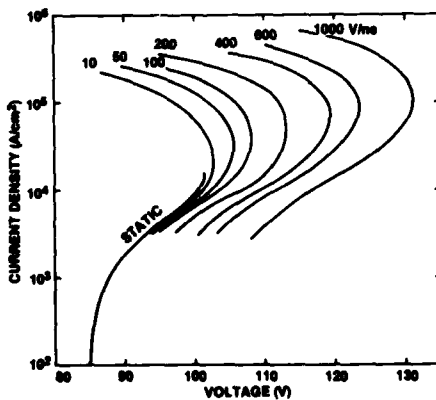


Figure 13. Dynamic characteristics calculated with labeled rates of voltage rise compared with calculated static characteristic. The $4\text{-}\mu\text{m}$ P-type diode is doped to $5 \times 10^{15} \text{ cm}^{-3}$.

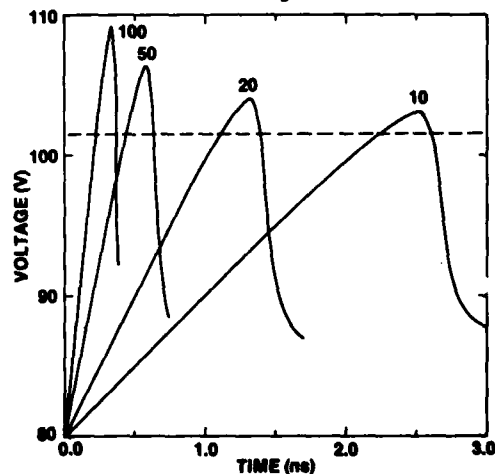


Figure 14. Variation of voltage with time for diode of figure 13. Time is measured from attainment of $V_{B1} = 80 \text{ V}$. Static value of V_{B1} is indicated by dashed curve. Parameter is dV/dt , V/ns .

show that the maximum voltage attained increases with the rate of voltage rise. The difference between this maximum voltage (V_{B2}) and that obtained in static calculations (V_{B20}) is plotted in figure 15 on a log-log scale against dV/dt . The slope of this curve is 2/3. Two of the points, those for $dV/dt = 2$ and 4×10^{11} V/s, are slightly above the straight line because the temperature of the diode was allowed to increase in time. All other points were calculated for a constant temperature of 300 K. The two points for the highest rates of dV/dt fall below the line because the initial voltage, required to prevent negative fields from developing for early times (small t), maintained an appreciable current minimum. It will be shown later that the presence of a residual current lowers the breakdown voltage. Also plotted in figure 15 as a function of dV/dt is the difference in current densities at V_{B2} and at V_{B20} ; i.e., $\Delta J_{B2} = J_{B2} - J_{B20}$. The straight line was obtained with a small adjustment in J_{B20} from that obtained from static calculations. The adjustment was less than the probable error in determining J_{B20} . The current difference points show more scatter than the voltage difference points. This should be expected from the greater difficulty in determining the J_{B2} values compared to the values of V_{B2} . The slope of the ΔJ curve is less than 2/3, and other similar calculations show a scatter in slopes. Data for the complementary N diode fell on the same line as for the P diode when V_{B20} was increased by 0.5 V from that determined by the static calculations. Again, this is less than the error range expected for determination of V_{B20} . Figure 16 shows the

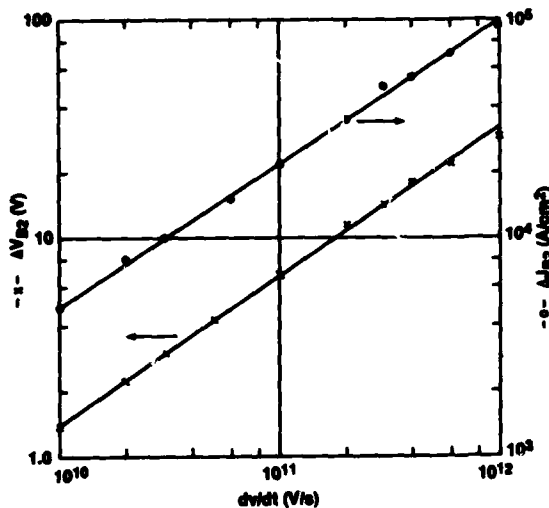


Figure 15. Log-log plots of excess voltage and current as function of dV/dt for diode of figure 13. Excess voltage is defined as maximum voltage attained with $dV/dt > 0$, less the static value with $dV/dt = 0$. Excess current is similarly defined.

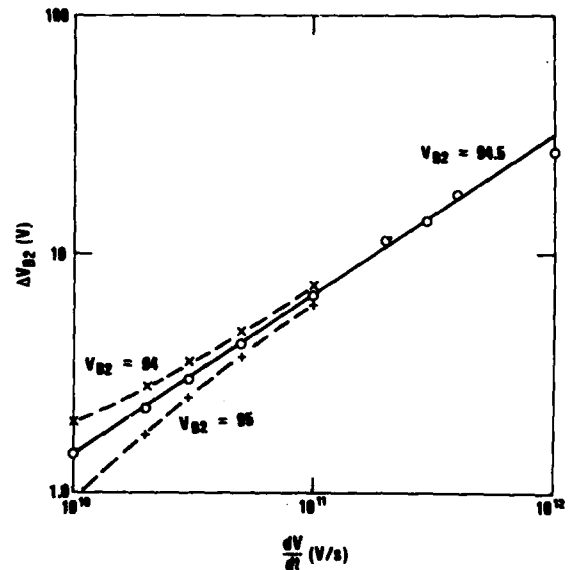


Figure 16. Excess voltage plotted as function of dV/dt for N-type diode. Assumed value for V_{B2} is labeled for each curve.

sensitivity of this type of plot to the choice of V_{B20} . It follows that one can (usually) obtain V_{B20} and J_{B20} more accurately (and certainly much more cheaply) by a series of dynamic rather than static computations.

6.2 Constant Overvoltage

Calculations have also been made for the same P diode at 300 K with various constant overvoltages. The external circuit used $R_s = 1 \Omega$ and $C = 1 \times 10^{-11}$ F. The initial voltage was 20 V. A log-log plot of breakdown time against applied overvoltage is shown in figure 17. The time of breakdown was arbitrarily chosen to be that which was required to attain a current density of 1×10^5 A/cm². Calculations become unstable and are halted at somewhat higher (but variable) currents. The overvoltage as plotted is adjusted for the voltage drop across R_s due to the breakdown current. The straight line in figure 17 is drawn with a slope of $-2/3$. For the overvoltage of 0.2 V, the breakdown time was also calculated with the diode temperature increasing due to the power dissipated. The breakdown time increased about 25 percent. The temperature increase at the junction is only 5 K. Longer breakdown times become costly to calculate, but it is evident that, since V increases with temperature, the time to breakdown must increase more and more rapidly as the overvoltage decreases.

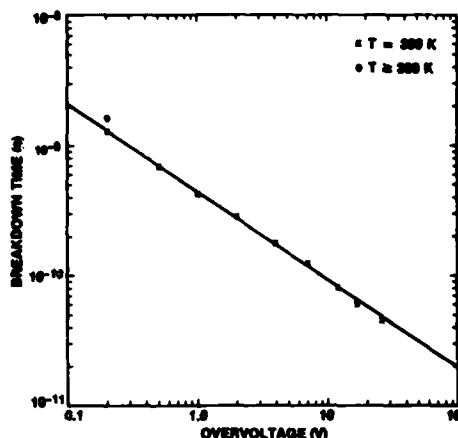


Figure 17. Log-log plot of time to breakdown versus overvoltage for P-type diode. All calculations were for a constant 300-K temperature, except for indicated point, where diode heating was simulated.

7. TEMPERATURE DEPENDENCE

7.1 Isothermal Calculations

Isothermal or constant temperature calculations have also been made at various higher temperatures for the P-type diode considered in section 6. The dynamic characteristics calculated with $dV/dt = 1 \times 10^{10}$ V/s at various temperatures are shown in figure 18. It is seen that both V_{B1} and V_{B2} increase with temperature. These calculations were made at enough different rates of dV/dt to obtain extrapolations as shown in figure 15. The results of the extrapolation are shown in table 1. Note that both V_{B1} and V_{B20} increase with temperatures for 400 and

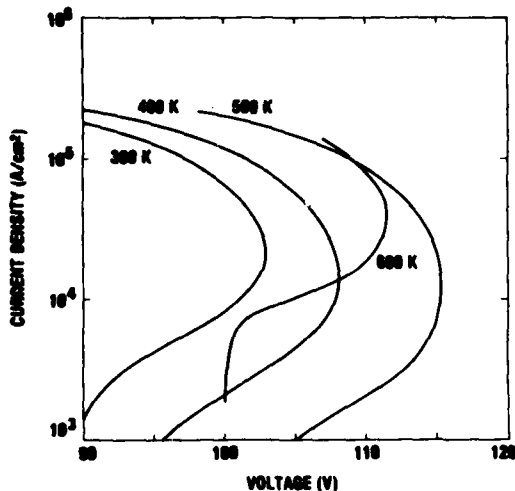


Figure 18. Dynamic characteristics of P-type diode of figure 13 at different temperatures, as labeled. Calculations were made with $dV/dt = 1 \times 10^{10}$ V/s.

TABLE 1. BREAKDOWN DATA^a FOR 4- μ m DIODES DOPED TO 5×10^{15} cm^{-3} , DIODE AREA = 1×10^{-4} cm^2

Type	T (K)	V_{B1} (V)	R^a (ohms)	V_{B2} (V)	J_{B2} (kA/cm^2)
N	300	79	2.5	94.5	23
P	300	80	6.6	101.5	16
P	400	87	9.4	105.6	9
P	500	92	18.4	112	6
P	600	88	17.6	106	12

^aData from fit to equation (29), except 600 K.

500 K, but decrease for 600 K. The increase in breakdown voltages with temperature is due to the decrease in ionization coefficients with temperature and, to a very small degree, the decrease in saturation velocities with temperature. The decrease in V_{B2} at 600 K is due to thermal injection of minority carriers into the high field region from the high doping boundary regions. This will be discussed further in the next section.

A similar series of calculations was made for a 10- μ m N-type diode doped to 4×10^{15} cm^{-3} . An area of 5×10^{-5} cm^2 was assumed, and the calculations were made with $R_s = 50$, $C = 1 \times 10^{-12}$ F, and $dV/dt = 1 \times 10^{11}$ V/s. Dynamic characteristics for various temperatures are shown in figure 19. The PTF of these diodes is about 0.65 and V_{B2} is nearly

double V_{B1} . Transit time oscillations may be noted in figure 19. At a given temperature, the frequency of oscillations increases with current, and at a given current the frequency decreases with temperature. Both of these effects are observed experimentally. The range of frequencies for this series of calculations is from 4 to 15 GHz. Avalanche oscillations will be discussed further in section 14.

The rate of temperature rise in a semiconductor is proportional to the field and the current density (see eq (6)). Figure 20 shows a plot of the rate of temperature rise for silicon as a function of current density, J , and with the electric field, E , as the parameter. To use these curves one needs to know the diode area in order to calculate J from the total current, and the diode depletion width in order to calculate E from the voltage. If the diode area and width are unknown, they may be estimated from measuring the breakdown voltage and the capacitance versus voltage curves.

The excess second breakdown voltage, ΔV_{B2} , was plotted against dV/dt for a P-type diode at 300 K in figure 15. Similar data at higher temperatures are plotted in figure 21. Also shown in the same figure are experimental measurements of Yanai et al.²¹ Their data were obtained in a study of the initiation of avalanche oscillations. It is seen that their data fit just below the 400 K calculated curve. Their

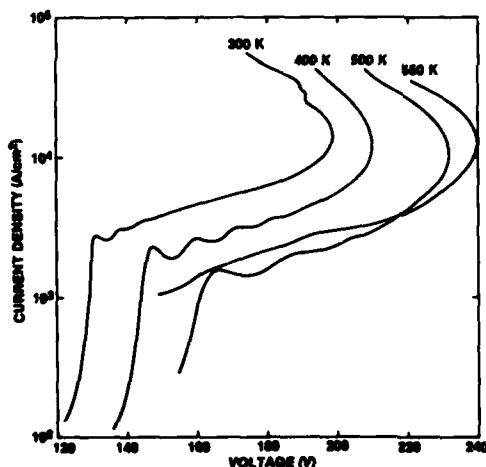


Figure 19. Change of dynamic characteristics with temperature for 10- μ m diode doped to $N = 4 \times 10^{15} \text{ cm}^{-3}$. Transit time oscillations are observed.

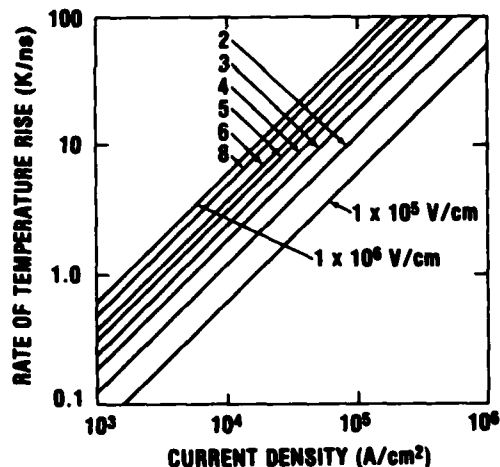
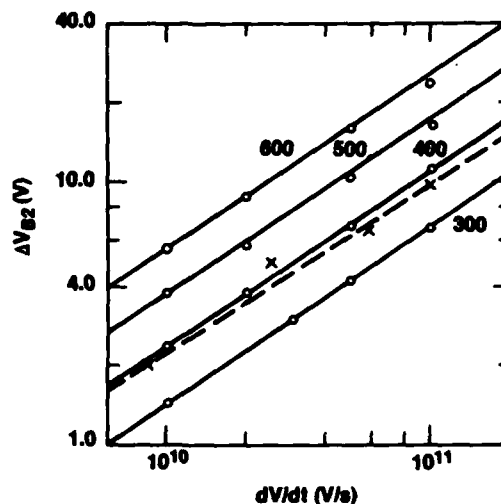


Figure 20. Rate of temperature rise for silicon diodes as function of current density. Parameter is electric field.

²¹H. Yanai, H. Torizuka, N. Yamada, and K. Ohkubo, *Experimental Analysis for the Large-Amplitude High-Efficiency Mode of Oscillation with Si Avalanche Diode*, *IEEE Trans. Electron Devices*, ED-17 (December 1970), 1067-1076.

Figure 21. Plot of overvoltage as function of rate of rise of applied voltage. Experimental data of Yanai et al (ref 21) are shown as crosses (dashed line) and computed data as circles. Solid lines are drawn with slope of 2/3. Parameter is temperature (K).



measured slope is slightly less, as would be expected if their longer pulses (low dV/dt) resulted in a higher temperature. It was stated earlier that the curves for complementary (N and P) diodes fell on the same curves. Further calculations have shown that these curves are essentially independent of doping density. The variation with temperature is predominantly a result of the decrease in the saturation velocities of the holes and electrons as the temperature increases.

7.2 Accuracy of Isothermal Calculation

The question arises as to how useful are the isothermal calculations when the temperature across the diode is not uniform. Since the total current across a diode is constant due to current continuity, the temperature rise distribution across a steady-state diode will be proportional to the field at each point. Therefore, neglecting heat flow, the temperature increase at any time will also be proportional to the field at that point: the temperature distribution has the same shape as the field distribution. Calculations were made at 300, 400, and 500 K for a 12- μm N-type diode doped to $3 \times 10^{15} \text{ cm}^{-3}$. Portions of the static characteristics at 400 and 500 K are shown in the inset of figure 22. The field-distribution calculation for 400 K at an applied voltage of 200 V was used to determine a temperature profile with an arbitrary maximum of 600 K, an increase of 300 K. The temperature increase at each of the other grid points was the same fraction of 300 K as the field at that grid point was of the maximum field. The temperature profile is shown in figure 22 as the short dashed curve. It has an average temperature of 440 K. The inset in figure 22 also shows a comparison of static characteristics for the given temperature profile (dashed line 2) and the isothermal 440-K profile (solid curve 1). The difference in current for the two profiles is quite small for 200 V

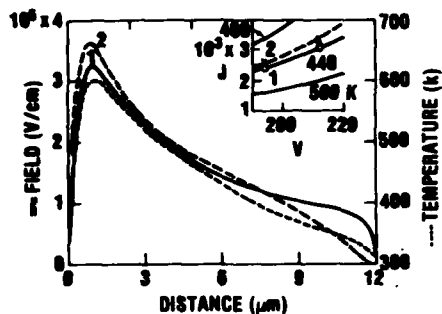


Figure 22. Variation of field profiles with temperature distribution. Inset shows portions of static characteristics for temperatures of 400, 440, and 500 K (solid lines) and for temperature distribution shown in main figure (dotted line, right scale). Average temperature of distribution is 440 K. Field distributions 1 and 2 correspond to numbered points in inset.

applied. For 220 V applied, the difference is greater. Also shown in figure 22 are the calculated field distributions for the given temperature profile (dashed curve 2) and for the same average temperature (solid curve 1). The higher maximum field for the junction at 600 K is due mainly to the temperature variation of the ionization coefficients, whereas the lower field in the low-temperature region results from the higher mobility at the lower temperature. Despite these rather large field variations, it is seen that there is no great error in using constant temperatures instead of appropriate temperature profiles in calculating static curves. Further results for the temperature variation of static and dynamic characteristics will be presented in later sections.

7.3 Silicon-on-Sapphire Diode

The silicon-on-sapphire diode used by Sunshine and Lampert²² for measurement of the temperature dependence of the current-voltage static characteristics was simulated through calculations. Their experimental measurements are shown in figure 23. Figure 23 also shows I-V characteristics calculated for $8 \times 10^{16} \text{ cm}^{-3}$. These calculations were made with $dV/dt = 1 \times 10^{10} \text{ V/s}$. Attempts to reach the steady state below the current "shoulders" were unsuccessful. When the breakdown voltage is extrapolated to $dV/dt = 0$, $N = 8 \times 10^{16} \text{ cm}^{-3}$ gives a good fit to the experimental data. An area of $5 \times 10^{-8} \text{ cm}^2$ was required to fit the current shoulder at room temperature. A diode width of $1 \mu\text{m}$ is sufficient to fit the experimental data over the range of measured data. A wider width would be required to fit the measured second-breakdown voltages (not shown), but the calculations would be much more costly and could not be made to as low currents, due to calculation instabilities.

²²R. A. Sunshine and M. A. Lampert, *Second Breakdown Phenomena in Avalanche Silicon-on-Sapphire Diodes*, *IEEE Trans. Electron Devices*, ED-19 (July 1972), 873-885.

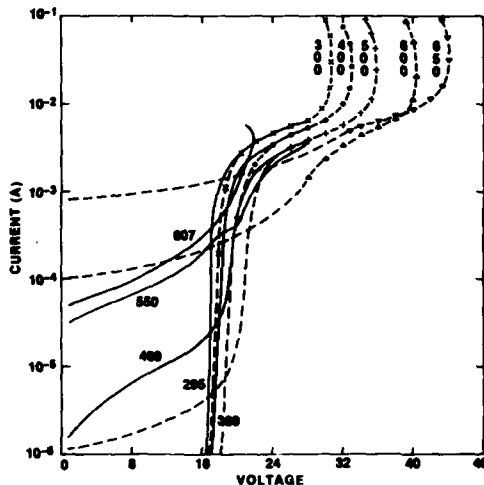


Figure 23. Measured and calculated current-voltage characteristics for silicon-on-sapphire diode with temperature (K) as parameter. Solid curves are experimental measurements of Sunshine and Lampert (ref 22). Calculation points are for 1- μ m diode doped to $8 \times 10^{16} \text{ cm}^{-3}$; $dV/dt = 1 \times 10^{10} \text{ V/s}$. Dashed-line extensions are guided by other calculations.

Sunshine and Lampert²² state that their thin film material had a carrier mobility of from 50 to 75 percent of bulk material. The low-field mobility of silicon doped to about 10^{17} cm^{-3} is only about 50 percent of undoped material. To our knowledge, no one has measured saturation velocities for heavily doped material at any temperature. Just as the temperature dependence of the saturation velocity is less than that of the low-field mobility, one would expect less dependence upon the doping level for the saturation velocity than for the low-field mobility. Moreover, one might expect less variation with temperature of the saturation velocity of highly doped material than is measured for intrinsic material. For these reasons, an option to use mobilities dependent upon doping level was not used. The particle velocities are saturated across virtually the entire depletion region, so that the use of the variation of the low-field mobility with doping level would be questionable. However, the use of the intrinsic material mobility overstates the calculated current density. If then an *a posteriori* correction is made to account for the lower mobility of the highly doped thin film material, the area used to fit the experimental data is in the range of those listed by Sunshine and Lampert.

The measured current at the maximum voltage was reported to be 11.8 mA. When the calculated currents for V_{MAX} were extrapolated to $dV/dt = 0$, a current range of from 10 to 15 mA was the best estimate. When constant applied voltages were used to better pinpoint this current, IMPATT oscillations of approximately 60 GHz were calculated.

²²R. A. Sunshine and M. A. Lampert, *Second Breakdown Phenomena in Avalanche Silicon-on-Sapphire Diodes*, IEEE Trans. Electron Devices, ED-19 (July 1972), 873-885.

There is a small difference between the measured and calculated variation of the first breakdown voltage with temperature. This could be due to the omission of field emission in the calculations. The maximum fields calculated vary from 6×10^5 V/cm at 300 K to 8×10^5 V/cm at 650 K. At these fields some field emission can be expected, since field emission dominates at 1×10^6 V/cm. Field emission increases with temperature, whereas ionization coefficients decrease with temperature. Experimentally, it has been observed that breakdown voltages decrease with increasing temperatures for diodes whose breakdown voltages are less than about 8 V. There is qualitative but poor quantitative agreement in the variation of the thermal emission current. In this case, the experimental error is probably greater. The experimental data show a large drop in the maximum voltage obtainable as the temperature exceeds 600 K. No decrease is calculated, even at 650 K, but based on other calculations, one should expect a decrease at a slightly higher temperature. If one examines the measured curve for 550 K carefully, one notes an "s" shaped curve segment in the current at about 0.2 to 0.3 mA. In the original figure, many data points are involved. One could easily dismiss this as experimental error, except one notices the same shape in the 600- and 650-K calculated characteristics.

Considering the above discussion, the overall fit between the measured and calculated characteristics is considered to be more than satisfactory. It would be useful to similarly compare diodes doped at lower levels, but no similar experimental data are known to be available.

8. THERMAL INJECTION CURRENTS

8.1 Initial Discussion

In section 4 it was pointed out that the use of low-field resistivity versus temperature curves at high fields was erroneous. Also, in the literature of second breakdown, the vague term "leakage current" is often used (or misused). What is probably meant is the reverse saturation current of the ideal diode theory. The term leakage current is misused when it is considered to be a function of the junction temperature.

In section 7 it was shown that breakdown voltages increased with temperature initially--primarily because of the decrease of ionization coefficients with temperature, but secondarily because of the decrease of saturation velocity with temperature--then decreased with temperature because of thermal injection. The process of thermal injection will now be discussed.

The reverse saturation current of the ideal diode equation has two components: a diffusion component and a thermal generation component. The ratio of these components is a function of temperature and of voltage. Practically, the diffusion component is most important in forward-biased diodes and the thermal generation in reverse-biased diodes. The current injected from the low-field boundary region into the high-field depletion region is, in this paper, termed the thermal injection current. The term leakage current is rejected because it can also pertain to surface leakage current and because it has been so often misused. The term reverse saturation current is not as descriptive in picturing the actual physical mechanism.

The thermal injection current consists of two components: electron current, AJ_{no} , injected from the cathode low-field region and hole current, AJ_{po} , injected from the anode low-field region; depending upon the types of contact, injecting or ohmic, one may dominate over the other. For most of our calculations we have assumed that $J_{no} = J_{po} = J_0$. The dependence of J_0 on temperature is the same as that of n_i^2 , given in equation (16). The experimentally measured reverse saturation currents are in poor agreement with theoretical calculations, so an arbitrary choice has been made for 300 K that $J_0 = 1 \times 10^{-7}$ A/cm. The variation of J_0 with temperature is given in figure 24.

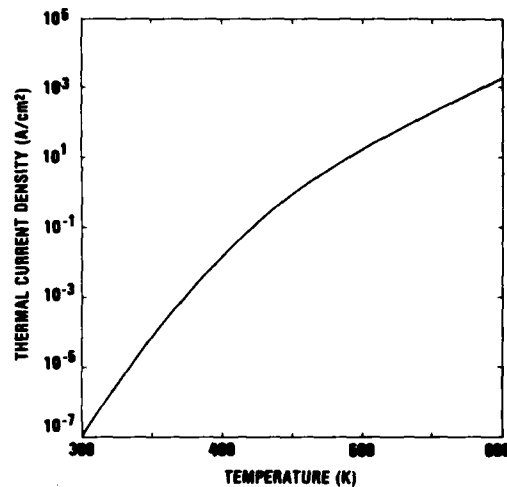


Figure 24. Assumed variation of J_0 with temperature. Variation is based on equation (16).

While the thermal generation of carriers is important in the low-field boundary regions, it is not important in the high-field depletion region, because of two phenomena. First, in practically all the calculations made with this program, the np product of the carrier densities has greatly exceeded n_i^2 once V_{B1} has been exceeded. Then, according to equation (10), recombination rather than generation will occur. However, since n_i^2 depends exponentially on temperature, it will exceed the np product at high enough temperature. Even at 600 K, where $n_i^2 = 4 \times 10^{30}$ cm⁻⁶, typical calculated np products exceed n_i^2 well below V_{B2} . Second, even when n_i^2 exceeds np, thermal generation will be minimal, since the transit time across the high-field region is so short. At the saturation velocity, this time is about 1×10^{-11} s per micrometer of distance at 300 K. This time is orders of magnitude shorter than the recombination-generation lifetime of silicon (even if gold doped). Further, the current could only increase by a factor of e

in one lifetime. Therefore, even at a temperature where $n_1^2 > pn$, little thermal generation could be expected in the high-field (temperature) regions. It is the temperature of the low-field injecting regions that is important in reducing the voltage required for current multiplication.

Returning to the discussion of the (low-field) resistivity versus temperature curves (fig. 3), it is the reduction of mobility with temperature that causes the increase of resistivity with T at the lower temperatures, whereas the decrease of resistivity with T at higher temperatures is caused by the increase of n_1^2 with T . Thus, we can expect some qualitative agreement from thermal models that use the resistivity versus temperature curves, but not quantitative agreement. The main reason that V_{B2} increases initially with temperature is the decrease of the ionization coefficients with temperature, not that of the mobility dependence. The decrease of V_{B2} at still higher temperature results from thermal injection, not thermal generation at the junction.

Before presenting results of the effect of thermal injection currents, it should be pointed out that J_0 may also be used to simulate photoinjection of carriers, to simulate the injection of emitter current into the base-collector region of a transistor, and/or to simulate the effect of ionizing radiation upon second breakdown. The last effect will be discussed in section 12.

8.2 Calculations of Thermal Injection Currents

In order to better understand the influence of temperature on diode operation, the bulk temperature effects (ionization coefficients, saturation velocities, and recombination or generation) have been separated from the boundary conditions (thermal injection). Again, in the study of the thermal injection currents, it is useful to consider separately diodes which punch through before breakdown and those not punched through at breakdown. Figure 25(a) shows characteristics calculated for a 4- μm P-type diode doped to $5 \times 10^{14} \text{ cm}^{-3}$. This diode is punched through well below breakdown and has no space-charge-limited (SCL) current region. The calculations are for 300 K and are made with $dV/dt = 2 \times 10^{10} \text{ V/s}$. V_{B2} is seen to be reduced as J_0 is increased, but the current at second breakdown increases. Similar calculations were made for the complementary N-type diodes. The results are shown in figure 25(b). Also shown in the figure are calculations made with J_{no} unequal to J_{po} . It is seen that J_{no} , the electron injection current density, is more effective than the hole injection current. This results from the higher ionization coefficient for electrons than for holes in silicon. When the multiplication factor, that is, $M = J/J_0$, is plotted against voltage for these punched-through diodes, the curves all merge into a single curve, with deviations occurring at low M values due to initial conditions, and at high M values due to space-charge distortion and double avalanching.

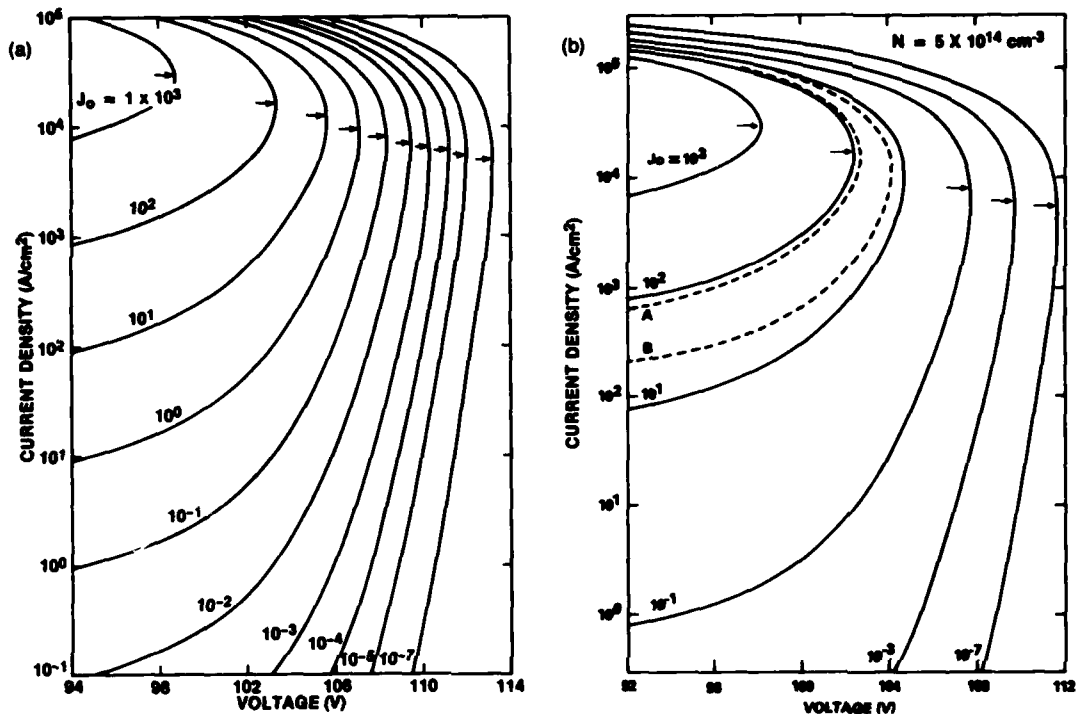


Figure 25. Calculated dynamic characteristics for (a) 4- μm P-type diodes, doped to $5 \times 10^{14} \text{ cm}^{-3}$. Parameter is J_0 in A/cm^2 . Arrows indicate voltage maxima. Calculated dynamic characteristics of (b) N-type diodes, doped to indicate voltage maxima. Dashed curve A is for $J_{n0} = 10^2$ and $J_{p0} = 10^1$; curve B is for $J_{n0} = 10^1$ and $J_{p0} = 10^2$. Calculations were made with $dV/dt = 2 \times 10^{10} \text{ V/s}$.

Calculations were also made with $J_0 = 1 \times 10^{-7} \text{ A/cm}^2$, corresponding to room temperature, but with constant elevated temperatures for the bulk of the P-diode. The results are shown in figure 26 as the dashed curves. Since this condition assumes no heat flow to the low-field regions, this will be termed the adiabatic case. Also shown in the same figure are characteristics where both the bulk and thermal injection region are at the same temperature--the isothermal case. The maximum voltages, V_{B2} , for each case are plotted as a function of temperature in figure 27. When the thermal injection region is kept at room temperature, V_{B2} increases more and more rapidly at higher temperatures, but, with increasing thermal injection, a maximum is reached at about 500 K. The rate of decrease in V_{B2} with temperature becomes continuously greater above the temperature for maximum voltage.

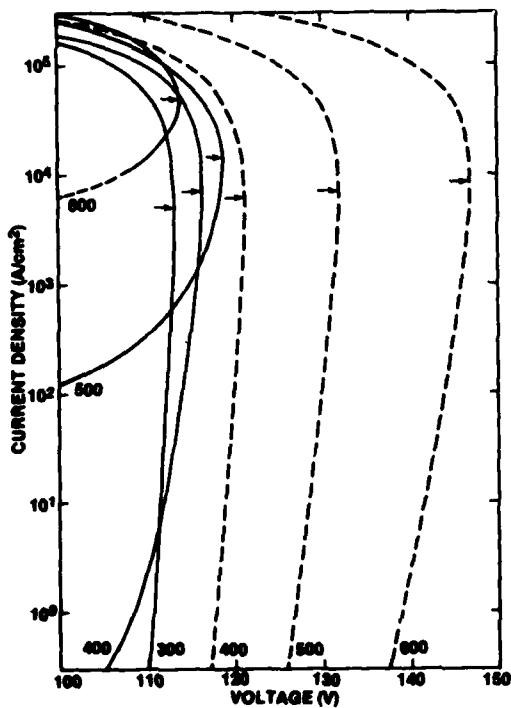


Figure 26. Characteristics for diode of figure 25(a) with bulk temperature (K) as parameter. For 300 K and dashed curves, $J_0 = 1 \times 10^{-7}$ A/cm². For solid curves J_0 is determined by temperature according to figure 24. Arrows indicate current density for maximum voltage.

While there is some lowering of V_{B2} with increasing J_0 , even at the lowest value of J_0 used for the punched-through diodes discussed thus far, this is not true for diodes not punched through at breakdown. Calculated characteristics as a function of J_0 for a P-type diode of the same width, but doped to 5×10^{15} cm⁻³ (a factor of 10 larger), are shown in figure 28. This diode is not punched through at breakdown and a regime of SCL current is noted. The SCL regime, where the I-V characteristic is linear, shows up on the semilog plot as a curved region. For $1 \times 10^{-7} < J_0 < 1 \times 10^{-2}$, no difference is noted in the calculated characteristics. At higher J_0 values, the decrease in V_{B2} is again observed. A comparison of the decrease in V_{B2} as a function of J_0 for each of the diodes is shown in figure 29. For high values of J_0 , the lowering of V_{B2} is comparable.

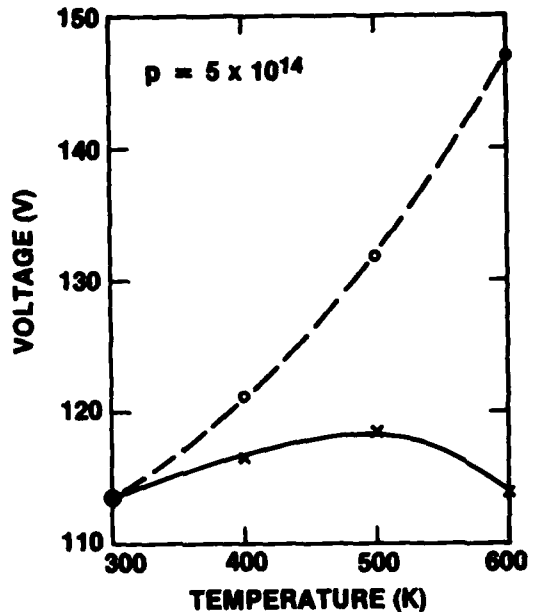


Figure 27. Second breakdown voltage as function of temperature for diode of figure 26. Thermal injection current is determined by bulk temperature (isothermal calculation) for solid curve, whereas thermal current corresponds to 300 K (adiabatic calculation) for dashed curve.

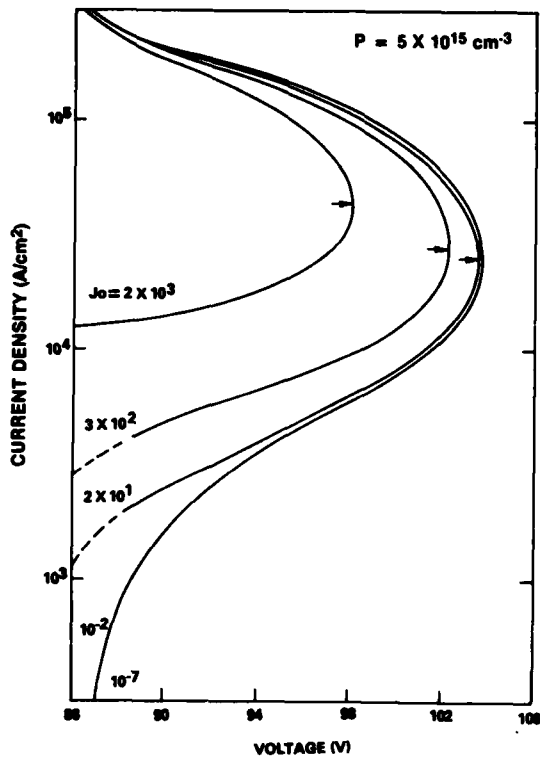
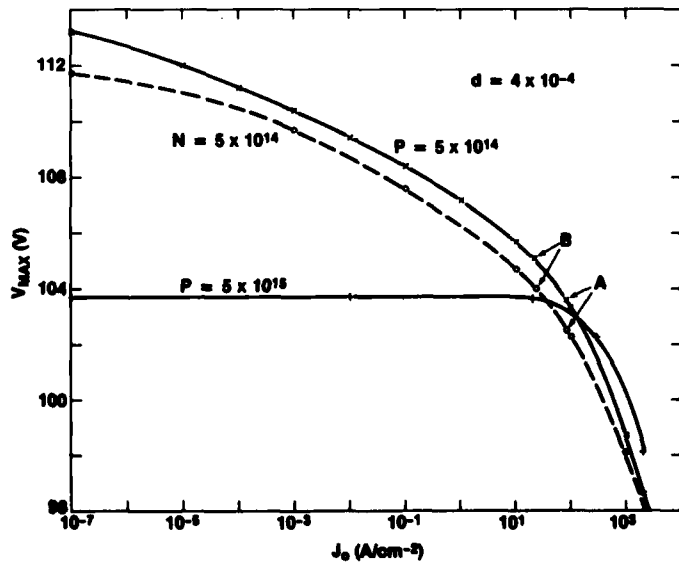


Figure 28. Calculated dynamic characteristics for 4- μm P-type diode, doped to $5 \times 10^{15} \text{ cm}^{-3}$, as a function of J_0 . No lowering of V_{B2} is noted for this punched-through diode as J_0 is increased from 10^{-7} to 10^{-2} A/cm^2 .

Figure 29. Plots of V_{B2} for 4- μm diodes as function of J_0 . Doping density (cm^{-3}) is indicated for each curve. Points A and B are defined in figure 25.



Characteristics for the higher doped diode were also calculated for both the adiabatic and isothermal cases at higher temperatures. The calculations were made at $dV/dt = 1 \times 10^{10}$ V/s and also at higher rates to allow extrapolation to $dV/dt = 0$. The results are shown in figure 30. The isothermal and adiabatic curves are the same up to nearly 500 K; 500 K corresponds to a J_0 value of 20 A/cm². Only the isothermal data were extrapolated to $dV/dt = 0$.

The calculations of this section show the importance of the thermally injected current, J_0 . The implications of this effect in comparing differing doping profiles will be discussed in section 10.

9. VARIATION OF DIODE WIDTHS AND DOPING DENSITIES

9.1 Varying Doping Densities

In section 5 it was shown that for a constant diode width, the V_{B1} and R_{sc} varied as the doping level was changed by a factor of 2 but V_{B2} was essentially unchanged. These observations are valid over a much wider range of doping levels. Figure 31 shows the family of characteristics for a 4- μ m P-type diode at 300 K, with doping ranging from 1×10^{15} to 2×10^{16} cm⁻³. Again, these characteristics were calculated with $dV/dt = 1 \times 10^{10}$ V/s to reduce costs and printout paper. As may be seen from the values of V_{B1} and V_{B2} , the dynamic characteristic agrees quite well with the data given in the previous section for static calculations. Note in figure 31 that while V_{B1} varies from about 45 to 105 V, V_{B2} varies only by about 3 V. The arrows in figure 31 indicate the current density, J_{B2} , for the maximum voltage. Note also that J_{B2} increases with the doping level. This is expected, since it was shown in the previous section that double avalanching occurs when the mobile carriers exceed the doping level. The punch-through factor (PTF) varies from about 0.4 for the doping level of 2×10^{16} cm⁻³ to about 7 for the doping of 1×10^{15} cm⁻³. The use of approximate numbers may be explained by the consideration of figure 32. The space-charge free

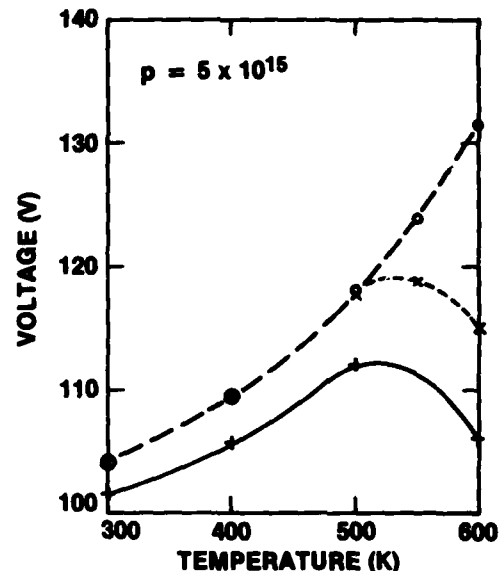


Figure 30. Second breakdown voltages for diode of figure 28 as function of temperature. Dashed curves are for $dV/dt = 1 \times 10^{10}$ V/s. Crosses indicate isothermal calculation and open points indicate adiabatic calculations. Solid curve (pluses) indicates V_{B2} extrapolated to $dV/dt = 0$. (See fig. 16.)

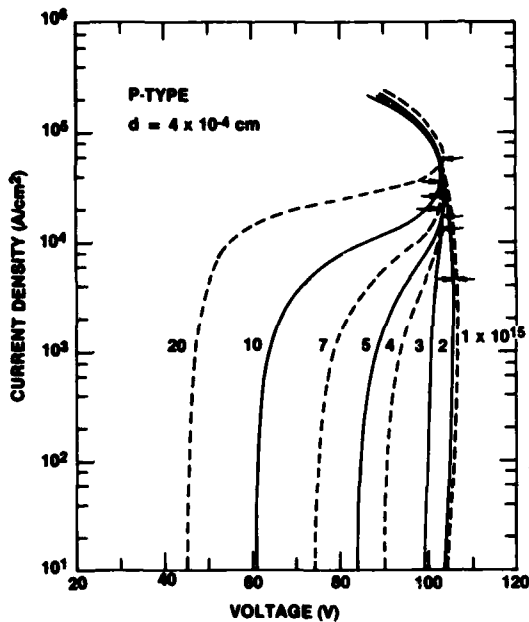


Figure 31. Characteristics of 4- μm P-type diode with doping level in cm^{-3} as parameter. Calculations were made with $dV/dt = 1 \times 10^{10}$ V/s. Alternating solid and dashed lines are used only for clarity.

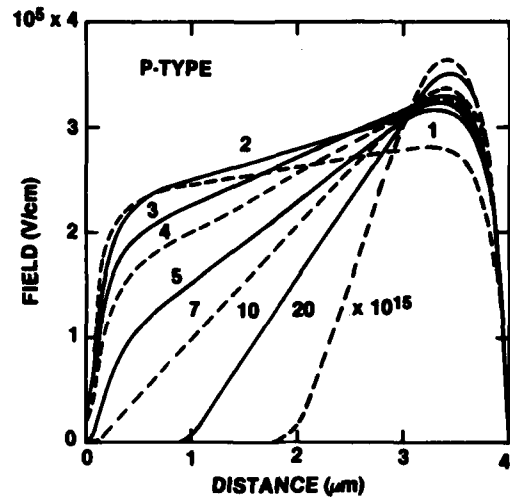


Figure 32. Distributions of electric field across diode of figure 31. Currents are all in SCF current regime.

(SCF) field distribution across each diode of figure 31 is plotted in figure 32. These fields are determined by the doping profiles simulated, since space charge from mobile carriers is negligible. While the N^+P junction is exactly defined, the gradual increase in doping at the PP^+ junction leads to an uncertainty in the width of the depletable region and thus to an ambiguity for the PTF.

The variation of the field distribution with current density is shown for the diode with a doping level of $2 \times 10^{16} \text{ cm}^{-3}$ in figure 33. Note the apparent similarity of the curves in figures 32 and 33. This results from the compensation by the mobile holes for more and more of the fixed doping charge as the current increases. As noted earlier, the number density of holes rises exponentially in the high-field junction region and is relatively constant in the low-field region. At J_{B2} , the field distribution is quite similar for all doping levels as might be expected from the similar V_{B2} values.

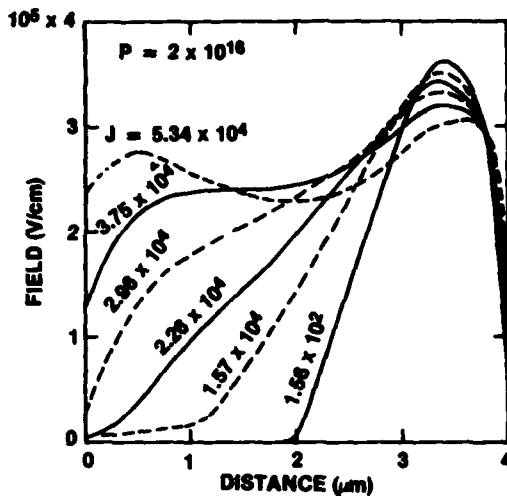
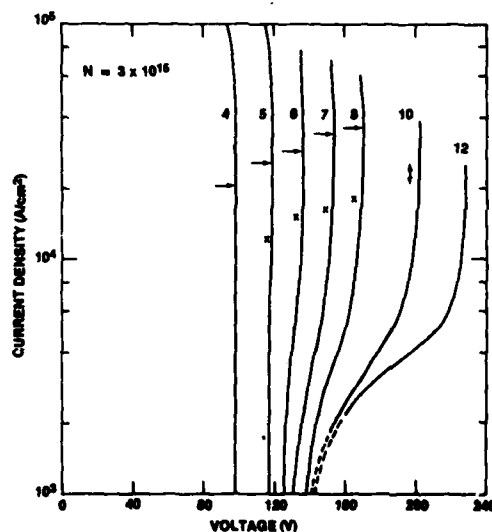


Figure 33. Field distributions across $P = 2 \times 10^{16} \text{ cm}^{-3}$ diode for various current densities (A/cm^2). Calculations were made with $dV/dt = 1 \times 10^{10} \text{ V/s}$.

9.2 Varying Widths

A second family of diodes of interest is that with the same doping density, but with varying widths. Figure 34 shows 300 K characteristics for N-type diodes doped to $3 \times 10^{15} \text{ cm}^{-3}$ and with width varying from 4 to 12 μm . Again these are dynamic characteristics, calculated with $dV/dt = 1 \times 10^{11} \text{ V/s}$; horizontal arrows indicate current for voltage maxima. Also shown by crosses are the values of V_{B2} and J_{B2} obtained by making calculations at higher dV/dt values and extrapolating to $dV/dt = 0$. For the two diodes of extreme widths, meaningful extrapolations could not (easily) be made. The current extrapolation was uncertain for the 10- μm diode. The dashed curves at low J for the 10- and 12- μm diodes are extrapolations of the computer data. Since the PTF is less than 1 for these diodes, V_{B1} is the same as for the 8- μm diode. The field distribution at low J values for each diode is shown in figure 35. The diode widths are not labeled, but can be identified by the point where E approaches zero. Also shown is the field distribution for the 12- μm diode at a current in the double avalanche region.

Figure 34. Characteristics of N-type diodes doped to $3 \times 10^{15} \text{ cm}^{-3}$. Diode width is given in μm for each curve. Calculations are for $dV/dt = 1 \times 10^{10} \text{ V/s}$. Horizontal arrows indicate current density for maximum voltage. Crosses indicate extrapolated values of V_{B2} and J_{B2} . Vertical double arrow indicates range of uncertainty in current density for 10- μm diode.



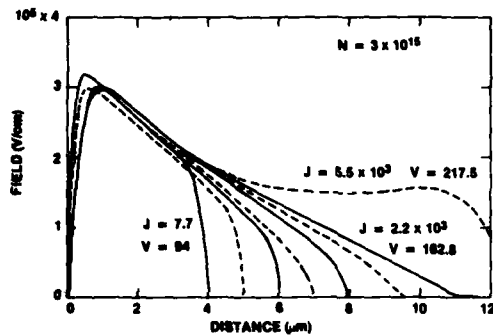


Figure 35. Field distributions across $3 \times 10^{15} \text{ cm}^{-3}$ diodes of various widths of figure 34 at low current densities. Also shown is field across 12- μm diode in double-avalanche current regime.

9.3 Whole Families

One needs a three-dimensional plot to present breakdown voltages as a function of both doping level and diode width for the entire family of diodes with constant doping levels. However, the same data may be presented on two-dimensional plots, with the other variable as a parameter. Sze¹⁶ shows a log-log plot of V_{B1} versus doping density for one-sided abrupt P-N junctions. His curves were calculated with the use of the ionization coefficients of Lee et al²³ and are reproduced in figure 36. Also shown in figure 36 are the V_{B1} and V_{B2} data of this work. The data are for either P- or N-type diodes; the small difference does not show on this voltage scale. Dashed lines connect the family of diodes with the same width. The agreement of the present data with Sze's data seems satisfactory. The difference is that which is expected from the different ionization coefficients used. In figure 36, all non-punched-through diodes fall along a common diagonal line independent of width. As the diode width decreases, punch-through occurs at larger doping densities. V_{B1} is essentially constant, independent of doping level, but a function of diode width, for diodes that are well punched through. The short curved segments between the straight lines correspond to $\text{PTF} \approx 1$.

Sze¹⁶ states that for non-punched-through diodes of Si, Ge, GaAs, and GaP, V_{B1} can be approximated by

$$V_{B1} = 60(E_g/1.1)^{3/2} (N/10^{16})^{-3/4} \quad (31)$$

For silicon, $E_g = 1.12 \text{ eV}$, so that for silicon

$$V_{B1} = 62(10^{16}/N)^{3/4} \quad (32)$$

¹⁶S. M. Sze, *Physics of Semiconductor Devices*, Wiley-Interscience, New York (1969), 39-41, 57-59, 121-126.

²³C. A. Lee, R. A. Logan, R. L. Batdorf, J. J. Kleimack, and W. Wiegmann, *Ionization Rates of Holes and Electrons in Silicon*, *Phys. Rev.*, A134 (May 1964), A761-773.

Our data fit closely to

$$V_{B1} = 65(10^{16}/N)^{2/3} \quad (33)$$

Grove²⁰ shows that the measured V_{B1} data for silicon have a slope less than three-fourths. The fit of that experimental data²⁴ to equation (33) is shown in figure 37.

The merged curve of figure 36 may be separated by plotting V_{B1} against diode width, as shown in figure 38. Now the data for the punched-through diodes are merged into the single curve applicable for intrinsic material. The equation for intrinsic material is

$$V_{B1} = 36d^{0.81} \quad (34)$$

as compared to

$$V_{B1} = 33d^{0.92} \quad (35)$$

for Sze's data. One cautionary word is necessary here. The width of the entire high-field region has been used for d in equation (34), whereas the usual practice is to use the width of the low doping region.

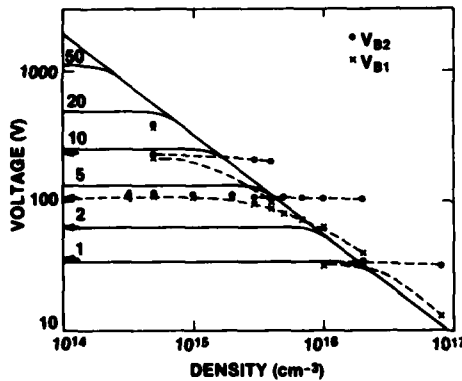


Figure 36. First (V_{B1}) and second (V_{B2}) breakdown voltages as function of doping density. Diode width in μm is given as parameter. Solid curves are V_{B1} curves taken from Sze (ref 16). Dashed curves connect calculated points of same diode width. Arrows at left indicate calculations for intrinsic diodes.

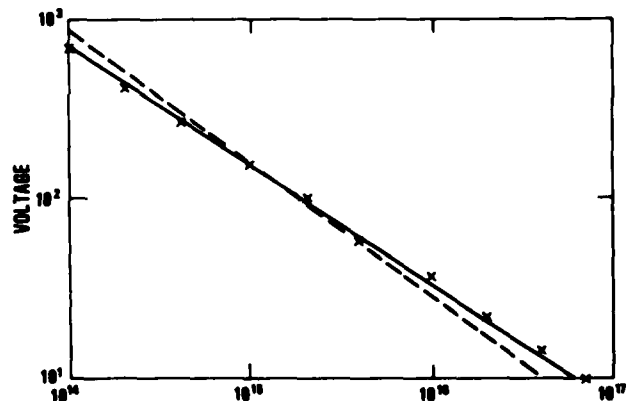


Figure 37. Comparison of measured and calculated V_{B1} variation with doping density. Points are experimental measurements of Miller (ref 24). Dashed line is equation (33) from Sze (ref 16) and solid line is equation (33) from our calculations.

²⁰A. S. Grove, *Physics and Technology of Semiconductor Devices*, John Wiley and Sons, New York (1967), 44-52, 194-201.

²⁴S. L. Miller, *Ionization Rates for Holes and Electrons in Silicon*, *Phys. Rev.*, 105 (February 1957), 1246-1249.

A third way to plot breakdown voltages is to use V_{B1} as a parameter on a log-log plot of d as ordinate and N as abscissa. This plot eliminates the merged curves, as shown in figure 39. It gives an overall picture of the breakdown voltages of all possible combinations of N and d . A great majority of diodes fall in or near the curved regions where the PTF is near unity.

For the abrupt one-sided junction with constant doping $dE/dx = eN/\kappa\epsilon_0$, equation (5), when mobile carriers can be neglected. Thus, below breakdown,

$$V = eNd^2/2 \kappa\epsilon_0 \quad (36)$$

This is the basic equation to determine the doping profile from capacitance measurements as a function of reverse bias. Knowing the area, the capacitance determines d , allowing N to be determined. Plots of V for silicon as a function of N with d as parameter are shown in figure 40. The intersection of these curves with the V_{B1} curve gives the PTF = 1 position. Equating equation (36) with equation (33), we find

$$V_{B1} = C'N^{-2/3} = C''Nd_B^2 \quad (37)$$

or

$$d_B = C'''N^{-5/6}$$

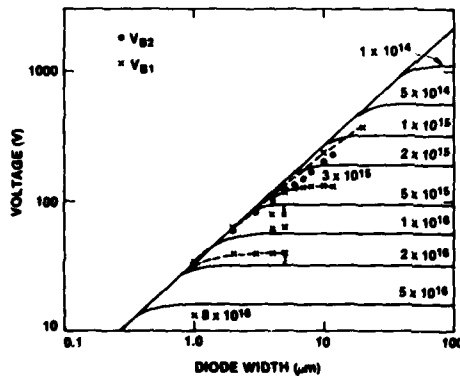


Figure 38. Same breakdown data plotted against diode width and with doping density (cm^{-3}) as parameter. Solid curves are from Sze (ref 16) and points are results from our calculations.

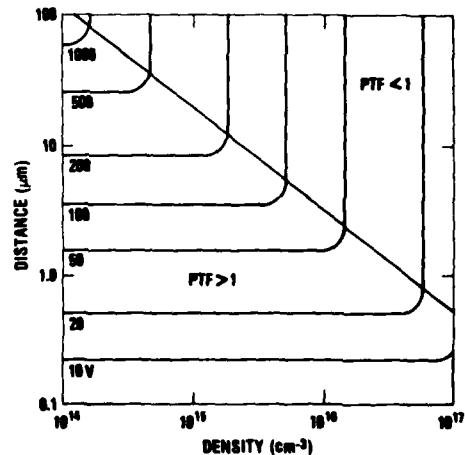


Figure 39. First breakdown voltages plotted as parameter for variations in both diode width and doping density. Diagonal line is locus of points for PTF = 1.

This shows that the depletion region at breakdown varies (inversely) slightly less than linearly with doping. Equation (37) is again the condition for $PTF = 1$ and is also shown in figure 39. Since for constant doping,

$$E_{\max} = 2V/d,$$

we find, by using equation (37) for the breakdown condition, that

$$E_{\max} = C''N^{1/6} \quad (38)$$

This shows that the junction field at breakdown is not constant as often assumed, but varies slightly with the doping density. A plot of calculated E_{\max} at breakdown as a function of N is shown in figure 41.

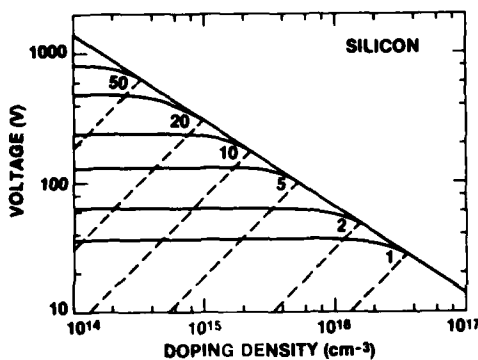


Figure 40. Calculated V_{B1} as function of doping density for various diode widths, from equations (33) and (34). Dashed lines give depletion width for voltages below breakdown. Each intersection with solid diagonal lines indicates that $PTF = 1$ for that doping.

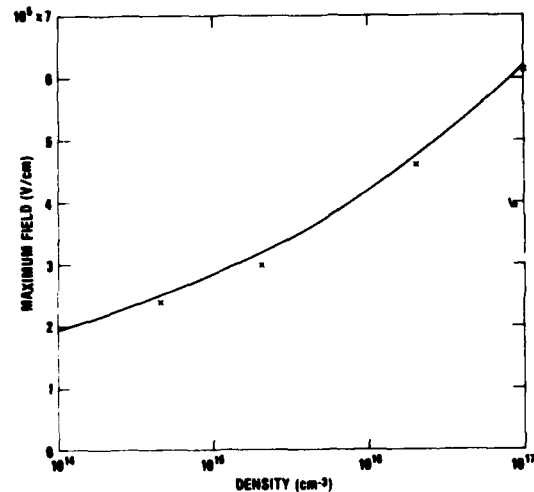


Figure 41. Maximum field at breakdown as function of doping density. Curve is plot of equation (38); points are for diffused one-sided junctions.

10. DIFFERING DOPING PROFILES

The doping profiles considered in the previous sections were one-sided diffuse junction diodes. Most approximations of semiconductor breakdown have assumed abrupt junction one-sided diodes. This approximation is often valid and does make junction positions and, therefore, depletion widths, PTF 's, etc, more definite. It also facilitates comparison with other calculations.

10.1 One-Sided Diodes

Calculated static current-density/voltage characteristics for abrupt junction one-sided diodes at 300 K are shown in figure 42. The doping levels are $1 \times 10^{17} \text{ cm}^{-3}$ for diode widths of 0.4, 0.5, and 0.6 μm and $2 \times 10^{17} \text{ cm}^{-3}$ for a 0.3- μm diode. The diodes are P-type except for one N-type diode. Carrier densities across the N-type diode are shown in figure 43. The electric field distributions across the same diode at the same current densities are shown in figure 44. Similar field distributions across the complementary (same width and doping level) P-type diode are shown in figure 45.

For the lowest voltages shown in both figures 44 and 45, the field is linear from the junction to the edge of the high doping region. Since these voltages are essentially first breakdown voltages (V_{B1}) for these diodes, the PTF = 1. The 0.6- μm diode does not punch through at breakdown (PTF = $0.5/0.6 = 0.83$), so its V_{B1} is equal to that of the 0.5- μm diode, as may be seen in figure 42. The 0.4- μm diode punches through before breakdown (PTF = $0.5/0.4 = 1.25$); hence, its V_{B1} is less than that for the wider diode. The transition from the quadratic current dependence upon voltage for the 0.4- μm diode to the linear dependence for the 0.6- μm diode may also be seen in figure 42.

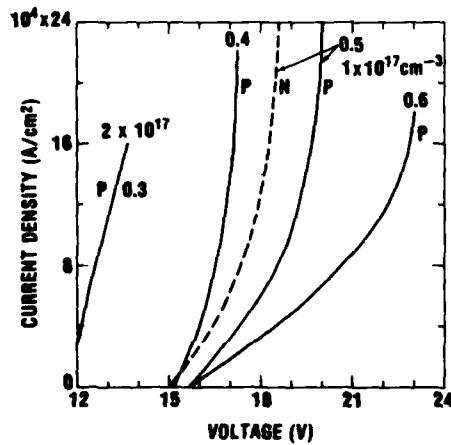


Figure 42. Calculated characteristics for abrupt one-sided diodes. One curve is for doping of $2 \times 10^{17} \text{ cm}^{-3}$; other curves are for $1 \times 10^{17} \text{ cm}^{-3}$. Diode width is given for each curve. Dashed curve is for N-type device; other curves are for P-type devices.

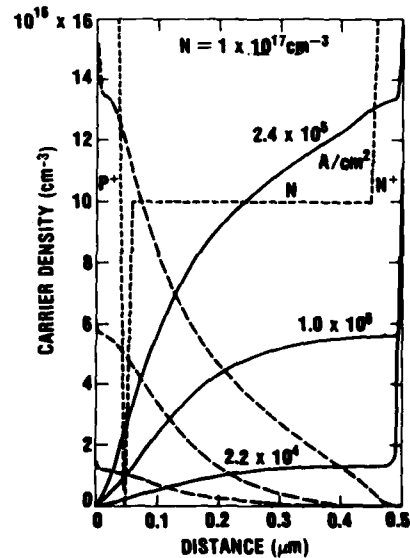


Figure 43. Carrier densities for N-type diode of figure 42. Doping profile is given by short-dashed curve; electron density is given by solid curves; hole density is given by long-dashed curves. Parameter is current density.

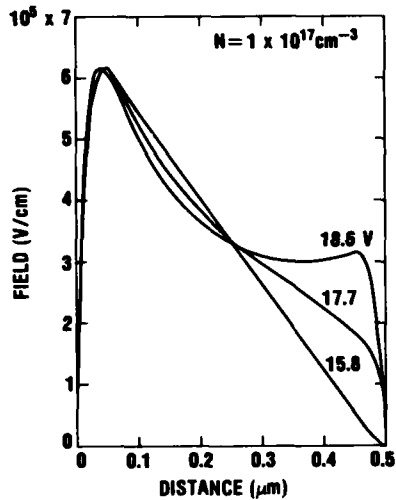


Figure 44. Field distributions corresponding to carrier profiles of figure 43. Diode voltage is curve parameter.

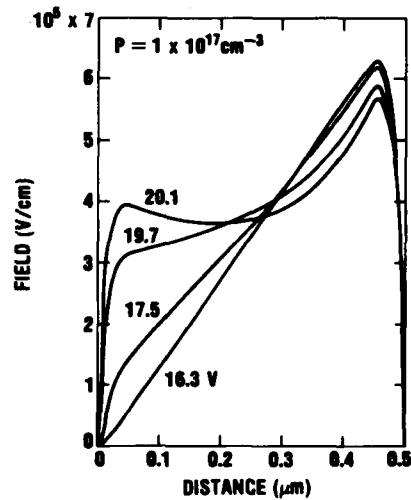


Figure 45. Field distributions for P-type diode which is complementary to diode of figure 44. Again, diode voltages are given.

As shown in figure 42, the P-type diode has a higher V_{B1} than does the complementary N-type diode. The P-type diode also has a higher space-charge resistance than does the N-type diode, as noted by the voltage difference increasing with current.

At the intermediate current level shown in figure 43, the space charge of the mobile carriers becomes an appreciable fraction of the doping level, and the field profile is no longer linear (fig. 44). At the highest current level shown in figure 43, the electron density exceeds the sum of the doping level and the hole density. This results in a field minimum (saddle) as shown in figure 44.

The peak electric field at the junction is essentially constant, independent of voltage (above V_{B1}) for the N-diode, as shown in figure 44. The field maximum does, however, move slightly from the junction toward the P^+ doping region. The peak field for the P-diode decreases with voltage as the voltage increases above V_{B1} , as shown in figure 45. At low current, the maximum field for the P-diode slightly exceeds that for the N-diode, but at higher currents it drops appreciably below the constant field maximum of the N-diode. The total voltage difference between the two diodes at the same current increases because the space-charge field in the P-diode increases with current

faster than it does in the N-diode. The saddle appears at about a 20 percent larger field for the p-device. These differences arise from the higher ionization rate for electrons than for holes in silicon.

The results reported in this section for the abrupt one-sided diodes differ minimally from those reported in the previous sections for diffuse-junction one-sided diodes. The maximum field is more sharply pointed for the abrupt doping profile.

10.2 Two-Sided Diodes

Static current-density/voltage characteristics for abrupt two-sided diodes doped to $1 \times 10^{17} \text{ cm}^{-3}$ are shown in figure 46. A logarithmic current-density scale is used to cover a wide current range. These characteristics were calculated point by point, since errors resulted even at low dV/dt rates. The PTF equals 1 for the 0.8- μm diode. The small ellipses at the highest current densities indicate IMPATT oscillations²⁵ for three of the diodes. Avalanche oscillations will be discussed in section 14. The doping profile and the mobile carrier densities are shown in figure 47 for the 0.8- μm diode. The corresponding field distribution at each current density is shown in figure 48. For the symmetric two-sided diode doped to $1 \times 10^{17} \text{ cm}^{-3}$, PTF = 1 for a 0.8- μm width. All diodes wider than 0.8- μm have equal V_{B1} , but narrower diodes have lower V_{B1} . The field distribution at breakdown has the form of an isosceles triangle. At higher currents, the effect of the mobile space charge is to lower the peak field at the junction as it is raised near each diode edge (fig. 48). The effect is to broaden the region wherein current multiplication occurs, as may be seen in figure 47. The higher fields in the P region than in the N region again result from the difference in the ionization rates for electrons and holes.

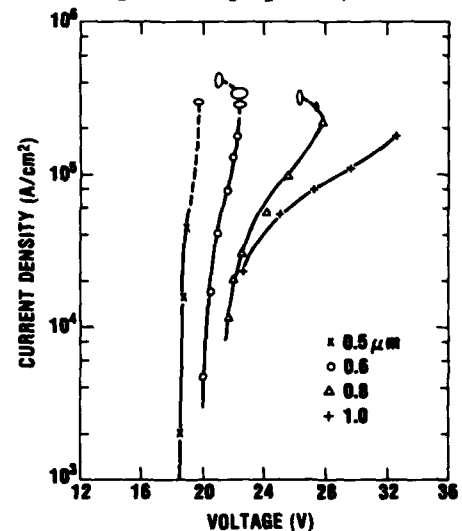


Figure 46. Characteristics of symmetric two-sided diodes doped to $1 \times 10^{17} \text{ cm}^{-3}$ for four diode widths. Ellipses at highest currents are equilibrium IMPATT oscillations. Voltage for 0.8- μm diode at $J = 6 \times 10^4 \text{ A/cm}^2$ is high because too low doping used in N^+ and P^+ regions for this current.

²⁵A. L. Ward, *Modes of Avalanche Oscillations in Silicon Diodes*, IEEE Trans. Electron Devices, ED-25 (June 1978), 683-687.

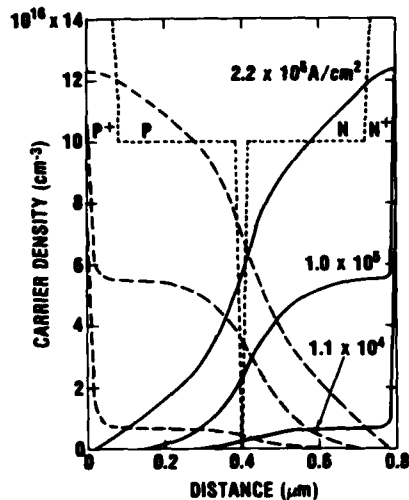


Figure 47. Carrier densities for symmetric two-sided diode doped to $1 \times 10^{17} \text{ cm}^{-3}$. Doping profile is shown as dotted curve, electron densities as solid curves, and hole densities as dashed curves. Parameter is current density.

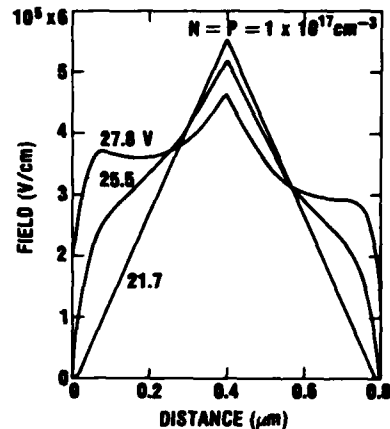


Figure 48. Field distribution corresponding to densities of figure 47. Diode voltage is given for each distribution.

10.3 Linearly Graded Diodes

Static current-density/voltage characteristics for linearly graded doping profiles are shown in figure 49. Again, the current-density scale is logarithmic to cover the range of interest. Three doping gradients are illustrated: 1×10^{20} , 1×10^{21} , and $1 \times 10^{22} \text{ cm}^{-4}$. Diode widths are 4, 5, and 8 μm ; 1.6 and 2.0 μm ; and 0.5 and 1.0 μm , respectively. Higher current densities are required for space-charge effects to appear for the higher doping gradients. Recall that the currents increase exponentially in the SCF current regime, but increase less rapidly with voltage due to the mobile carrier's space-charge resistance. The doping profile and the carrier densities across the 5- μm diode with a doping gradient of $1 \times 10^{20} \text{ cm}^{-4}$ are shown in figure 50. Both N and P doping are shown as positive in all figures; there is no change in gradient at the metallurgical junction. The corresponding field profiles are shown in figure 51. For low currents, the field is parabolic; with increased current density, the field maximum decreases and moves into the P^+ region. The PTF equals 1 for a 4- μm diode with a gradient of $1 \times 10^{20} \text{ cm}^{-4}$. For the 5- μm diode shown in figure 51, the depletion (high-field) region widens at higher currents. At the highest current shown, the field distribution closely resembles that for a lightly doped (PTF > 1), N-type, broadly diffused junction diode. In fact, at even higher current densities, field distributions tend to become independent of doping profiles.

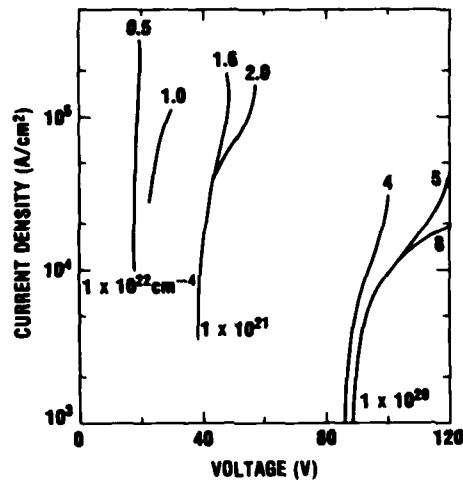


Figure 49. Characteristics of three families of linearly graded diodes, with gradients of 1×10^{20} , 1×10^{21} , and $1 \times 10^{22} \text{ cm}^{-4}$. Diode width is parameter for each curve.

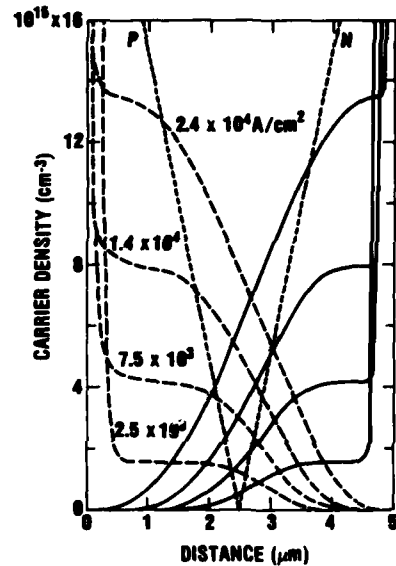


Figure 50. Carrier densities for 5- μm diode with linear doping gradient of $1 \times 10^{20} \text{ cm}^{-4}$. Doping densities--straight dotted lines--are all plotted as positive numbers. Electron densities are given by solid curves and hole densities by dashed curves. Current densities are given.

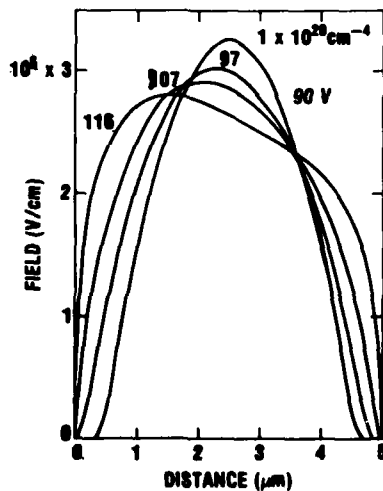


Figure 51. Field distributions corresponding to current densities of figure 50. Diode voltage is given for each distribution.

10.4 Other Doping Profiles and Discussion

With the advent of the use of ion implantation to form P-N junctions, other doping profiles are feasible. In particular, high-low (Hi-Lo) and Lo-Hi-Lo profiles, both single- and two-sided, have been used with advantage in IMPATT diodes. It is planned to make calculations simulating these profiles, since they should have superior thermal properties.

It was shown in section 8 that thermal injection currents play a major role in second breakdown for times greater than the thermal time constant. For short times, essentially adiabatic conditions, the temperature distribution is qualitatively the same as the field distribution. Therefore, the field distributions calculated in this section can be used to study the effect of doping profiles upon temperature distributions. Two-sided diodes have their highest temperature farther from the low-field thermal injection regions than do one-sided diodes. Abrupt two-sided diodes have smaller temperature gradients at the low-field boundary than do linearly graded diodes. Thus, the former should have smaller thermal injection currents and be less susceptible to second breakdown than the latter. The two-sided Hi-Lo or Lo-Hi-Lo diodes have even smaller temperature gradients at the low-field boundary and should be the least susceptible to second breakdown. Of the one-sided diodes, the P-diode should be superior to the N-diode, since the high-temperature junction region of the former is farther from the source of the thermally injected electrons, which ionize more easily than do holes.

In conclusion, we predict the following order, from the most susceptible to thermal damage to the least, of doping profiles: (1) one-sided N-diodes, (2) one-sided P-diodes, (3) linearly graded diodes, (4) abrupt two-sided diodes, and (5) Lo-Hi-Lo two-sided diodes. Experimental tests will be required to verify these predictions.

11. EXTENDING THE TIME SCALE

The most serious limitation of the computer program is the cost limit of simulating problem times of more than a few nanoseconds. Generally, the time step is limited by the dielectric relaxation time, but in all cases there is also a transit-time limitation which is also important. At the room-temperature saturation velocity, the transit time is approximately 10 ps for each micrometer of diode width. One transit-time effect is the generation of avalanche oscillations. It will be shown in section 14 that the presence of oscillations has a marked effect on the current-voltage characteristic of a diode. At times when the current is quasi-stationary, when $dI/dt < \epsilon$ (where ϵ may be chosen by experience), it should be possible to use large values of Δt to solve the thermal diffusivity equation (eq (6)) and then use small values of Δt to solve the electronic equations with the new temperature distribution.

11.1 Procedure

Since the present computer program is limited to the nanosecond time regime, it is useful to explore ways of obtaining information at longer times. One method is to combine the calculated static

characteristics at various temperatures with the knowledge of the temporal rate of temperature rise. The rate of temperature rise as a function of current density and field for silicon was given in figure 20. The procedure is illustrated for a 4- μm P-type diode doped to $5 \times 10^{15} \text{ cm}^{-3}$. The 300 K, $dV/dt = 1 \times 10^{10} \text{ V/s}$ characteristic of this diode was shown in figure 13. This characteristic, together with those at selected higher temperatures, is shown in a linear plot in figure 52 (p 60). Load lines corresponding to $R_s = 50 \Omega$ and an area of $5 \times 10^{-5} \text{ cm}^2$ are also shown in the figure for applied voltages of 120, 130, 180, and 230 V. The calculated temporal rate of temperature rise as a function of J is shown in figure 52(d) for temperatures of 300, 400, and 500 K. The temperature increase rate is greater at higher temperatures, since higher fields are required to obtain the same current density.

To proceed, consider the 180-V load line (the second from the top in fig. 52(a)). The current density at 300 K is $3.1 \times 10^4 \text{ A/cm}^2$. As shown in figure 52(d), the temperature increases 5 K per nanosecond at 300 K for $J = 3.1 \times 10^4 \text{ A/cm}^2$. Therefore, 20 ns are required to reach 400 K at the applied voltage. The intersection of the load line with the 400 K characteristic gives new J and V values. Thus, J versus time curves are constructed point by point, as shown in figure 51(b). Similarly, V versus t curves are constructed, as illustrated in figure 52(c) for an applied voltage of 120 V. These curves show an initial increase of V and a decrease of J with time, followed by a decrease in V and increase of J, indicating the onset of second breakdown. Other applied voltages may be used to extend the time-to-breakdown scale to higher and lower values.

The curves of figure 52(b) and (c) may be used to plot power as a function of time. A log-log plot of the average power versus the breakdown time is shown in figure 53 (p 61). Breakdown time in this case is determined by the time to reach 600 K. The slope of this curve is 1.16. Experimental measurements in this time range usually have a slope of about one on the log-log plot.

11.2 Simulation of 1N4148

Extensive experimental studies²⁶ have been made on second breakdown in the switching diode, 1N4148. This diode has an N-Epi region of 11 μm , doped to $1.5 \Omega\text{-cm}$. The diode used for the measurements of interest²⁶ has a 3-mil diffusion window. To simulate this diode, calculations were made for a 12- μm N-type diode doped to $3 \times 10^{15} \text{ cm}^{-3}$. The P region was 1 μm . The diode area was set at $5 \times 10^{-5} \text{ cm}^2$.

²⁶D. M. Tasca, J. C. Peden, and J. Miletta, *Non-Destructive Screening for Second Breakdown*, *IEEE Trans. Nucl. Sci.*, NS-19 (December 1972), 57-67.

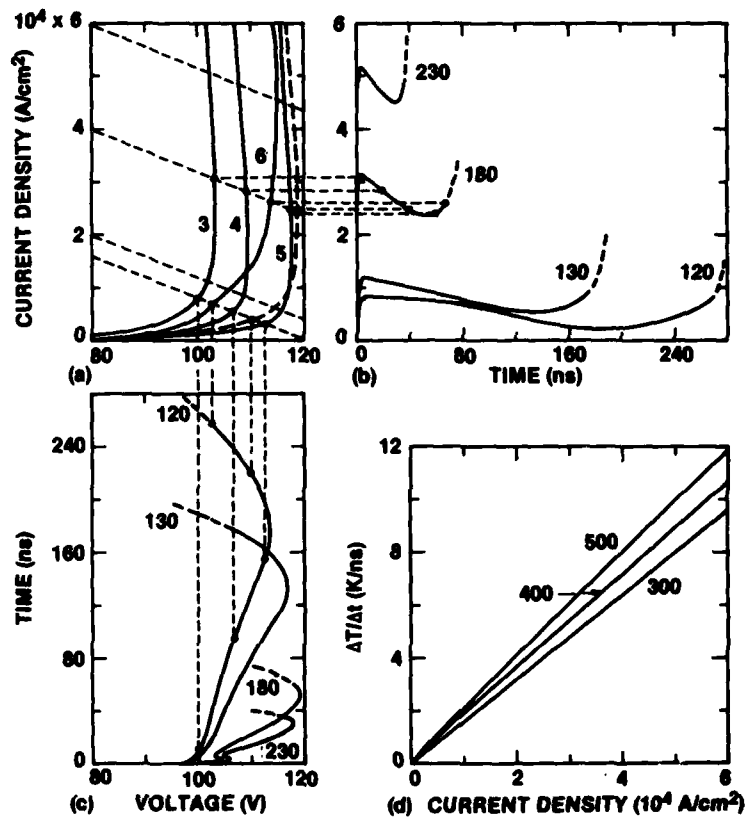


Figure 52. Method of obtaining current and voltage versus time curves from static characteristics. (a) Characteristics for $4\text{-}\mu\text{m}$ P-type diode doped to $5 \times 10^{15} cm^{-3}$. Parameter is temperature in multiples of 100 K. Characteristic for 550 K shown by unlabeled dashed curve. Dashed load lines correspond to 50Ω and diode area of $5 \times 10^{-5} cm^2$. (b) Derived current density versus time curves with applied voltage as parameter. Dashed connections between (a) and (b) help show construction process. (c) Derived voltage versus time curves. Temperature at various times can be obtained from dashed connection to (a). Applied voltage is given for each curve. (d) Rate of temperature rise as function of current density that was used in construction of (b) and (c). Parameter is temperature (K).

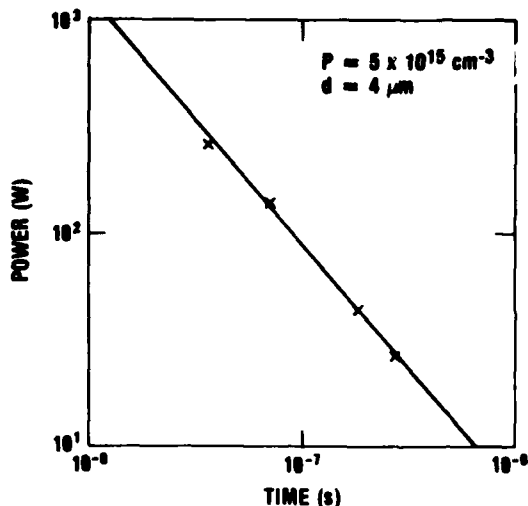


Figure 53. Power to breakdown versus breakdown time for diode of figure 52. Slope of straight line is 1.16.

Constant temperature static characteristics were calculated, point by point, for this diode from 300 to 600 K. These are shown in figure 54. Calculations were also made for thermal injection currents corresponding to 100 K less than the bulk temperature. These curves, for temperatures from 400 to 650 K, are also shown in figure 54. The temperature difference of 100 K was chosen arbitrarily. Different temperature differences for different curves might be more realistic. It may be seen that the curves with the lower temperature boundary condition merge with the corresponding isothermal calculation at a current density that increases with temperature.

Portions of the two-temperature characteristics are replotted in figure 55. A linear scale is used and the ordinate is total current. Load lines for 5000Ω are shown in figure 55(a). This value was chosen for agreement with the experimentally observed²⁶ changes of voltage and current upon second breakdown. The method of calculating current versus time and voltage versus time was described in section 11.1. The results for applied voltages of from 500 to 1200 V are shown in figure 55(b) and (c). The area of $5 \times 10^{-5} \text{ cm}$ should be used to convert J to I in figure 55(d). As seen in figure 55(b), the current is nearly constant in time, whereas the voltage changes considerably with time (and temperature) as seen in figure 55(c).

From the current and voltage at each time step, the average power dissipated may be calculated. The time to reach the temperature of 650 K is assumed to be the breakdown time. The power thus calculated as a function of the time to breakdown was found to agree satisfactorily with experimental measurements for breakdown times of less than $\sim 1 \mu\text{s}$. Power to breakdown obtained from the isothermal calculations fell considerably below the measured curve.

²⁶D. M. Tasca, J. C. Peden, and J. Miletta, *Non-Destructive Screening for Second Breakdown*, *IEEE Trans. Nucl. Sci.*, NS-19 (December 1972), 57-67.

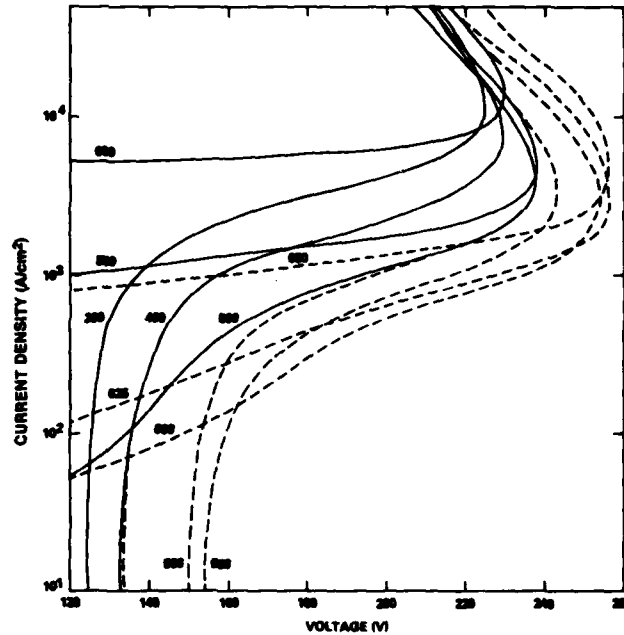


Figure 54. Calculated static characteristic for 12- μm N-type diode doped to $3 \times 10^{15} \text{ cm}^{-3}$, simulating 1N4148. Solid curves are for isothermal calculations, and temperature (K) is given as parameter. For dashed curves, thermal injection current corresponds to $T - 100$, where T is bulk temperature, again given as parameter.

In the above calculations it was assumed that the thermal time constant was infinite, i.e., the temperature continued to increase as if no heat flow occurred. The thermal time constant, τ_{th} , of the 1N4148 is not available, but 500 mW is given as a safe operating level. Exploratory measurements in our laboratory indicate that the diodes fail at about 1 to 2 W.

The construction diagram of the 1N4148 shows two heat duct heat sinks; on the small area P^+ side, the sink is about 50 μm from the junction and on the large area ($\sim 2 \times 10^{-2} \text{ cm}^2$) N^+ side, the sink is about 135 μm from the junction. Although the equations given in section 4 apply only to one directional heat flow, their use can give some idea of the thermal resistance (θ) and thermal time constants (τ_{th}) expected. The dependance of τ_{th} and θ in silicon upon the distance to the heat sink, L , is shown in figure 56. The equilibrium junction temperature is given by

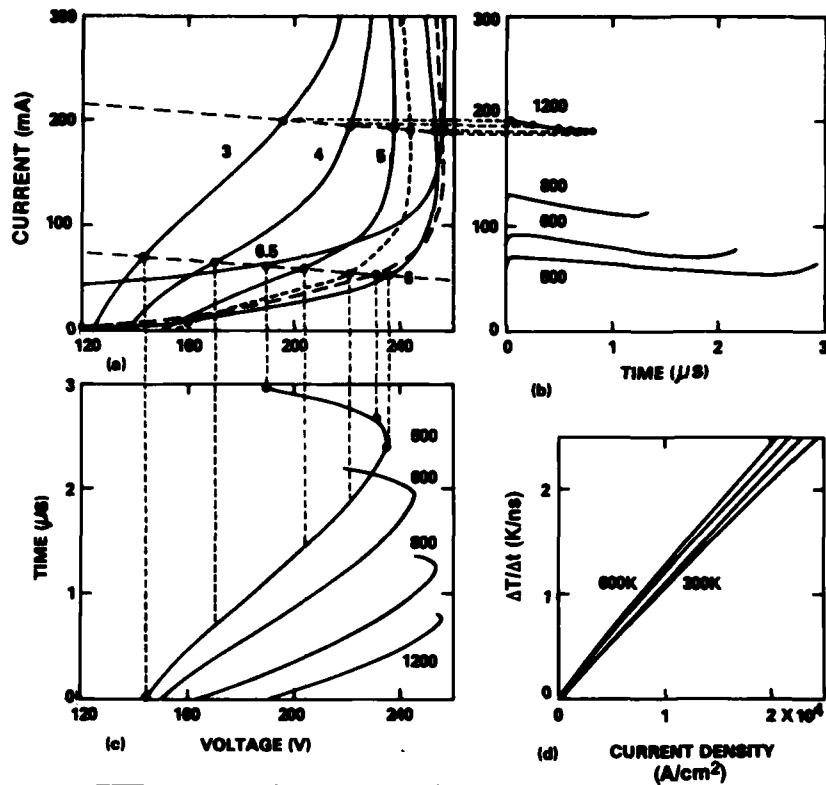


Figure 55. Derivation of current versus time and voltage versus time for 1N4148: (a) Static characteristics of figure 54, replotted on linear scale. Parameter is bulk temperature in multiples of 100 K. Dotted and dashed characteristics are for 550 and 625 K, respectively. Area is $5 \times 10^{-5} \text{ cm}^{-3}$ and load lines shown are 5000Ω . (b) Resultant current versus time curves. See figure 52 caption for details. (c) Resultant voltage versus time curves. (d) Time derivative of temperature as function of current density. Parameter is temperature and unlabeled curves are for 400 and 500 K in monotonic order.

$$T_j = T_o + LP/k_T A \quad , \quad (39)$$

as seen from equations (21) and (23). For a power of 1 W, $L = 135 \mu\text{m}$, and $A = 5 \times 10^{-5} \text{ cm}^2$, $T_j - T_o$ is calculated to be 186 K. This is also equal to θ , since $P = 1 \text{ W}$. The temperature dependence of k_T is neglected. This temperature increase per watt is in reasonable agreement with the laboratory measurement of 1 to 2 W for failure. The thermal time constant would be dominated by the closer heat sink. From equation (22) we find $\tau_{th} = 2.8 \times 10^{-5} \text{ s}$ for $L = 50 \mu\text{m}$.

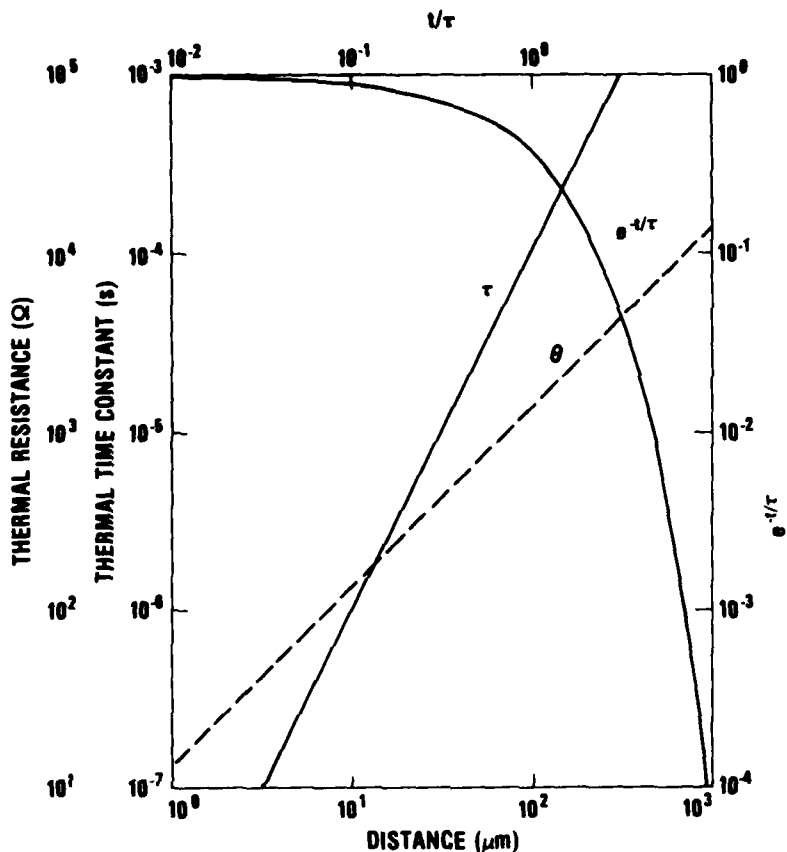


Figure 56. Thermal time constants and thermal resistance of silicon as function of distance (left and bottom scales). See equations (22) and (23). Area assumed is $5 \times 10^{-5} \text{ cm}^2$. Shown also, right and upper scales, is the plot of $\exp(-t/\tau)$ versus t/τ .

For a further check, we can use

$$P\theta/\tau_{th} = JE/\rho c \quad , \quad (40)$$

which is required at $t = 0$ from equations (25) and (26). From computer calculations, $JE/\rho c = 1.5 \times 10^7 \text{ K/s}$ for a power of 1 W. Since $P\theta$ is the steady-state temperature difference (eq (21)), θ is better known than τ_{th} . To agree with the computer value for dT/dt at $t = 0$, one finds from equation (40) that $\tau_{th} = 1.2 \times 10^{-5} \text{ s}$ for $\theta = 186 \text{ K/W}$.

Selecting 1×10^{-5} s for τ_{th} , the computed power to breakdown, P_B , versus time for breakdown, t_B , for the 1N4148 was recalculated using equation (26). The results showed an appreciable increase in P_B for $t_B \gtrsim \tau_{th}/2$. The experimental data²⁶ showed an appreciable deviation from the $P_B \propto T^{-1/2}$ curve at $t_B \cong 1 \times 10^{-6}$ s. Therefore, the calculations were repeated with $\tau_{th} = 2 \times 10^{-6}$ s. The results, shown in figure 57, show good agreement with the experimental data.

Considering the large uncertainty in τ_{th} , the factor of 5 needed for agreement does not seem disturbing. Moreover, it might be expected that τ_{th} would not be constant, but vary with time, especially since the heat sink is dual and the geometry not planar.

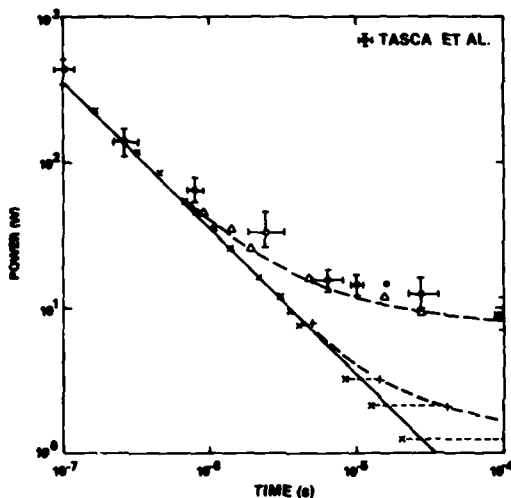


Figure 57. Comparison of calculated and experimental breakdown power for 1N4148 diode. Range of experimental data of Tasca et al (ref 26) is given by error bars. Calculated values are given by crosses for $\tau_{th} = \infty$, by pluses for $\tau_{th} = 1 \times 10^{-5}$ s, and by triangles for $\tau_{th} = 2 \times 10^{-6}$ s. Straight line is drawn with slope of -1 and indicates constant energy.

While the calculated P_B agrees with the measured values for $t_B < 1 \times 10^{-6}$ without adjustment, the calculated breakdown currents, I_B , are lower than those measured by about 40 percent. This is shown in figure 58. There are a number of plausible explanations for this discrepancy. First, the doping level, 3×10^{15} cm^{-3} , chosen for the calculations applies to ideal 1.5 $\Omega\text{-cm}$ silicon; a higher doping level corresponding to lower mobility material would increase the current at a given voltage. Second, the spreading resistance of this diode is less than the calculated space-charge resistance in the SCL current regime. Since the area of the N-type Epi region is 40 times that of the P-diffusion window, current spreading should be expected to occur. Recall that the maximum field at the junction is nearly independent of current density, but the field near the edge of the depletion region increases sharply with current

²⁶D. M. Tasca, J. C. Peden, and J. Miletta, *Non-Destructive Screening for Second Breakdown*, IEEE Trans. Nucl. Sci., NS-19 (December 1972), 57-67.

density, both in the SCL regime. Again, current spreading would increase the current at a given voltage. Third, the calculations of the static characteristics were made with high diffusion coefficients to deliberately damp out IMPATT oscillations which would otherwise appear. The presence of avalanche oscillations results in higher average currents at a given voltage. Avalanche oscillations will be discussed further in section 14. Finally, some of the material parameters chosen may be erroneous. In particular, the use of the ionization coefficients measured by Grant²⁷ reduces the breakdown voltages by about 5 to 10 percent, depending on the diode doping. Again, higher currents would be expected at a given voltage.

12. IONIZING RADIATION

In section 7 it was mentioned that the boundary condition on the current density, J_0 , could be used to simulate the effect of ionizing radiation upon the diode. Only the injected photoionization current has been simulated. Bulk photoionization in the high-field region is not simulated, but since J_0 is multiplied by a multiplication factor of from 10^2 to 10^{10} after breakdown, the bulk photoionization may be neglected.

12.1 Two Examples

The calculated characteristics of section 8 may be used to study the effect of ionizing radiation upon second breakdown. Portions of the characteristics of figure 25 have been redrawn on a linear scale in figure 59. An area of 1×10^{-4} cm² has been assumed and 50- Ω load lines are also shown. Arrows indicate currents for the voltage maxima. For illustrative purposes, let us consider a half-cycle sinusoidal voltage with an amplitude of 160 V and a half-period of 180 ns. With no ionizing radiation it is assumed that $J_0 = 1 \times 10^{-7}$ A/cm², or $I_0 = 1 \times 10^{-11}$ A. From figure 59, no appreciable current flows until the

²⁷W. N. Grant, *Electron and Hole Ionization Rates in Epitaxial Silicon at High Electric Fields*, *Solid-State Electron.*, **16** (1973), 1189-1203.

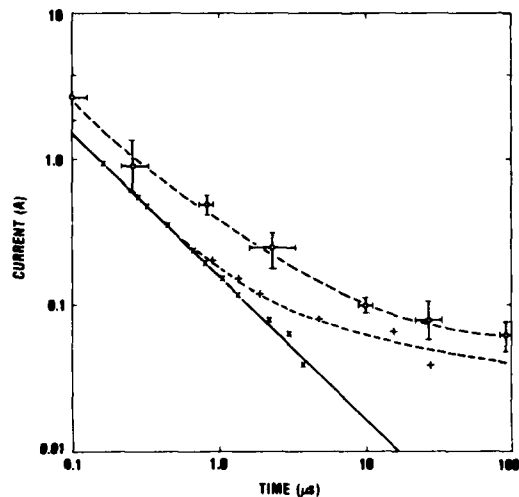


Figure 58. Comparison of calculated and measured breakdown currents for 1N4148 diode. Open circles with error bars give measurements of Tasca et al (ref 26). Crosses indicate values calculated with $\tau_{th} = \infty$ and pluses indicate $\tau_{th} = 2 \times 10^{-6}$ s calculations.

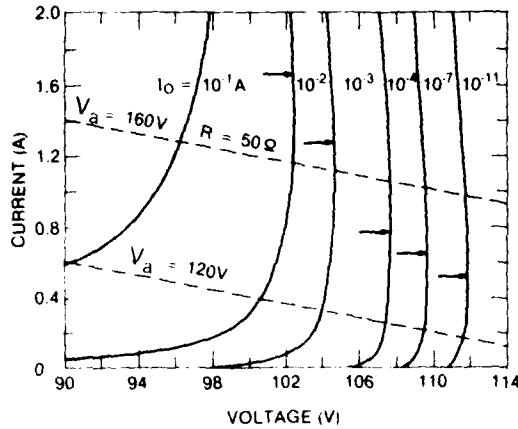


Figure 59. Calculated characteristics of 4- μm N-type diode doped to $5 \times 10^{14} \text{ cm}^{-3}$ with ionizing radiation as parameter. Same characteristics shown in figure 25(b), but plotted on linear scale. Area of $1 \times 10^{-4} \text{ cm}^2$ is assumed. 50- Ω load lines are shown for applied voltages of 120 and 160 V.

applied voltage, V_a , exceeds 110 V. Then the diode current and voltage are determined by the intersection of the static characteristic and the moving load line. This may be done graphically at desired time intervals. The resulting current-versus-time and diode-voltage-versus-time curves are plotted in figure 60(a) together with V_a as applied. Similar curves simulating ionizing radiation, with $I_0 = 1 \times 10^{-2} \text{ A}$, are plotted in figure 60(b). The presence of the ionizing radiation results in an increase in the peak current of about 20 percent and of peak power by 18 percent. At first thought, one might easily conclude that the presence of ionizing radiation increases the susceptibility to damage. However, note that for $I_0 = 1 \times 10^{-11} \text{ A}$, a negative differential resistance (NDR) regime is reached at $I \approx 0.5 \text{ A}$, whereas the NDR regime is only reached at $I \approx 1.7 \text{ A}$ for the $I_0 = 1 \times 10^{-2} \text{ A}$ curve. Thus, for $I_0 = 1 \times 10^{-11} \text{ A}$, the current exceeds the threshold for the NDR regime for a period of 60 ns, whereas for $I = 1 \times 10^{-2} \text{ A}$, the maximum current is well below the NDR threshold. Since current contraction into a channel is likely in the NDR regime, the presence of ionizing radiation may decrease the susceptibility of some diodes to second breakdown.

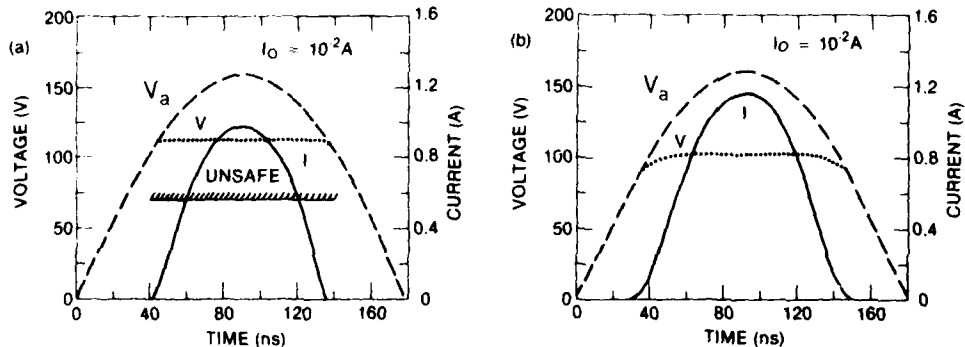


Figure 60. Current and voltage as function of time for half-cycle sinusoidal applied voltage (V_a) pulse shown. Characteristics of figure 59 were used to deduce these curves. (a) $I_0 = 1 \times 10^{-11} \text{ A}$. Negative resistance is encountered in "unsafe" area. (b) $I_0 = 10^{-2} \text{ A}$. Negative resistance area is off scale.

In the above calculation we assumed a constant room temperature characteristic and a moving load line to calculate I and V versus t . In the last section we used a stationary load line and a moving characteristic (as a function of temperature) to calculate dynamic curves. The two techniques may be readily combined to allow both the load line and the static characteristic to move in time in order to simulate a varying applied voltage and a heating of the diode, respectively.

A second illustrative calculation assumes a constant applied voltage of 120 V, but I_0 is varied with time. The pulse of ionizing radiation is assumed to cause I_0 to rise exponentially from 1×10^{-11} to 1×10^{-2} A in 18 ns, to reach a peak of 1×10^{-1} A at 24 ns, decay to 1×10^{-2} A at 60 ns, and thereafter decay by a factor of 10 each 10 ns. The variation of I with time is shown in figure 61. The calculation is again made graphically with the use of figure 59, and the results are also plotted in figure 61. The peak power during the irradiation pulse is greater by a factor of just over 2.5 than the non-irradiated power. In this case, the susceptibility to second breakdown is increased by the presence of the ionizing radiation.

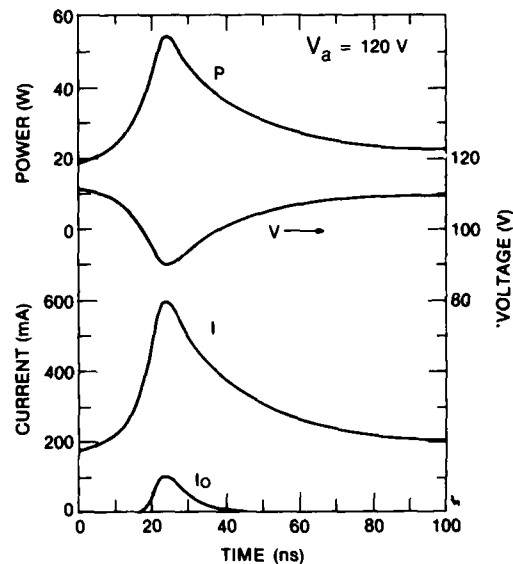


Figure 61. Calculated current, voltage, and power for same diode (fig. 59) with $V_a = 120$ V and exposed to ionizing radiation pulse described in text. Unmultiplied injection current is labeled I_0 .

In the second illustrative calculation in the paragraph just above, we assumed a constant temperature, a stationary load line, and a characteristic moving as a function of I_0 . In order to further include heating during the ionizing pulse, a full set of curves such as figure 57 would be required at each temperature chosen. It would seem that a requirement for information on a particular diode and a particular ionizing pulse would be needed in order to justify such a complex calculation.

12.2 Discussion

There are very limited experimental reports upon the combined effects of an ionizing radiation environment and high electrical stress

on semiconductors. Vault²⁸ found that the effect of ionizing radiation was to reduce the power level for second breakdown, with the reduction greater for reverse bias than for forward bias. However, Habing²⁹ had earlier found that ionizing radiation lowered the pulse current failure threshold of a forward-biased transistor base-emitter junction by a factor of five, but made no change in the reverse-biased threshold. Hartman and Evans³⁰ found that the same level of ionizing radiation had minimal effect upon the burnout thresholds of several transistor base-emitter junctions. There have also been oral reports of ionizing radiation increasing the level of stress required for junction failure.

In order to compare the above calculations with experimental measurements, it is necessary to determine the level of photocurrents that result from given dose rates. The chief unknown in this calculation is the effective volume in which ionization occurs. As argued above, ionization that occurs outside the depletion region is more effective through avalanche multiplication than is the ionization that occurs in the high-field region. However, Habing²⁹ calculates a photoionization current of 100 mA for his device with a dose rate of 5×10^{11} rad(Si)/s. This is just the maximum initiating photocurrent that was assumed in figure 61.

In experimental measurements of power-to-fail, one usually adjusts the power measured to a selected time-to-fail by means of a power law relation between the two. This is necessary since neither power- nor time-to-fail can be preselected. However, this procedure could erroneously eliminate any effect of ionizing radiation upon second-breakdown susceptibility. For example, in the illustrative calculation above of the effect of a pulse of ionizing radiation (fig. 60), an increased power was calculated. However, the time-to-fail would also be decreased. The fact that the data fit the same power-versus-time curve masks the fact that the ionizing radiation did modify the power dissipated. This consideration makes the experimental determination of the effect of ionizing radiation upon stress measurements extremely difficult.

A second indication of possible decreased susceptibility to second breakdown due to ionizing radiation is indicated from calculations made of switching from forward to reverse bias. These calculations, which will be discussed in section 16, have shown that the stored

²⁸W. L. Vault, *Response of Integrated Circuits to a Simulated IEMP Environment*, Harry Diamond Laboratories, HDL-TR-1649 (October 1973).

²⁹D. H. Habing, *Response of Bipolar Transistors to Combined EMP and Ionization Environment*, *IEEE Trans. Nucl. Sci.*, NS-17 (December 1970), 360-363.

³⁰B. F. Hartman and D. C. Evans, *Electrical Pulse Burnout of Transistors in Intense Ionizing Radiation*, *IEEE Trans. Nucl. Sci.*, NS-22 (December 1975), 2528-2532.

charges remaining from the forward conduction prevent the maximum field at the junction from attaining as high a value as was found in calculations for a fully depleted diode. Similarly, the mobile space charge due to ionizing radiation could lower breakdown voltages. In the case of extremely high levels of ionizing radiation, one would expect little difference between forward and reverse bias susceptibility.

As far as is known, this is the first theoretical attempt to quantitatively calculate the combined effect of ionizing radiation and high electrical stress upon reverse-biased silicon diodes. It has been shown that, depending upon the devices and experimental conditions chosen, susceptibility to high electrical stress may be increased or decreased by the presence of ionizing radiation. There is some experimental support of this conclusion.

13. DISCUSSION OF NEGATIVE RESISTANCE

Negative static and dynamic characteristics have been calculated in virtually all diodes simulated. The threshold for the NDR regime varies from around 10^4 A/cm² for near intrinsic material, to a few times 10^5 A/cm² for material doped to 10^{17} cm⁻³. By definition, the static characteristic separates a lower voltage region, where currents decrease in time, from a higher voltage region where currents increase in time. Therefore, dynamic characteristics cross the static characteristic at maximum or minimum points in current, except for the unusual case when the mobile space-charge distribution is drastically different from the steady state. In contrast, dynamic characteristics attain their maximum and minimum voltages when they cross the load line. These rules will be illustrated in the later section on avalanche oscillations.

The stability of a diode for currents on the positive resistance region is much greater than for currents in the NDR regime. Assume that, for reason of material inhomogeneity or temperature nonuniformity, for example, the current density of a local area is greater than that of the surrounding region. If the current is in the positive resistance regime, like point A in figure 62, the local area is undervoltaged, and its current will decrease. This stabilizing effect helps keep the current density uniform despite material defects and temperature gradients. However, if the current is in the NDR regime, like point B in figure 62, the local area is overvoltaged and the current will increase further. Thus, the small area will rob current from surrounding areas and form a channel or filament. One-dimensional calculations are no longer valid when filamentation occurs. However, once filamentation is initiated, damage will occur if the current is not limited sufficiently by the external circuit.

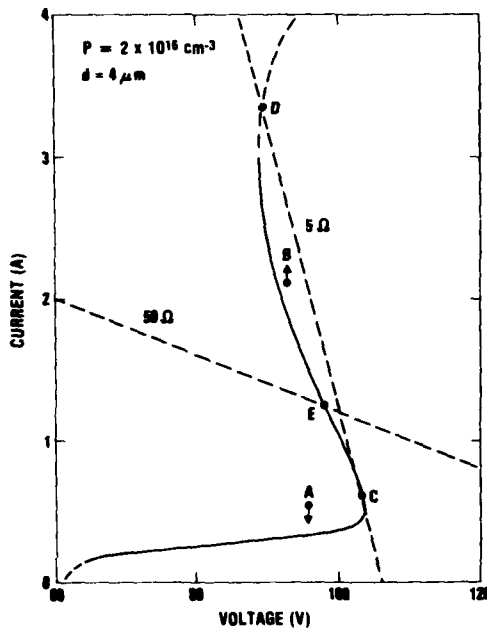


Figure 62. Illustration of diode stability in negative differential resistance region. Characteristic was calculated with $dV/dt = 1 \times 10^{10}$ V/s and is for 4- μm P-type diode doped to $2 \times 10^{16} \text{ cm}^{-3}$. Diode area is $1 \times 10^{-5} \text{ cm}^2$. Two load lines are shown. Dashed-line extension above 3 A is estimated.

high-frequency negative resistance diode in 1958. The IMPact-ionization Avalanche Transit Time, or IMPATT, mode was first observed by Johnston et al³² in 1964. The anomalous, or high-efficiency, mode was first observed by Prager et al³³ in 1967, and was shown to entail a trapped plasma and given the acronym TRAPATT by Johnston et al.³⁴ The relaxing

³¹W. T. Read, *A Proposed High-Frequency Negative Resistance Diode*, *Bell Syst. Tech. J.*, 37 (March 1958), 401-446.

³²R. L. Johnston, B. C. DeLoach, Jr., and B. G. Cohen, *A Silicon Diode Microwave Oscillator*, *Bell Syst. Tech. J.*, 47 (1964), 369-372.

³³H. J. Prager, K. K. N. Chang, and S. Weisbrod, *High-Power, High-Efficiency Silicon Avalanche Diodes at Ultra-High Frequencies*, *Proc. IEEE (Lett.)*, 55 (April 1967), 586-587.

³⁴R. L. Johnston, D. L. Scharfetter, and D. J. Bartelink, *High-Efficiency Oscillations in Germanium Avalanche Diodes Below the Transit-Time Frequency*, *Proc. IEEE (Lett.)*, 56 (September 1968), 1611-1613.

The size of the external resistance is of utmost importance when operating in the negative resistance region. Two load lines are shown in figure 62. If the external resistance is less than the absolute magnitude of the negative resistance, as for $R_s = 5 \Omega$ in this illustration, the current will jump from the point of tangency (point C) to intersect the static characteristic at a much higher current (point D). If the external resistance is greater than the magnitude of the negative resistance and the load line intersects the static characteristic in the negative resistance region (point E for $R_s = 50$), oscillations will result. These will be discussed in the next section.

14. AVALANCHE OSCILLATIONS

14.1 Background

Several times in the preceding sections, avalanche oscillations have been mentioned. While it is not appropriate to discuss these oscillations fully in this report, there are important consequences of these oscillations for second breakdown. Read³¹ originally proposed a

avalanche mode (RAM) was calculated by Ward and Udelson³⁵ in 1968. A variation of the latter mode, named the MULTIPATT mode, was reported by Ward³⁶ in 1973. These modes will be described in the following paragraphs.

14.2 Calculations

In section 11, in discussing the calculations simulating the 1N4148, it was mentioned that avalanche oscillations were present unless prevented by increasing the diffusion coefficients and/or the external $R_S C$ time constant. Examples of these calculated oscillations are shown in figure 63; the series resistance, R_S , was chosen to be 50Ω , and various shunt capacitances, C , of from one to several picofarads were selected. Conventional IMPATT oscillations are calculated with applied

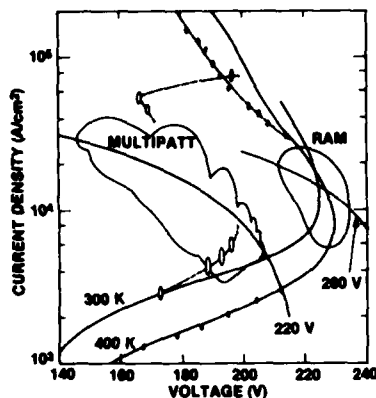


Figure 63. Various avalanche oscillations calculated for simulated 1N4148 diode. Static characteristics are shown for 300 and 400 K. Small ellipses indicate IMPATT oscillations. A MULTIPATT oscillation is shown for 300 K, $V = 220$ V, and $R_S = 50 \Omega$ (load line is shown). A RAM oscillation is shown for 400 K, $V = 260$ V, and $R_S = 50 \Omega$.

voltages below 210 V at 300 K. The lower current limit has not been investigated. These oscillations are shown in figure 63 as the small ellipses joined by a dashed line. In this applied voltage range, IMPATT oscillations appear centered about the intersection of the static characteristic and the load line, but leave the static characteristic as they grow in amplitude and average current. Equilibrium oscillations are attained; these are those which are shown in figure 63. At higher applied voltages, the IMPATT oscillations continue to grow in amplitude; equilibrium is not attained. The current increases, and the voltage decreases in a sequence of loops along and above the load line. When the voltage across the diode can no longer sustain the current, the current decays rapidly, looping below the load line. The voltage recovery is determined by the external $R_S C$ time constant. When the current and voltage return to the load line near the static characteristic, the oscillation is complete.

³⁵A. L. Ward and B. J. Udelson, *Computer Calculations of Avalanche-Induced Relaxation Oscillations in Silicon Diodes*, *IEEE Trans. Electron Devices*, ED-15 (November 1968), 847-851.

³⁶A. L. Ward, *Further Calculations of the Relaxation Avalanche Mode*, *Proc. 4th Cornell Electrical Engineering Conference, Ithaca, NY (1973)*, 391-400.

This mode of oscillation has been named the MULTIPATT mode, since multiple transit time oscillations are superimposed on each RAM oscillation. Near its threshold, the MULTIPATT oscillation is extremely noisy; an example is shown in figure 64. The variation of the oscillation period is mainly due to the residual amplitude of the IMPATT oscillation as it returns to the load line. In calculations where the temperature is increased as power is dissipated, the oscillations may abruptly cease. The similarity to microplasma behavior is obvious.

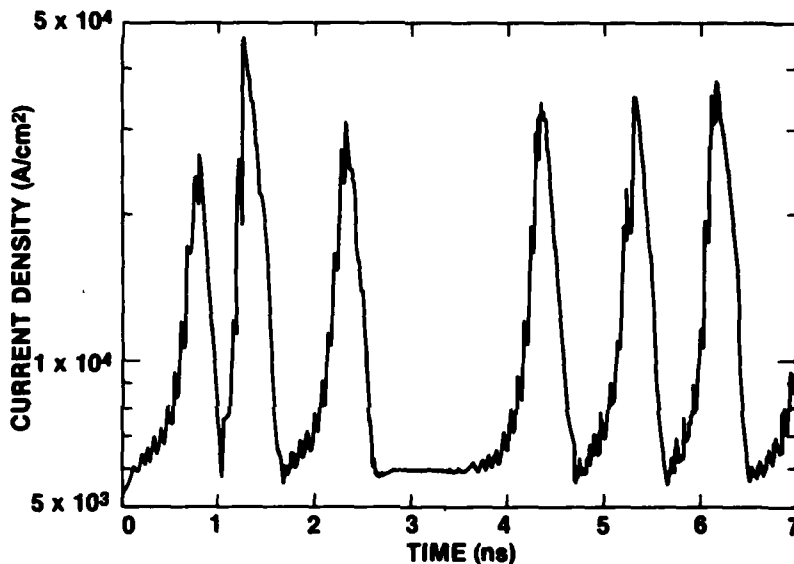


Figure 64. MULTIPATT current oscillations calculated for 300 K, $V = 232$ V, $R_s = 50 \Omega$, and $C = 1 \times 10^{-12}$ F.

At voltages well above the threshold, the MULTIPATT period becomes much more constant. The number of transit time oscillations per MULTIPATT period averages about 20 for this diode and circuit combination. Other combinations have produced from 2 to over 30 smaller current pulses superimposed on the large current pulse. For the ratio of 2 and 3, the corresponding number of bunches of electrons and holes are found to be in transit across the diode at a given time. For higher ratios, the number of bunches present at any time is usually about 3 or 4. An example of the electron distributions at selected times for the simulated 1N4148 is shown in figure 65.

As the applied voltage is increased, the maximum current and voltage excursion increase. In some cases no equilibrium is reached before the computations become unstable and are halted. The highest current peak in equilibrium calculations was 1.5×10^5 A/cm² and the minimum voltage was 94 V. The latter is well below the V_{B1} of 125 V.

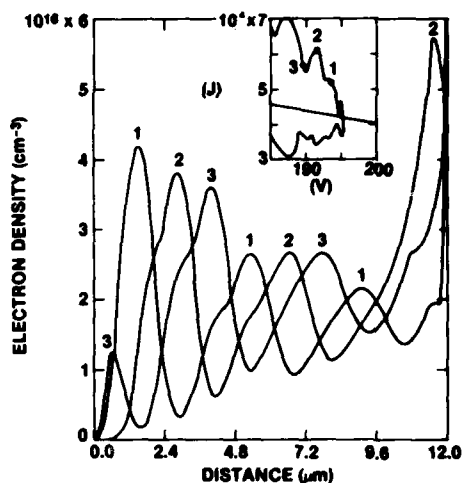


Figure 65. Distribution of electrons across diode during current growth stage. Inset shows portion of characteristic, whose numbered times correspond to distributions shown. Calculations are for 300 K, $V = 300$ V, $R_s = 50 \Omega$, and $C = 3 \times 10^{-12}$ F.

At still higher applied voltages, the MULTIPATT mode oscillations decay into a new mode of small-amplitude transit time oscillations, as shown in figure 63. This mode is termed the traveling-wave IMPATT mode, because multiple bunches of carriers are traversing the diode at any time. At still higher currents, the carrier bunches are confined to two high-field regions near each (P^+N and NN^+) junction. This mode, called the trapped-plasma IMPATT mode, is also shown in figure 63. It requires a much higher voltage than does the traveling-wave IMPATT mode, but less than the nonoscillating state. These modes have been described more fully.²⁵

IMPATT oscillations were also calculated for this diode at 400 K at both low and high currents. No oscillations occurred at intermediate currents. At the higher temperature, the amplitudes of the oscillations are smaller. In the NDR regime, suppressing the oscillations resulted in higher voltages required to obtain the same current, as can be seen in figure 63.

The variation of frequency of the IMPATT mode with current density is shown in figure 66 for several temperatures. The decrease in frequency with temperature is noted experimentally in pulsed IMPATTs. It results from the decrease in saturation velocity with temperature. The straight lines in figure 66 are drawn with a slope of 1/2. There is an approximate fit over two orders of magnitude of J . The half-power

²⁵A. L. Ward, *Modes of Avalanche Oscillations in Silicon Diodes*, *IEEE Trans. Electron Devices*, ED-25 (June 1978), 683-687.

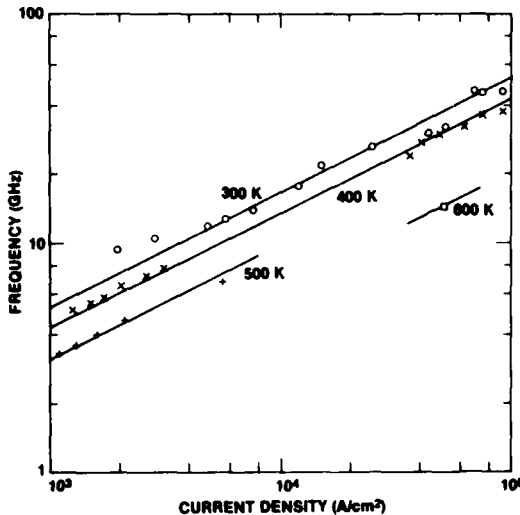


Figure 66. Variation of IMPATT frequency with current density at indicated temperatures. Straight lines are drawn with slope of 1/2.

law has been observed experimentally and attributed¹⁶ to the constancy of the inductance-current (LI) product, since the frequency is given by

$$f \propto (LC)^{-1/2} ,$$

and C is a constant. The constancy of the LI product was verified by calculations for the RAM oscillations.³⁶

In the absence of IMPATT oscillations, steady-state RAM oscillations can only occur in the negative resistance regime. A RAM oscillation is shown for 400 K in figure 63. That these are relaxation oscillations is more evident from plots of I and V as a function of time. These are shown in figure 67 for a near-intrinsic 2.5- μm diode. It is seen that the period is essentially determined by the time required for the diode to reach the breakdown voltage, V_B , from the minimum voltage, V_m .

The time for a capacitance, C, to charge up to V_B from V_m through R_s with an applied voltage, V_a , is

$$T = R_s C \ln \left[\frac{(V_a - V_m)}{(V_a - V_B)} \right] . \quad (41)$$

¹⁶S. M. Sze, *Physics of Semiconductor Devices*, Wiley-Interscience, New York (1969), 39-41, 57-59, 121-126.

³⁶A. L. Ward, *Further Calculations of the Relaxation Avalanche Mode*, Proc. 4th Cornell Electrical Engineering Conference, Ithaca, NY (1973), 391-400.

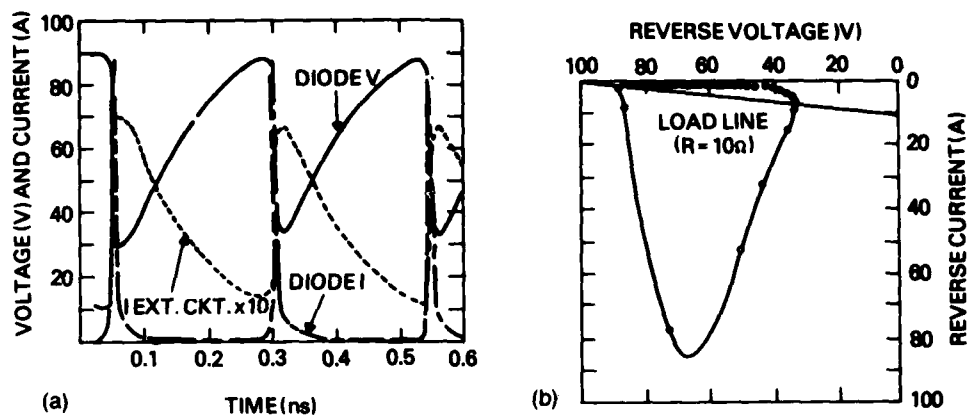


Figure 67. Typical relaxation oscillations. Calculation is for 2.5- μm P-type diode with area of $4 \times 10^{-4} \text{ cm}^2$ and doped to $2 \times 10^{14} \text{ cm}^{-3}$. (a) Temporal variation of voltage across and current through diode. Shown on enlarged scale is current through series resistor. (b) Dynamic current-voltage trace for data shown in (a). Data points are for time intervals of $5 \times 10^{-12} \text{ s}$.

However, V_B and V_m are not constant, but depend on dV/dt , for example, which is a function of $R_S C$. An extensive series of calculations was made to test equation (41). The diode used was a nearly intrinsic 5- μm diode. For large amplitude oscillations, equation (41) was satisfied when R_S and C were varied only when V_B and V_m were adjusted to their calculated values.

By reducing the external $R_S C$ time constant, oscillations were found to decay into nearly sinusoidal oscillations. To analyze these decaying (or growing) sinusoidal oscillations, the diode may be considered to be an inductance, L , representing the avalanche delay, and a differential resistance, R_d , representing the dV/dI of the diode. Then it can be shown³⁷ that current excursions from the steady-state value are given by

$$I(t) = I(0)[\sin(\omega t)] \exp[\lambda t] \quad (42)$$

where

$$\lambda = -\frac{1}{2} \left(\frac{R_d}{L} + \frac{1}{R_S C} \right) \quad (43)$$

³⁷A. L. Ward and L. G. Schneekloth, Calculations of Relaxation Oscillations in Gas Tube Circuits, Harry Diamond Laboratories, HDL-TR-1166 (August 1963).

and

$$\omega^2 = \frac{1}{LC} \left(1 + \frac{R_d}{R_s} \right) - \lambda^2 \quad (44)$$

From equations (42) and (43), it is seen that oscillations will decay ($\lambda < 0$) if R_d is positive, or, for R_d negative, if $R_s C$ is less than $|L/R_d|$, the diode time constant. Oscillations will grow ($\lambda > 0$) if R_d is negative and $R_s C > |L/R_d|$. Equations (43) and (44) may be solved for R_d and L to obtain

$$L = \frac{-R_s C}{1 + 2R_s C \lambda} \quad (45)$$

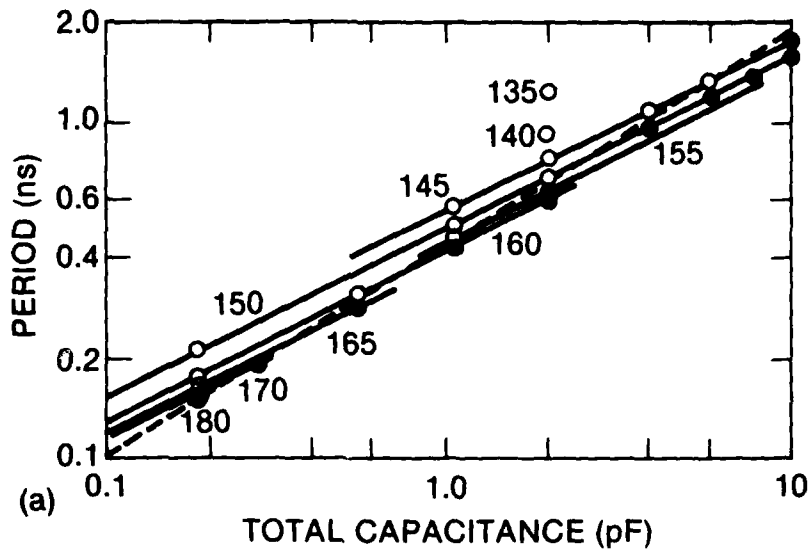
and

$$R_d = \frac{-R_s (1 + 2R_s C \lambda)}{1 + 2R_s C \lambda + R_s^2 C^2 (\omega^2 + \lambda^2)} \quad (46)$$

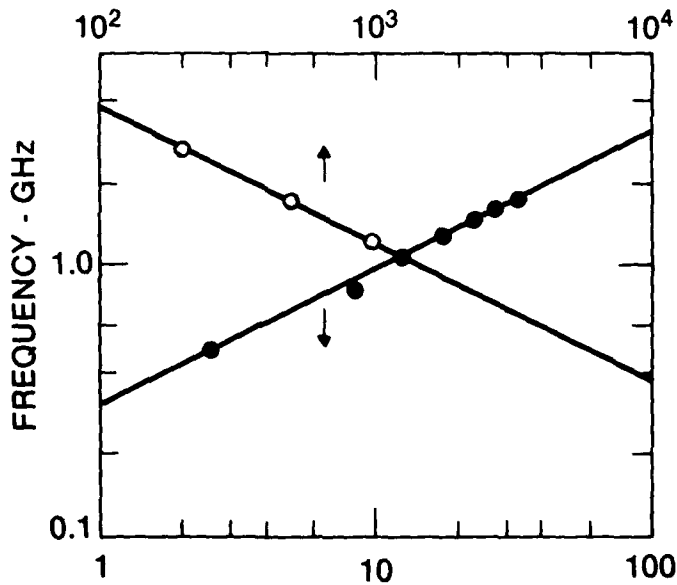
These two equations have been used to analyze the near-sinusoidal oscillations as computed with varying R_s , C , and V_a . The calculated period for the near-intrinsic 5- μm diode is shown in figure 68(a) as a function of the total capacitance, the external C plus the diode self-capacitance. The range of C was from 1×10^{-13} to 1×10^{-11} F, the range of V_a was from 130 to 170 V, and R_s was kept constant at 500 Ω . The straight lines through the data at each value of V_a have a slope of 1/2. The dashed line separating growing oscillations (\bullet points) and decaying oscillations (\circ points) is drawn at a slope of 0.625.

A plot of the average current against V_a showed that the current extrapolated to zero at 127.5 V, the breakdown voltage. Figure 68(b) shows a plot of the calculated frequency, f , against $V_a - 127.5$ for $C = 2 \times 10^{-12}$ F and $R_s = 500 \Omega$. The straight line has a slope of 1/2. Since I is proportional to $V_a - 127.5$ this again shows that $f \propto I^{1/2}$. Also shown in figure 68(b) is a plot of f against R_s for $V_a = 145$ V and $C = 1 \times 10^{-12}$ F. The straight line is drawn with a slope of -1/2. The information in these two figures may be included in the single expression

$$f = 9.5 \times 10^3 (V_a - 127.5)^{1/2} / (R_s C)^{1/2} \quad (47)$$



(a) TOTAL CAPACITANCE (pF)
 -○- SERIES RESISTANCE - OHMS



(b) -●- ($V_a - 127.5$) - VOLTS

Figure 68. Plots of oscillation period and frequency. (a) Oscillation period as function of total capacitance for $R_s = 500 \Omega$. Log scales are used. Open circles denote decaying and solid circles denote growing oscillations. Parameter of each curve is V_a . (b) Oscillation frequency against $V_a - 127.5$ for $R_s = 500 \Omega$ and $C = 2 \times 10^{-12} F$, and against R_s for $V_a = 145 V$ and $C = 1 \times 10^{-12} F$.

Comparison of equations (41) and (47) does not give much promise of compatibility. However, with the end point known, equation (41) can be manipulated to give the form of equation (47). Consider the log term of equation (41):

$$\frac{V_a - V_m}{V_a - V_B} = \frac{V_a - V_B + V_B - V_m}{V_a - V_B} = 1 + \frac{V_B - V_m}{V_a - V_B} \quad (48)$$

Consider the term $V_B - V_m$, the maximum voltage excursion of the oscillation. This should be equal to $\Delta Q/C$, where ΔQ is the charge flow for the voltage difference. This charge flows through R_S , so we may expect ΔQ to be inversely proportional to R_S . Then,

$$V_B - V_m = \text{const}/R_S C \quad (49)$$

Substituting equations (48) and (49) into equation (41), one finds

$$T = R_S C \ln \left[1 + \frac{\text{const}_1}{R_S C (V_a - V_B)} \right] \quad (50)$$

Now we introduce an approximation that

$$\ln(1 + x) \approx 0.8\sqrt{x} \quad (51)$$

Plots of $\ln(1 + x)$ and $0.8\sqrt{x}$ are shown in figure 69. It is seen that the approximation is a good one for $0 < x < \sim 8$. Identifying $1 + x$ with $(V_a - V_m)/(V_a - V_B)$, we find $x > 0$, since $V_B > V_m$, and x of more than 8 would be unlikely. For the illustration in figure 67, $V_a = 100$, $V_B = 90$, and $V_m = 30$. This gives $x = 7$, one of the highest values yet calculated. Applying the approximation of equation (51) to equation (50), we find

$$T = R_S C \sqrt{\frac{\text{const}_2}{R_S C (V_a - V_B)}}$$

or

$$f = \text{const}_3 \frac{(V_a - V_B)^{1/2}}{(R_S C)^{1/2}} \quad (52)$$

which is the expression sought, equation (47). Therefore, we may identify relaxation oscillations in semiconductor diodes by shunting the diode with various capacitances and measuring the frequency variation. IMPATT frequencies are unaffected by the external circuit.

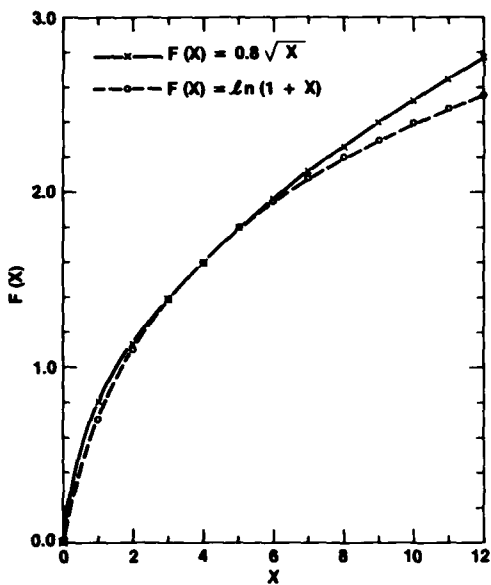


Figure 69. Plots of $\ln(1 + x)$ and of $0.8\sqrt{x}$ as a function of x .

The growing or decaying oscillations for $R_s = 500 \Omega$ and $C = 2 \times 10^{-12} F$ were analyzed by determining the growth rate, λ , and ω as a function of V_a . Then R_d and L were calculated from equations (45) and (46) and are shown in figure 70. Also shown in the same plot is the product of L and the average current, I . This product is seen to be constant, as stated previously. Figure 71 shows plots of the diode time constant, $L/|R_d|$, and λ as a function of V_a . This figure shows that λ is negative (decaying oscillations) for $L/|R_d| > R_s C = 1 \times 10^{-9} s$.

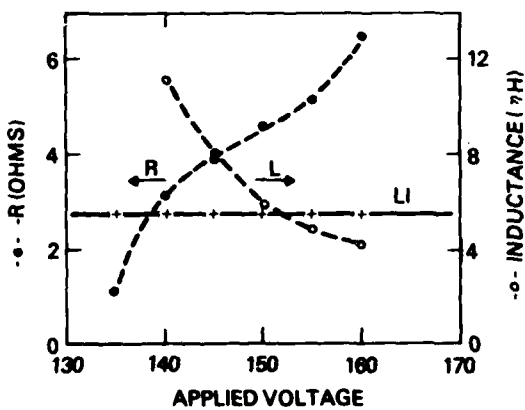


Figure 70. Calculated values of negative resistance, inductance (L), and LI as function of V_a for diode of figure 68. $R_s = 500$ ohms and $C = 2 \times 10^{-12} F$.

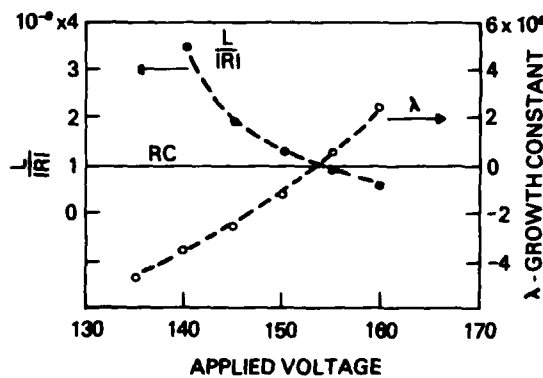


Figure 71. Calculated time constant ($L/|R|$) and growth constant (λ) as function of V_a . Circuit parameters are given in figure 70 caption.

14.3 Experimental Measurements

During the course of EMP vulnerability studies,³⁸ oscillations were observed in the reverse-biased T1DF606A diode (equivalent to 1N645 and so designated hereafter) at stresses just below second breakdown. Oscillations were noted in the vhf/uhf range; figure 72 shows current amplitudes of greater than 1 A and voltage excursions of over 50 V. The onset of the large amplitude oscillations is delayed about 400 ns (in this example) from the time the voltage reaches its nominal maximum. This indicates that these are device oscillations, not merely circuit oscillations. Various capacitors were shunted across the diode to test for relaxation-type oscillations. The dependence of the frequency upon the shunt capacitance is shown in figure 73. The straight line drawn through the data has a slope of $-1/2$, in agreement with equation (52) for the relaxing mode.

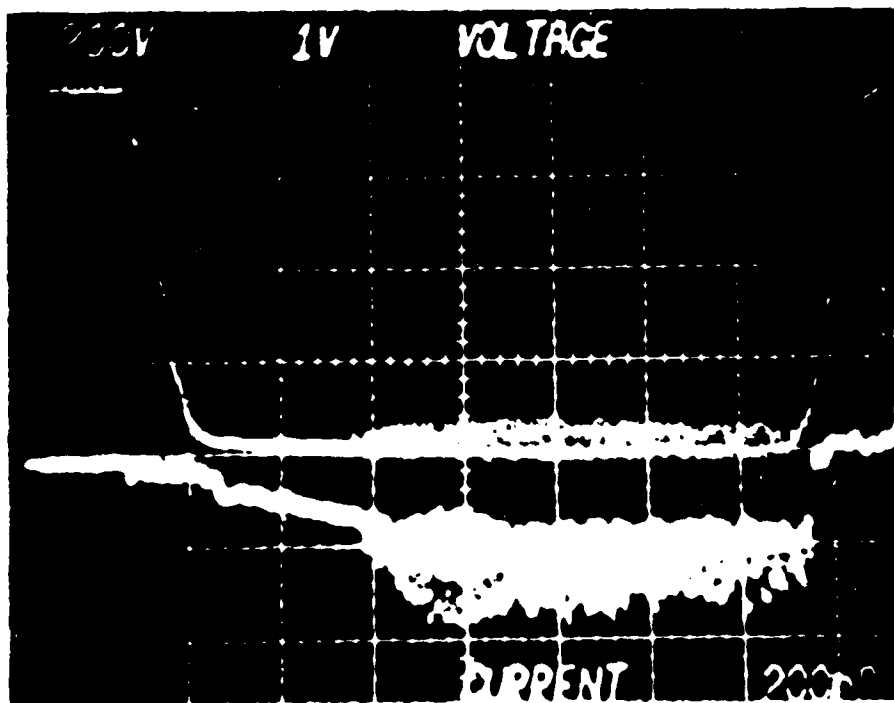


Figure 72. Typical pulsed avalanche oscillation observed in 1N645. Time scale, 200 ns/div. Top trace: voltage, 200 V/div. Bottom trace: current, 1.0 A/div.

³⁸R. V. Garver, R. H. Femenias, Vasco C. Martins, J. L. Washington, Gary L. Roffman, R. J. Reyzer, Samuel A. Clark, Jr., and Morris Campi, Systems Performance Analysis of the Electromagnetic Pulse Effects on Defense Communications System Transmission Systems, Final Report (U), Harry Diamond Laboratories, HDL-TR-1951 (February 1982). (SECRET-RESTRICTED DATA/NOFORN)

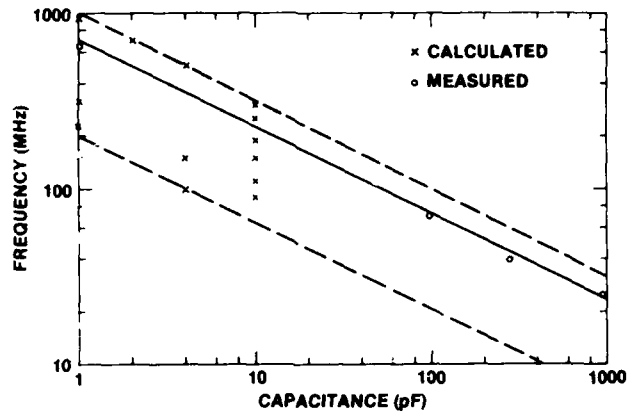


Figure 73. Frequency of oscillations in 1N645 as function of C. Straight lines are drawn with slope of $-1/2$. Multiple calculated frequencies arise from dependence upon amplitude of oscillations.

The doping profile of the 1N645 is not known. The devices were measured in our laboratory to have a V_{B1} of from about 500 to 600 V. Since the oscillations occur at about 800 V we know that the device is not punched through at breakdown. From figure 40 it is seen that a doping level of about $4 \times 10^{14} \text{ cm}^{-3}$ will give $V_{B1} \approx 500 \text{ V}$. Figure 38 shows that a diode width of at least 50 μm would be needed. Calculations were made for an N-type 50- μm diode doped to $4 \times 10^{14} \text{ cm}^{-3}$. The calculations for this diode showed strong IMPATT and MULTIPATT oscillations. The current-density threshold for MULTIPATT oscillations was just under $1 \times 10^3 \text{ A/cm}^2$. Comparing this threshold with the experimental threshold of just under 1 A, as seen in figure 72, we find an area of about $1 \times 10^{-3} \text{ cm}^2$. Capacitance versus reverse voltage measurements of the 1N645 were consistent with the deduced doping and area. As noted in previous sections, oscillations usually may be eliminated in calculations if desired. Static characteristics thus calculated at three temperatures are shown in figure 74. These characteristics are composites of both dynamic and steady-state calculations, chosen for best accuracy in several current ranges. The voltage increases about 10 V per decade increase in current in the SCF current regime, which agrees well with laboratory measurements.

Both IMPATT and relaxation oscillations were calculated for the 1N645. A sequence of oscillations is shown in figure 75, together with the static characteristic and the appropriate 50- Ω load lines. IMPATT oscillations (small ellipses) are noted at both lower and higher currents than the MULTIPATT relaxation oscillations. The calculated current versus time and voltage versus time for an applied voltage, V_a , of 738.4 V are shown in figure 76. The 2.2-GHz IMPATT oscillation is

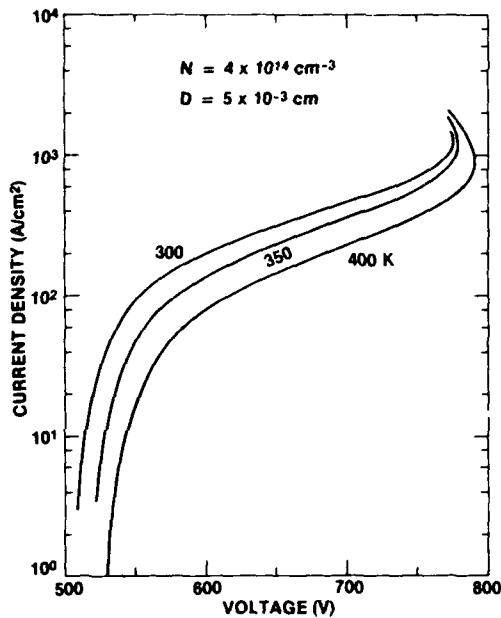


Figure 74. Calculated static characteristics for simulation of 1N645. Parameter is temperature (K).

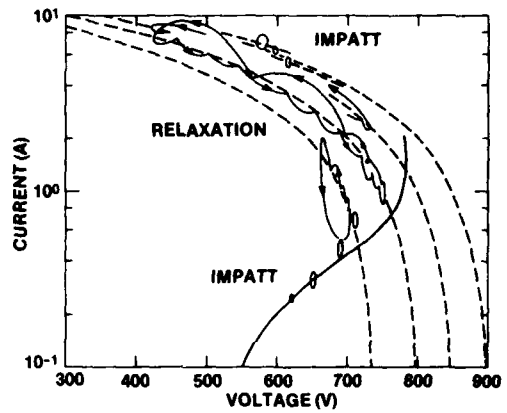


Figure 75. Calculated oscillations for 1N645 simulation. Temperature is 300 K, $A = 1 \times 10^{-3} \text{ cm}^2$, $R_s = 50 \Omega$, $C = 1 \times 10^{-12} \text{ F}$. MULTIPATT types of relaxation oscillations occur at intermediate applied voltages; IMPATT oscillations at both higher and lower voltages.

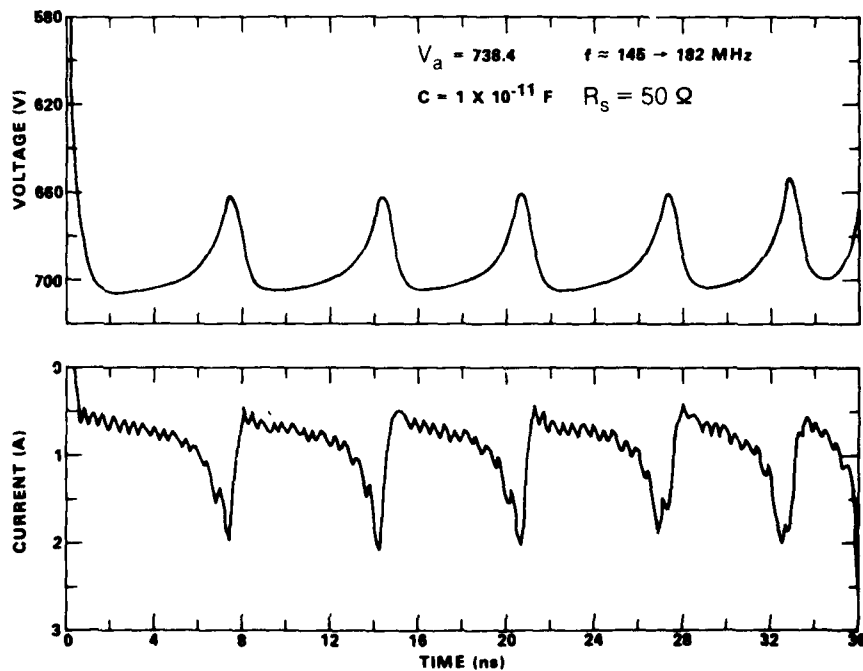


Figure 76. Voltage and current oscillations calculated for 1N645. Change of frequency in time is due to change in amplitude of oscillations.

seen to grow slowly to the current peak. Reducing V_a a few tenths of a volt extends this time appreciably. It is believed that growing IMPATT oscillations occur during the 200-ns delay before large-amplitude oscillations are seen experimentally in figure 72. The frequency of the relaxation oscillations in figure 76 increases from 145 to 182 MHz as time increases. The last current pulse continued to grow until the calculations were halted due to instability.

One major factor in the calculated frequency change of the oscillations is the amplitude of the oscillations. This is complicated by mode changes which are not fully understood. Unexplained mode changes are prevalent among IMPATT diode measurements. The effect of a temperature increase in the diode is also quite noticeable. Figure 77 shows that a rise of only 6 K of the average temperature across the diode reduces the frequency from ~ 317 to ~ 310 MHz. During oscillations, heating is uniform neither in time nor in space. The maximum and average temperatures across a diode are shown in figure 78(a) as a function of time. The temperature distribution across the diode at selected times is shown in figure 78(b). The heating is quite nonuniform.

The dependence of the RAM frequency upon the current level and changes of modes complicates the study of the dependence of frequency upon shunt capacitance. The calculated frequency of the 1N645 as a function of C is given in figure 73. There is about a factor of five range of calculated frequency for each capacitance. Generally, the higher the average current, the higher the resulting frequency, but mode changes produce exceptions. The highest calculated frequencies obey the inverse square root of C quite well, the lowest frequencies less well. It should be mentioned that the experimentally measured oscillations were also subject to mode changes. In particular, there were observably different oscillations of a lower, but irregular, frequency. Those plotted in figure 73 were of a uniform amplitude.

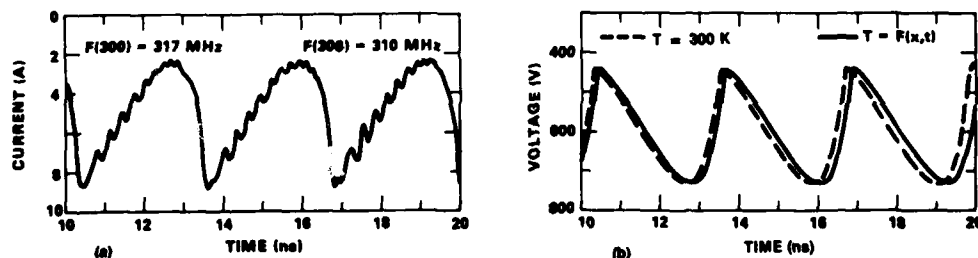


Figure 77. Change of frequency with temperature. (a) Current as function of time. Frequency drops from 317 MHz at 300 K to 310 MHz at average temperature of 306 K. (b) Voltage as function of time. Dashed curve was calculated with constant temperature of 300 K; solid curve was calculated with increasing temperature.

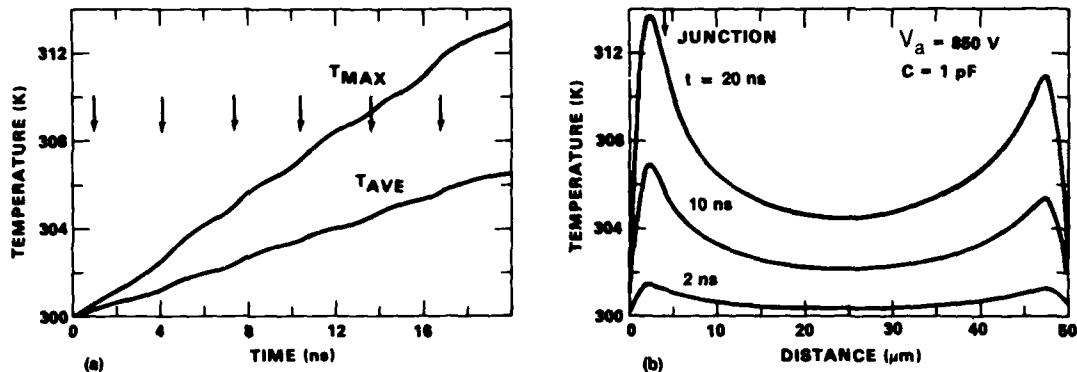


Figure 78. Diode temperature in time and space for run of figure 77. (a) Average and maximum temperature as function of time. Arrows indicate times of current peaks. (b) Distribution of temperature across diode at selected times. Arrow at left top indicates position of metallurgical junction.

Restricting the calculations to a given mode and external circuit, the RAM frequency was found to increase with the square root of the average current density. This is shown in figure 79. However, the frequency of the IMPATT mode of this 50- μm diode increased with only about the 0.4 power of J , as seen in figure 79. Also shown in figure 79 are the IMPATT oscillations of a 12- μm diode and the RAM oscillations of a 5- μm diode, illustrated earlier. Further shown in figure 79 are two points for higher temperature oscillations in the 1N645, the only cases where oscillations have been observed at these or higher temperatures. The modes and circuit are not comparable to the 300 K data.

It is well known that the frequency of IMPATT oscillations is strongly temperature dependent, but the frequency range of 5 GHz and above precludes using this variation as a practical dynamic temperature probe of the junction. Our measurements and calculations show that relaxation oscillations of less than 100 MHz may be used as a temperature probe. Figure 80 shows an example of the decrease in frequency observed in a long (4- μs) pulse. A change of oscillation mode is also evident.

Low-amplitude oscillations were also observed in the 1N4148 during pulse testing in the laboratory.

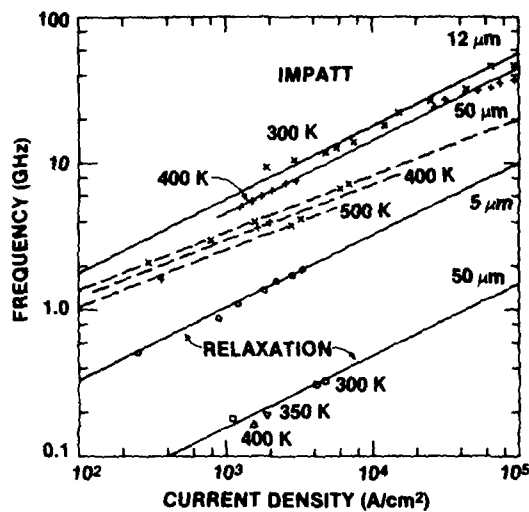


Figure 79. Variation of frequency with current density for several diodes. IMPATT frequencies at 300 and 400 K are shown for 12- μm diode (1N4148) and at 300, 400, and 500 K for 50- μm diode (1N645). Relaxation oscillations are shown for 5- μm and 50- μm diodes. Solid lines are drawn with slope of 1/2.

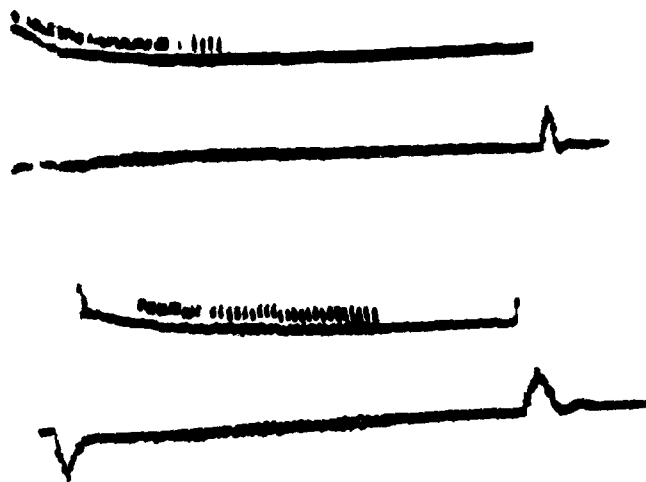


Figure 80. Observed change of frequency of relaxation oscillation with temperature in 1N645. Diode was shunted by 940 pF. Upper trace: 200 V/cm; lower trace: 2 A/cm. Time scale: 0.5 $\mu\text{s}/\text{cm}$.

15. FORWARD BIAS CHARACTERISTICS

15.1 Zero Current

Before discussing calculations of forward bias characteristics, it is useful to discuss the condition of zero current flow, i.e., no applied bias.

For $J = 0$, equation (3) becomes

$$n\mu E = eD(dn/dx) \quad , \quad (53)$$

where the subscripts have been dropped. Solving for E we have

$$E = (d/\mu)(dn/dx)/n = (kT/e)(dn/dx)/n \quad , \quad (54)$$

where the last form follows from the Einstein relation. For room temperature, $kT/e = 0.026$ V. Neglecting p , equation (5) becomes

$$dE/dx = e(N - n)/\kappa\epsilon_0 \quad . \quad (55)$$

The sign convention has been changed back to the conventional.

The last two equations can be solved for the two unknowns, E and n , by a direct difference substitution. That is,

$$\Delta n = (e/kT)nE(\Delta x) \quad , \quad (56)$$

$$\Delta E = e(n - N)\Delta x/\kappa\epsilon_0 \quad . \quad (57)$$

The problem is determining the boundary conditions. First, consider a step junction at $x = 0$. That is, $N = N_0$ for $x < 0$, and $N = 0$ for $x > 0$. We know $E = 0$ at $x = \pm\infty$ and $n = N_0$ at $x = -\infty$ and $n = 0$ at $x = +\infty$, but these conditions cannot be used to solve equations (56) and (57). However, we can start computations from $x = 0$ and proceed in each direction in turn. The problem is that $E(0)$ and $n(0)$ are both unknown. One could guess that $n(0) = N_0/2$, choose Δx , a trial value of $E(0)$, and proceed to use each equation alternately. Even a pocket calculator would quickly convince one that $n(0) < N_0/2$. In fact, it was soon found that $n(0) = N_0/e$. This should have been anticipated, since

$$n(x) = N_0 \exp[-eV(x)/kT] \quad (58)$$

and $V(0) = kT/e$ for a step junction. The value of $E(0)$ and $V(0)$ for various PN junctions may be found in Kennedy,³⁹ where it is shown that $V(0) \approx e/kT$ for $P \gg N$ or $N \gg P$. For $N_0 = 1 \times 10^{19} \text{ cm}^{-3}$ and $\Delta x = 1 \times 10^{-7}$, the value of $E(0)$ was found to be $1.67 \times 10^5 \text{ V/cm}$, again using a pocket calculator. This field maximum agrees with Kennedy's value for $N \gg P$. The field distribution for the $N_0 = 1 \times 10^{19} \text{ cm}^{-3}$ step junction is shown in figure 81. The total high-field space-charge region is about $3 \times 10^{-6} \text{ cm}$ wide. This reverse-bias field everywhere exactly counterbalances the diffusion current that otherwise would flow (eq (53)). The junction potential is known as the built-in, diffusion, or contact voltage. It cannot be measured directly because of other contact potentials to the measuring instrument.

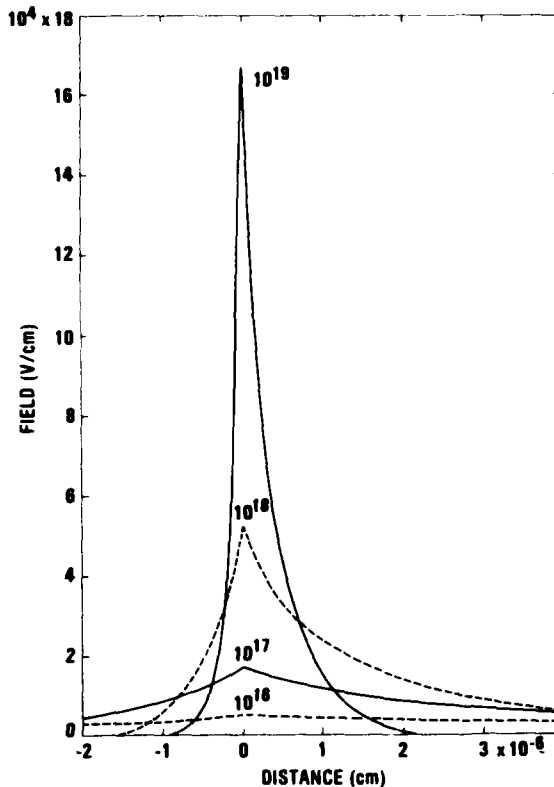


Figure 81. Field distributions for step junctions with zero current flow. Junction is at $x = 0$. Doping on $x < 0$ side is labeled for each curve. Doping is zero for $x > 0$.

Field distributions for other step junctions are shown in figure 81. It may be noted that for $N = N_0/100$, E is reduced by a factor of 10 and x is increased by a factor of 10. This is easily verified by substituting in equations (56) and (57); the equations are unchanged. The variation of $E(0)$ with N_0 for a step junction is shown in figure 82.

A comment should be made on guessing the boundary field, $E(0)$. Consider the $x > 0$ direction where $N_0 = 0$. If E is too high, then Δn is too high by equation (56). This means that n is too low in equation (57); therefore, ΔE is too low. The eventual result is that n becomes negative. Conversely, for E too small, Δn is too low or n too high. It follows that ΔE is too large and E becomes negative. Similar criteria apply to the $x < 0$ direction; N either exceeds N_0 or decreases, or E becomes negative or changes direction. For

³⁹D. P. Kennedy, The Potential and Electric Field at the Metallurgical Boundary of an Abrupt p-n Semiconductor Junction, *IEEE Trans. Electron Devices*, ED-22 (November 1975), 988-994.

programming a computer, equation (58) could be used as a test for the initial boundary condition.

A second type of junction studied is the linear gradient of width d . This is easily programmed, since N_0 changes a constant amount each Δx step. However, the boundary conditions are now more tricky. For very steep gradients the midpoint of the gradient may be used, and values of $n(0)$ and $E(0)$ may be estimated from the step junction. For less steep gradients, the edge of the gradient where $N = N_0$ should be chosen for $x = 0$. Then a guess of $n(0)$ fixes $E(0)$ in the $x < 0$ direction. Calculations converge when $E(d)$ and $n(d)$ agree with a possible solution to the step junction $N = 0$ region.

The field and carrier distribution for a graded junction with $N_0 = 1 \times 10^{19}$ and $d = 2 \times 10^{-6}$ cm is shown in figure 83. The maximum field for the graded junction is only 6.1×10^4 V/cm as compared to 1.67×10^5 V/cm for the step junction.

The two equations were programmed for a desk calculator and the accuracy of $n(0) = N_0/e$ and the fit to equation (58) verified to several more significant figures. Even for these more accurate calculations, E becomes sufficiently small while n is still so much greater than n_i that the neglect of p is justified.

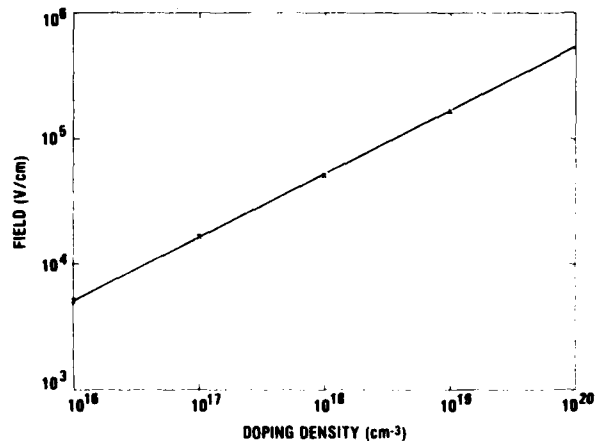


Figure 82. Junction field for step junctions with zero current flow as function of doping level. Equation of straight line is $E = 5.4 \times 10^{-5} N^{1/2}$.

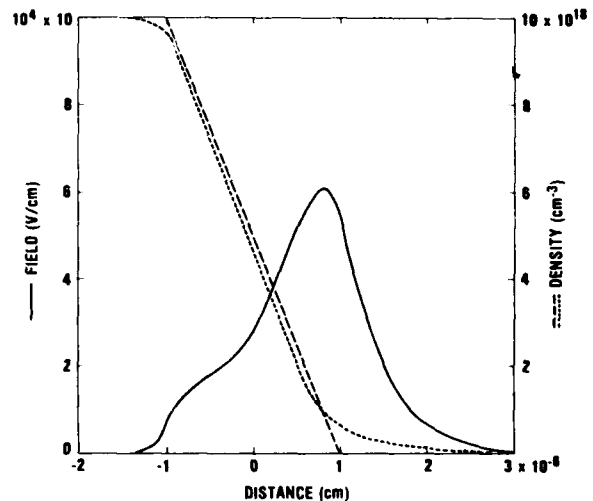


Figure 83. Field distribution for linearly graded junction with zero current flow. Doping is shown as dashed curve; equilibrium carrier density as dotted curve. Field maximum, solid curve, is near zero doping intercept.

This discussion of the field distribution for $J = 0$ has been presented to introduce the fact that, for reasonable currents the field in regions of doping gradients will be negative with zero or small forward bias. The current density needed to assure $E = 0$ when the gradient is dn/dx is given, from equation (3), by

$$J = eD(dn/dx) \quad . \quad (59)$$

Since $D \approx 40$ for electrons, for $\Delta N = 1 \times 10^{16}$ in $1 \mu\text{m}$ (a very small gradient of $1 \times 10^{20} \text{ cm}^{-4}$), $J \approx 640 \text{ A/cm}^2$. Thus, for smaller current densities, the field will remain negative in the junction region, but will be positive where there is a smaller carrier gradient. The presence of fields of both polarities causes problems in the present computer program.

When N_0 is only a few orders of magnitude greater than n_i , it will be necessary to include p in equation (55). Then p can be calculated from the relation

$$p = n_i^2/n \quad ,$$

and p and n will each approach n_i as $E \rightarrow 0$.

For very small applied voltages, equation (56) can be modified to include J , as follows.

$$\Delta n = (e/kT)nE(\Delta x) \pm (J/eD)(\Delta x) \quad , \quad (60)$$

where the positive sign pertains to forward bias and the negative sign to reverse bias. The sign is verified by setting $E = 0$ (valid only for a forward bias) and regaining equation (59).

No exploratory calculations have been made with p or J not equal to zero.

15.2 Static Characteristics

The initial conditions chosen to calculate forward-bias static characteristics are those that are exactly SCF; i.e., the mobile carriers are set equal to the doping density. The applied voltage is an important parameter in the initial transient. For low voltages, carriers cannot flow in unlimited densities from the highly doped region, but are limited by space charge. After the carriers cross the diode, the charges neutralize and the densities continue to grow. The formation of a negative field at one or both high doping gradients eventually causes instability in the present computer program (which was not designed for forward-bias calculations), and the calculations are halted. By reducing the doping levels and/or gradients in the highly

doped regions, the problem is reduced. Further, at high enough currents, the negative field disappears, as discussed in the first part of this section. Therefore, second-breakdown studies are not impeded.

When higher applied voltages are used for forward-bias calculations, initial space-charge limiting is reduced, and the current grows to an equilibrium value quite rapidly. A large series resistance permits a high initial voltage and a sharp voltage drop as the current increases. The current overshoots and approaches equilibrium from above. It has been verified in a few cases that the same equilibrium is reached whether the equilibrium current is approached from above or below. The negative field problem is reduced by the approach from above.

The carrier distribution during the turn-on transient for a 12- μm PIN diode is shown in figure 84. The maximum doping was held to $1 \times 10^{16} \text{ cm}^{-3}$ in the P^+ and N^+ regions. The calculations were made for $V_a = 20 \text{ V}$, $R_s = 100 \Omega$, and an area of $1 \times 10^{-4} \text{ cm}^2$. The corresponding field distributions are shown in figure 85. The voltage and current transients are shown in figure 86. Reasonable equilibrium has been attained.

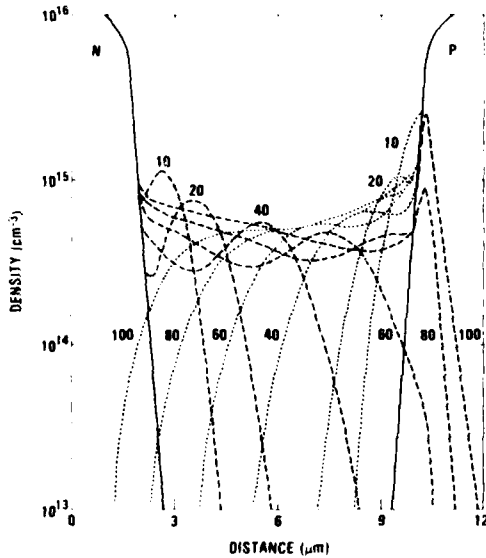


Figure 84. Distribution of carriers during turn-on transient. Doping profile is shown as solid curves, electrons as dashed curves, and holes as dotted curves. Parameter is time in ps.

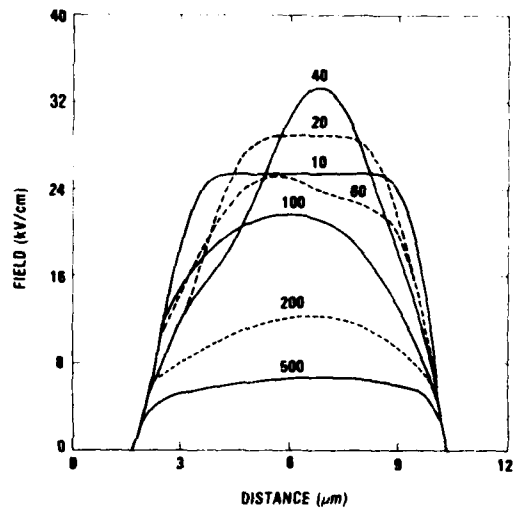


Figure 85. Distribution of field during turn-on transient. Parameter is time in ps.

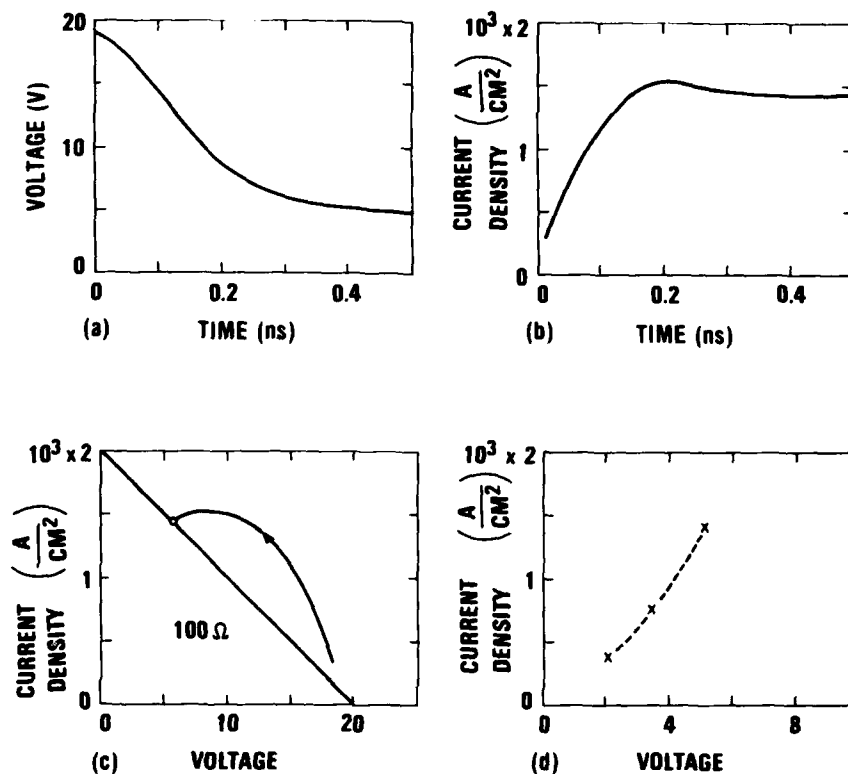


Figure 86. Voltage and current turn-on transients. (a) Diode voltage and (b) diode current density as function of time. (c) Current density as function of voltage; 100- Ω load line is shown. (d) Portion of forward characteristic; $V = 20$ and $R_s = 100, 200,$ and 500Ω .

Whereas doping levels are the dominant factor in reverse breakdown, they are a minor factor in forward-bias characteristics. The two dominant factors are diode width and the recombination lifetime. Calculated forward characteristics for different diode widths are shown in figure 87. The accuracy of these calculations at the lowest currents is questionable, but the strong dependence on diode width is observed experimentally.

A much more extensive study has been made of the dependence of forward characteristics on recombination lifetimes, τ . Static characteristics calculated for a 12- μm PIN diode for various recombination lifetimes are shown in figure 88. For most of the data, the conduction current nearly equals the total current, but at the lowest currents shown, diffusion currents are an appreciable part of the total current.

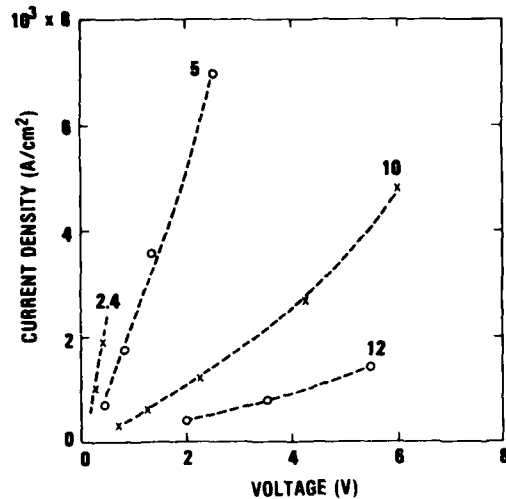


Figure 87. Forward characteristics for several diode widths. Diode width in μm is parameter.

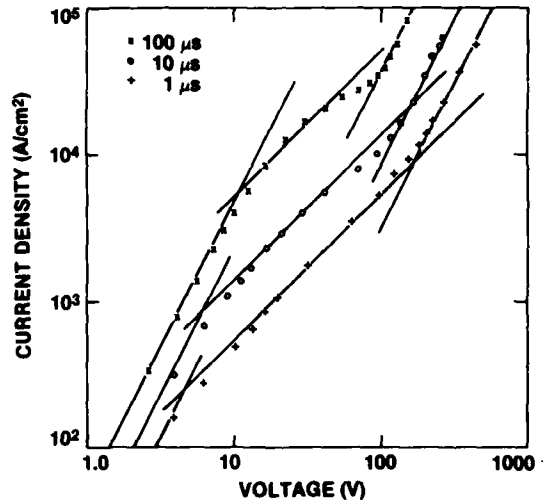


Figure 88. Forward characteristics for 12- μm PIN diode for recombination lifetimes of 1, 10, and 100 μs . Straight lines have slopes of 1 or 2.

For still lower currents, not calculable with the present program, the diffusion component is nearly the total current, and the current increases exponentially with voltage. A recent paper⁴⁰ presents calculations of forward characteristics up to $J \cong 10 \text{ A/cm}^2$ and $V \cong 1 \text{ V}$, showing the deviation from exponential growth at the highest currents.

It is noted in figure 88 that the current increases as the square of the voltage for over an order of magnitude (in the low current regime) for $\tau = 100 \mu\text{s}$, and over smaller ranges for shorter lifetimes. At higher currents, there is a range of ohmic conductivity, i.e., $I \propto V$. For the higher values of τ , there follows a region of sublinear current increase with voltage. At a diode voltage of about 100 V, the field attains the avalanche threshold, and the current again increases with the square of the voltage. There is no sign of a negative resistance regime, even though the current is more than a factor of 10 larger than the threshold of the NDR regime with reverse biasing.

The field and carrier distributions across the diode vary markedly as the current increases and are quite different for different lifetimes. The carrier densities drop monotonically across the intrinsic region at all currents for $\tau = 1 \mu\text{s}$, as shown in figure

⁴⁰P. C. H. Chan and C. T. Sah, *Experimental and Theoretical I-V Characteristics of Zinc-Doped Silicon p-n Junctions Using Exact DC Circuit Model*, *IEEE Trans. Electron Devices*, ED-26 (June 1979), 937-941.

89(a). Recombination prevents nearly all carriers from completely traversing the intrinsic region. The resulting space charge causes large fields to develop, as shown in figure 89(b). For $\tau = 10 \mu\text{s}$, many more carriers completely traverse the intrinsic region and accumulate in the opposite high doping region where they recombine; this is shown in figure 90(a). The net space charge is now smaller, resulting in smaller fields for the same current, as shown in figure 90(b). For $\tau = 100 \mu\text{s}$, the total number of minority carriers in the highly doped region is greater than those in the much wider intrinsic region. Figure 91(a) shows that the carrier densities of the electrons and holes are nearly equal across the intrinsic region. Again, the field is greatly reduced at the same current density, as seen in figure 91(b).

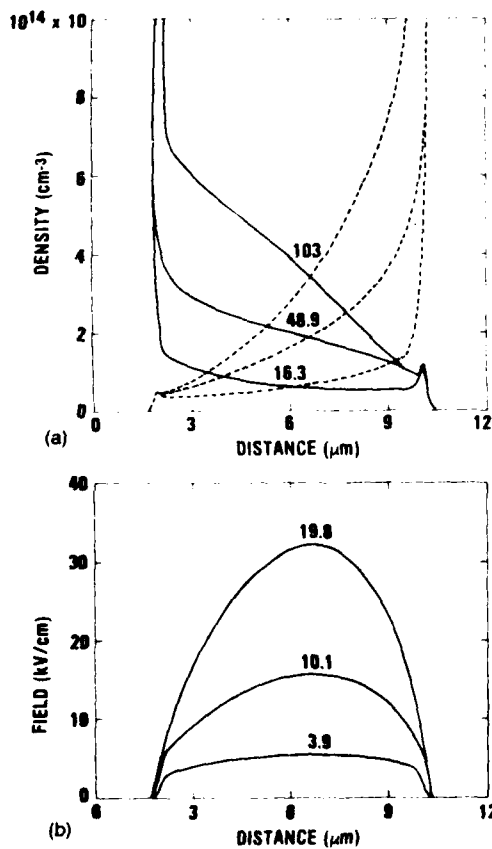


Figure 89. Field and carrier distributions for $\tau = 1 \mu\text{s}$. (a) Solid curves--electrons; dashed curves--holes; parameter--current (mA). Area is $1 \times 10^{-4} \text{ cm}^2$. (b) Field distributions: parameter--diode voltage.

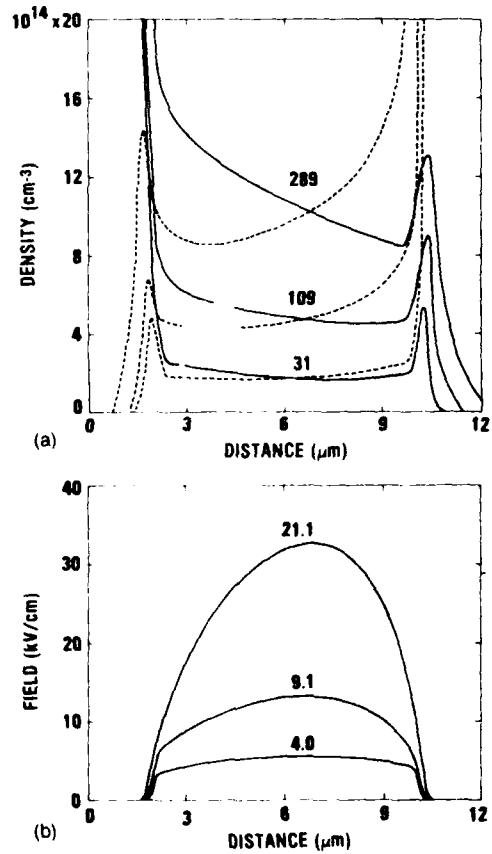


Figure 90. Field and carrier distributions for $\tau = 10 \mu\text{s}$. (a) Solid curves--electrons; dashed curves--holes; parameter--current (mA). Area is $1 \times 10^{-4} \text{ cm}^2$. (b) Field distributions: parameter--diode voltage.

In published theoretical studies of PIN diode switching, it has been generally assumed that $p = n$ in the intrinsic region and that there are no accumulated minority charges in the junction region. These calculations indicate that minority charges accumulate in the junction region in any condition where n and p could be considered equal.

The maximum field in the forward-biased diode increases with current as seen in figures 89 to 91. Plots of the maximum field as a function of J for each τ are shown in figure 92. A power law region is evident for each τ ; the slope varies from about 0.63 for $\tau = 100 \mu\text{s}$ to 1.0 for $\tau = 1 \mu\text{s}$. The falloff of E_{MAX} at high J is due to avalanching. Note that there is a higher threshold for avalanching for a smaller τ . An example of calculated fields with and without avalanching is shown in figure 93(a). The corresponding carrier densities are shown in figure 93(b). When $E = E_{\text{MAX}}$, $p = n$ in the intrinsic region. The value of $n_{\text{eq}} = p = n$ is shown in figure 94 as a function of J . Again, power laws are noted at small currents. The slopes vary from 0.77 to 0.92. At higher currents, the curves merge into a single curve with a slope of 1.07.

It is also of interest to know how the maximum field varies with n_{eq} . This is shown in figure 95. The slopes of the straight lines as drawn vary from 0.84 to 1.21. There is some supporting evidence that for $\tau = 100 \mu\text{s}$, the sharp dropoff of E_{MAX} at the lowest n_{eq} densities is real. Calculations can be made to higher τ values for smaller diode widths. Figure 96 shows a plot of E_{MAX} as a function of n_{eq} for a 4- μm diode, with τ varying from 2.5×10^{-5} to 2.5×10^{-3} s. The highest value of τ is that given by Sze¹⁶ for the best silicon. Also shown are a few calculations for a 3- μm diode; there is a strong indication that

¹⁶S. M. Sze, *Physics of Semiconductor Devices*, Wiley-Interscience, New York (1969), 39-41, 57-59, 121-126.

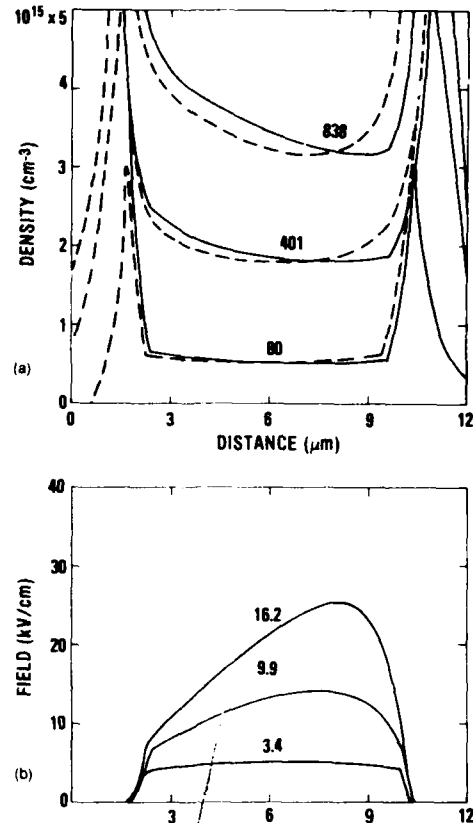


Figure 91. Field and carrier distributions for $\tau = 100 \mu\text{s}$. (a) Solid curves--electrons; dashed curves--holes; parameter--current (μA). Area is $1 \times 10^{-4} \text{ cm}^2$. (b) Field distributions: parameter--diode voltage.

E_{MAX} drops sharply at the lowest currents calculable, i.e., when diffusion currents begin to dominate. This is to be expected, since diffusion is independent of field. In all cases, in both figures 95 and 96, the dropoff of E_{MAX} occurs at approximately $E = 5 \times 10^3$ V/cm. It may or may not be significant that this is about the field where the electron velocity begins to saturate; see figure 1.

All the data thus far have been for diodes at room temperature. Temperature effects are due to the variation of mobility and of the intrinsic density, n_i , with temperature. The latter effect is evidenced in the recombination rate; see equation (10). A plot of J versus V for a 12- μ m PIN diode is shown in figure 97 for temperatures up to 400 K, $\tau = 1 \mu$ s. Comparing figure 88 with figure 97, we see that the 400 K, $\tau = 1$ s, curve follows very closely with the 300 K, $\tau = 100 \mu$ s, curve. The decreased V required to obtain a given J at higher temperatures is due to the reduced recombination. Calculations were also made for 450 K, but the points showed considerable scatter. Generally, the 450 K curve followed the 400 K curve, showing that the changes due to mobility and lifetime temperature dependencies tended to counterbalance one another. For long

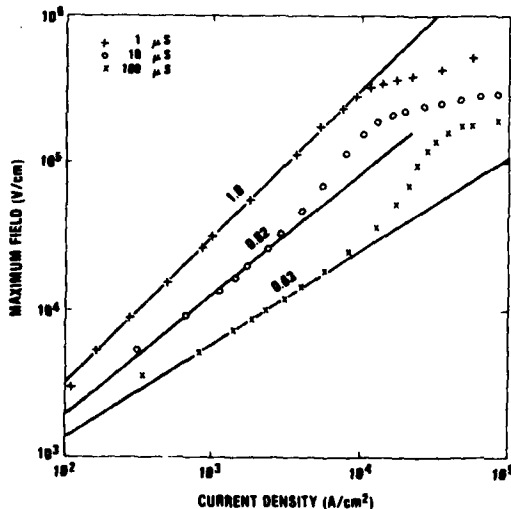
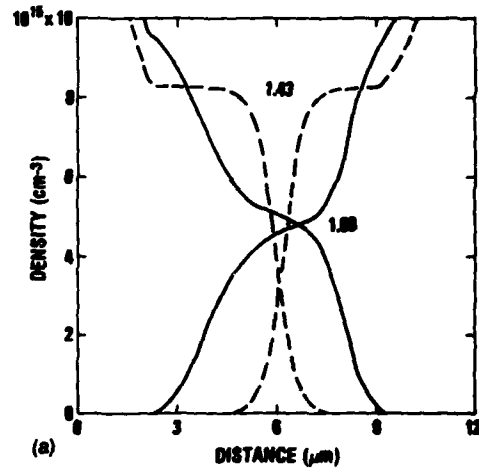
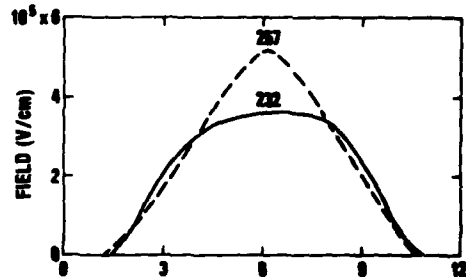


Figure 92. Maximum field as function of current density for three recombination lifetimes. Slopes of straight lines are given.



(a)



(b)

Figure 93. Comparison of field and carrier distributions calculated with and without avalanche multiplication. (a) Electron and hole distributions with avalanche multiplication are shown as solid curves and as dashed curves without avalanche multiplication. Parameter gives current in A. (b) Solid curve gives field with avalanche multiplication and dashed curve without. Parameter is diode voltage.

lifetime material, the temperature effect on recombination is small, so an increase in V would be required to obtain a given J , due to the decrease in mobility with temperature. The variation of resistivity with temperature, shown in figure 3, is thus correlated in the forward-biased diode.

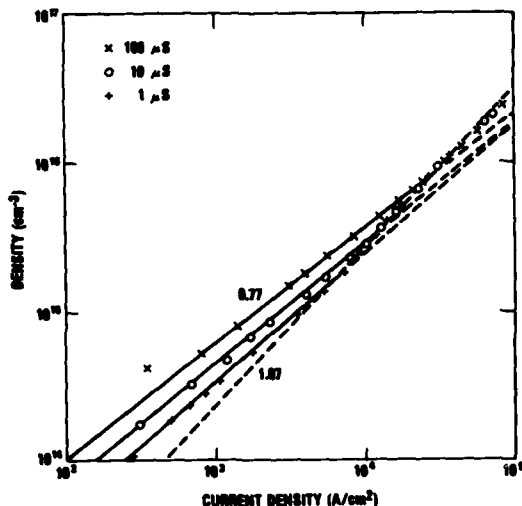


Figure 94. Carrier density at position where electron and hole densities are equal, as function of current density for three recombination lifetimes. Parameters are slopes of straight lines.

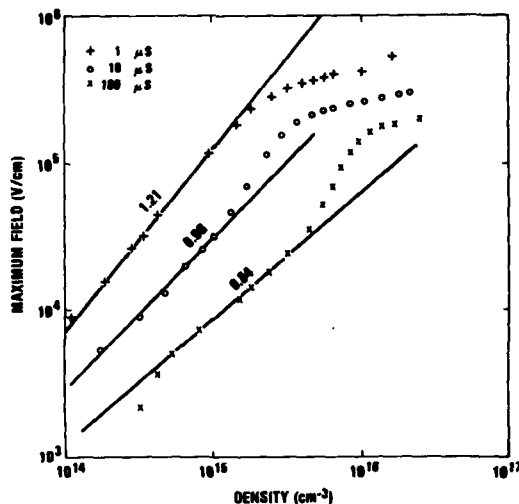


Figure 95. Maximum field as function of equal carrier density at that position. Diode width is $12 \mu\text{m}$ and three recombination lifetimes are used in calculations. Slope of each straight line is indicated.

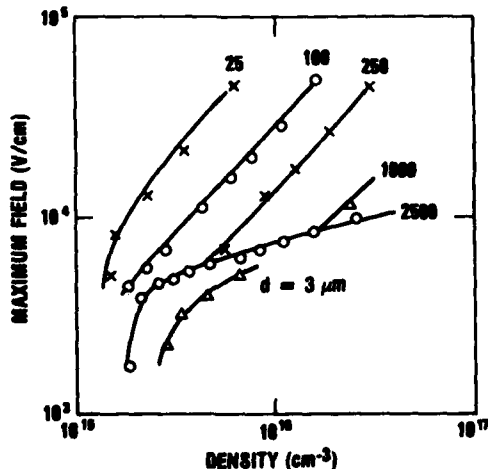


Figure 96. Maximum field as function of equal carrier density for 3- and 4- μm diodes. Curve labeled 3 μs is for recombination lifetime of 2.5 ms. All other curves are for 4- μm diode and recombination lifetime is given in μs .

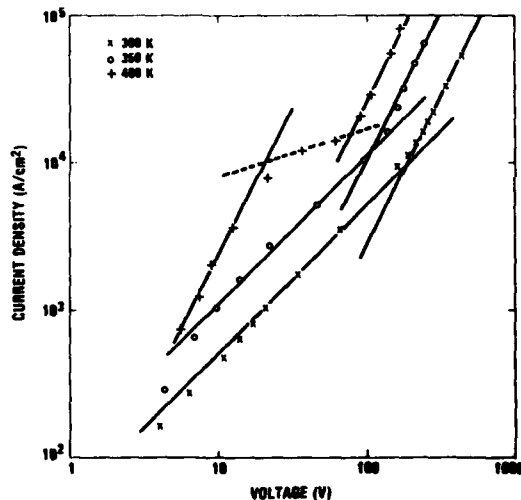


Figure 97. Forward characteristics for 12- μm diode at different temperatures. Recombination lifetime is $1 \mu\text{s}$.

16. REVERSE SWITCHING TRANSIENTS

16.1 Low-Voltage Switching

The steady-state distributions of electrons and holes across the forward-biased diode are used as initial conditions for simulation of reverse switching transients. For applied reverse voltages less than V_{B1} , the current will decay monotonically with time to the reverse saturation current. For the PIN diode, the turn-off occurs in two stages and is known as a step recovery. During the charge storage time, the reverse current is essentially constant, controlled by the series resistance and the applied voltage. When the carriers begin to deplete the diode, the current decays, and the field concurrently builds up across the depletion region.

An example of the calculated decay of current in a 12- μm PIN diode is shown in figure 98. The calculations are for a temperature of 400 K. Two applied voltages are used, as well as two initial values of n_{eq} (i.e., $n = p$ in the intrinsic region). The recombination lifetime (τ) is 2.5 ms and the series resistance is 100 Ω . The distribution of charges across the diode is shown at selected times in figure 99. Comparing figures 98 and 99 we see that the initial constant current period corresponds to the recovery of the charges stored in the highly doped regions. Published theories of the step-recovery diode do not include these stored charges, but identify the end of the constant current period with the drop to zero of the charges at the infinitely narrow NI junction. Since they assume that all the stored charge is in the intrinsic region, they deduce a charge level in the I region several times too high. The field deduced thereupon is similarly too low. Invariably, much more charge is in the constant current period than in the current decay period. Many calculations, not presented here, verify that there is a one-to-one relation between the initial charge in the high doping region and the charge flowing in the constant current stage. Calculations made with differing reverse voltages (see fig. 98) and different resistances (not illustrated) verify that the amount of charge recovered is essentially constant, independent of the current level. The amount of charge recovered during the current decay is found to agree with the total initial charge in the intrinsic region. This is also illustrated in figure 98. If τ is decreased to 2.5×10^{-4} from 2.5×10^{-3} s, some measurable charge is lost by recombination, and less is collected than was stored. However, identifying the measured reverse recovery time of a diode with τ is a too prevalent erroneous practice.

The field distributions corresponding to the carrier densities shown in figure 99 are presented in figure 100. The second sharp decay in current observed in figure 98 is identified in figures 99 and 100 as the transition from SCL to SCF current flow. This transition has not been calculated previously. For a 3- μm PIN diode, the current

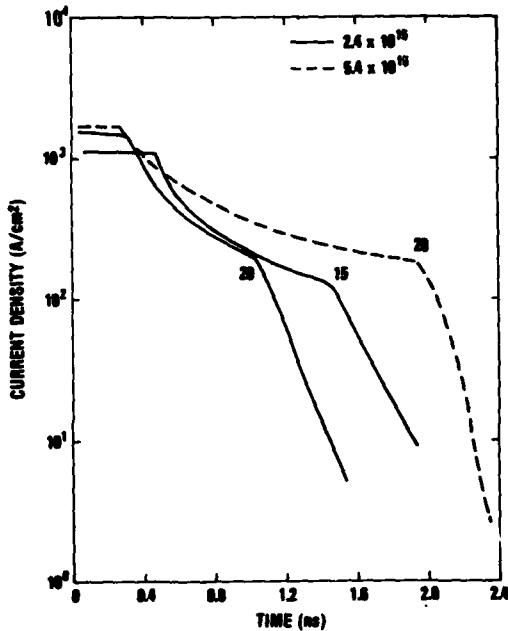


Figure 98. Current decay during reverse switching of 12- μm PIN diode. Solid curves are for initial equal density in the intrinsic region of $2.4 \times 10^{15} \text{ cm}^{-2}$, whereas dashed curve is for initial density of $5.4 \times 10^{15} \text{ cm}^{-2}$. Parameter for each curve is applied voltage.

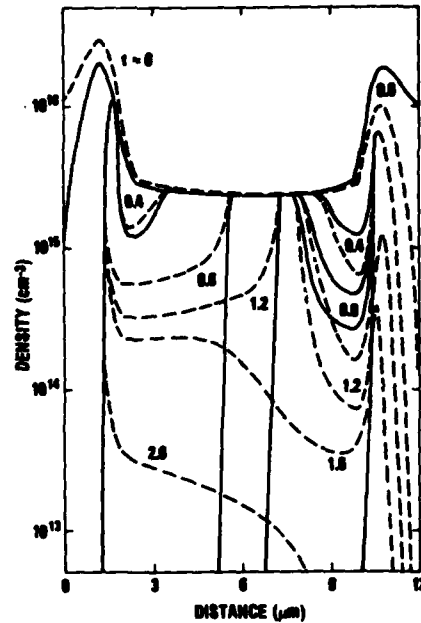


Figure 99. Charge distributions during reverse recovery of diode of figure 98 with 15 V applied. Solid curves are for electrons and dashed curves are for holes. Parameter is time in ns. Distributions of majority carriers in high doping regions are shown only for $t = 0$.

level at which the transition from SCL to SCF conditions occurred was calculated to be just one-half of the constant current level. Experimental measurements by others in our laboratory for such a diode showed such a current break at that level.

16.2 Switching into Avalanche

When the reverse voltage applied for switching approaches V_{B1} , the field becomes sufficient to cause ionization, and the current decay rate is reduced during its later stages. Figure 100 shows that the maximum fields occur at about one-half of the time that it takes for the current to decay to its SCF value. Figure 101 shows the current decay for V_a below V_{B1} and the decay followed by growth for V_a above V_{B1} . These calculations are for the 12- μm PIN diode and $R_s = 50 \Omega$. The shunt capacitance, C , is either 1 or $2 \times 10^{-12} \text{ F}$. The effect of the $R_s C$ time constant is dramatic, since it determines how fast the voltage can

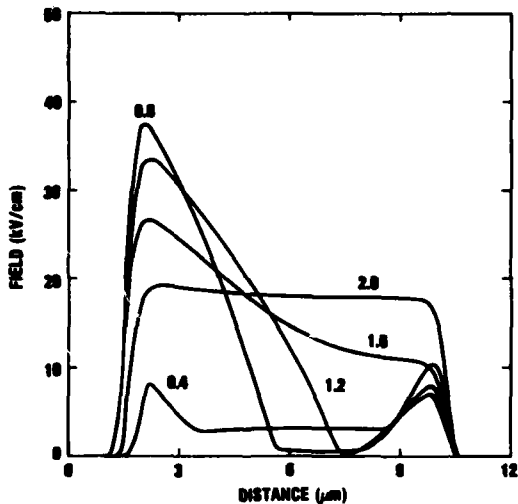


Figure 100. Field distributions during reverse recovery, corresponding to data of figure 99. Parameter is time in ns.

build up across the diode. If the voltage increases faster, the current does not drop as low before the avalanche threshold is reached. The threshold applied voltage to prevent current decay is about 232 V; above that voltage an equilibrium current is attained. Calculations made with depletion (rather than charge storage) initial conditions have shown either no current growth or current increasing indefinitely until calculation instability halted the program; no equilibrium could be attained. There is considerable experimental support for the stabilizing effect of the role of an "approach" current (of various kinds) to the breakdown transition.

For the highest applied voltages shown in figure 101, the current overshoots its equilibrium value. At still higher voltages, the oscillation does not decay, but builds up into a MULTIPATT oscillation. The initial buildup of a MULTIPATT oscillation is shown in figure 102, where J is plotted against V for various applied voltages. The initial stored charge for the calculations shown in figure 102 was less than that used in those shown in figure 101, but the final steady-state currents (when attained) are the same.

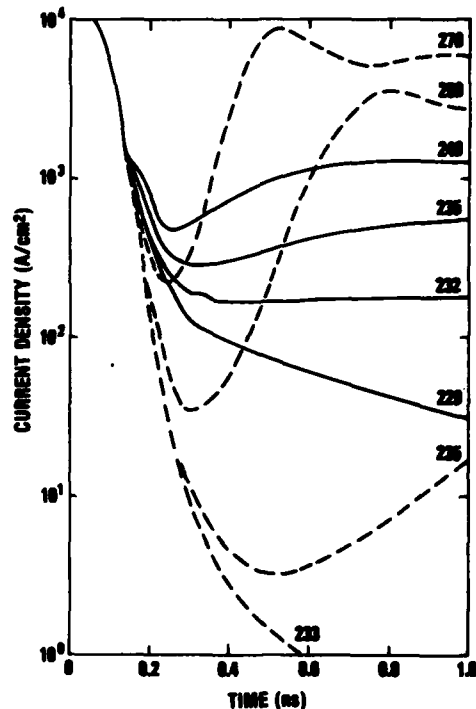


Figure 101. Current densities during reverse switching into avalanche for 12- μ m PIN diode. Load resistance is 50 Ω and parameter is applied voltage. Shunt capacitance is 1×10^{-12} F for solid curves and 2×10^{-12} F for dashed curves.

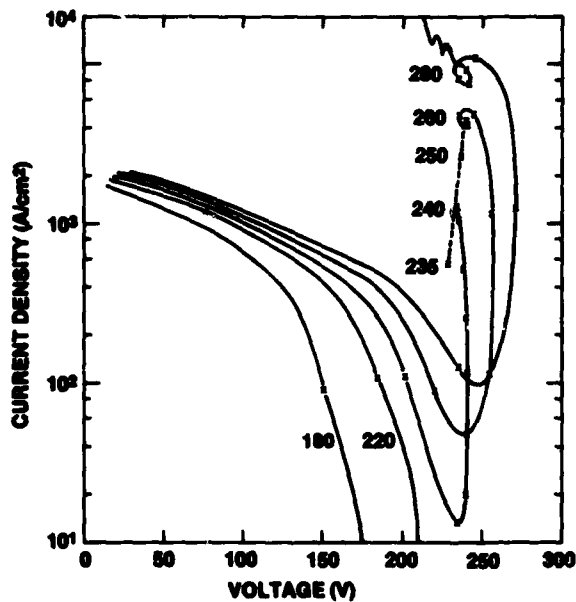


Figure 102. Dynamic current density versus voltage curves for 12- μ m PIN diode. Applied voltage is given as parameter. $R = 50 \Omega$ and $C = 1 \times 10^{-12}$ F. Stored charge ($t = 0$) was less for these calculations than for those of figure 101. Points along solid lines indicate time intervals of 0.1 ns. Dashed curve is static characteristic.

The dynamic impedance during the switching transient may be calculated by superimposing a small ac signal (1 or 2 V) on the applied voltage. Since the various switching stages are of nanosecond or sub-nanosecond duration, frequencies of from 5 to 20 GHz have been used. For reverse switching, the impedance is low during the charge storage time, and the phase angle between the current and voltage is found to be about 5 to 10 deg capacitive. The impedance and phase angle increase during the carrier sweep out. The dynamic diode capacitance may be determined from the impedance and phase angle. This capacitance is found to agree with that calculated from the width of the depletion regions during the SCL sweep out. During the final SCF sweep out of carriers, the phase angle is about 80 to 90 deg capacitive. The calculated capacitance is then smaller than that calculated for a fully depleted diode. This may be because of the inductive effect of the residual current.

When the diode is reverse switched at a high enough voltage to induce avalanche, the phase angle becomes more inductive. The calculated phase angle for the 12- μ m PIN diode is shown as a function of current density in figure 103. At each frequency there is a transition from a capacitive reactance ($\theta = 270$ deg) to an inductive reactance ($\theta = 90$ to 110 deg) as J increases. The transition occurs at higher J for higher frequencies. The calculated impedance as a function of J is shown in figure 104, where an area of 1×10^{-4} cm² has been assumed. The impedance increases slightly as J increases and reaches a maximum when the diode is a pure negative resistance ($\theta = 180$ deg). The calculated inductance as a function of I is shown in figure 105. The inductance decreases approximately as $I^{-1/2}$, as found more directly in other calculations discussed earlier. These calculations are for lower current densities than previous ones; a possible maximum value for L was anticipated, but not found.

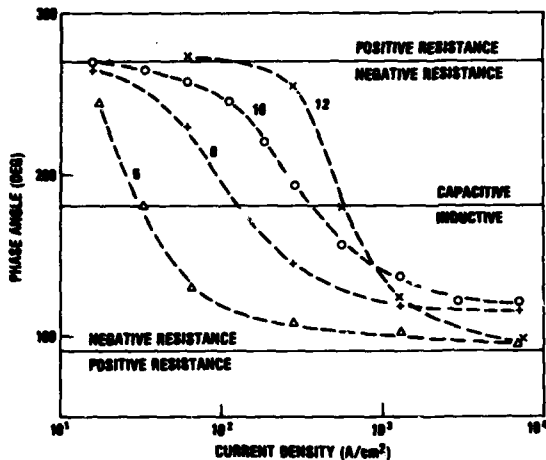


Figure 103. Calculated phase angle as function of current density determined from superimposed ac signal of frequency in G., labeled for each curve. Capacitive, inductive, and positive and negative resistance regions are marked.

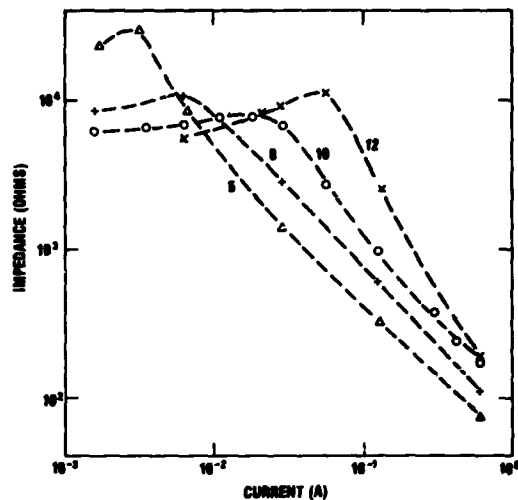


Figure 104. Impedance as function of current calculated at frequency (GHz) labeled.

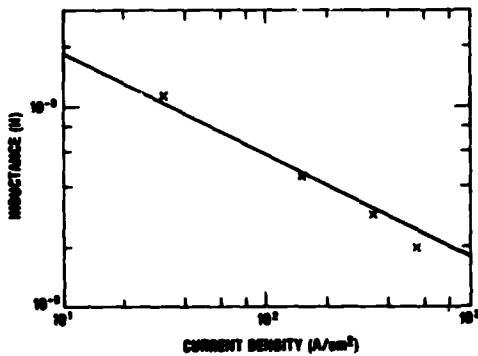


Figure 105. Inductance as function of current density determined from figures 103 and 104, assuming resonance with device capacitance.

Factor of 10^6 , meaningful comparisons can be made only in terms of current density. It should be mandatory for diode manufacturers to publish the area of each device.

17. FURTHER DISCUSSION

I feel that it is unfortunate that the term "breakdown" is used so extensively in the semiconductor field to designate the first appearance of current in a reverse-biased junction. Rather than the breakdown voltage, I would prefer the term "avalanche voltage" as more accurate. Then the awkward term "second breakdown" would be avoided. Breakdown would then be defined as the maximum voltage attainable under the cited condition. Further, it would be logical to define the avalanche voltage in terms of current density, rather than total current. When device areas range over more than a

It would also be useful in predicting second breakdown if the nominal PTF of each diode were available. Alternatively, the doping level and the diode width could be given. These data would be useful in predicting the ratio of second to first breakdown voltages and the magnitude of the expected space-charge resistance. Further, the doping level, if available directly, or indirectly from the PTF, gives the best criterion for the appearance of double avalanching. Specifically, the criterion is that the diode current density should not exceed the product of the doping density, the saturation carrier velocity ($\sim 1 \times 10^7$ cm/s at 300 K), and the electronic charge. To use this criterion it is necessary to know both the diode area and the doping level. The application of the criterion to diodes of different doping levels is shown in figure 106. It is seen that the critical current increases with the doping level and indicates a current level on the static characteristic just below the point of negative resistance. Since double avalanching occurs at roughly one-half the current for a negative resistance and its resultant current channeling, the criterion offers a safety margin for the prediction of second breakdown. This criterion is not adequate where the applied voltage pulse length is the same or greater than the device's thermal time constant. Then, lower currents over long times can cause damaging heating. However, it is the short-duration high-power pulse regime where the experimental scatter is largest and the thermal models are most inadequate. The proposed criterion would be of both general and particular use here. In general, for low doping levels, even low currents are unsafe; damage can occur when the first breakdown voltage is barely exceeded. A large series resistance may be called for. In particular, the criterion is most useful if impedance measurements can be made above first breakdown. Then the voltage required to exceed the current criterion becomes known and that can be used as an alternative criterion on voltage or power. Since the saturation velocity decreases with temperature, the critical current will also decrease with temperature, whereas the critical voltage will increase with temperature.

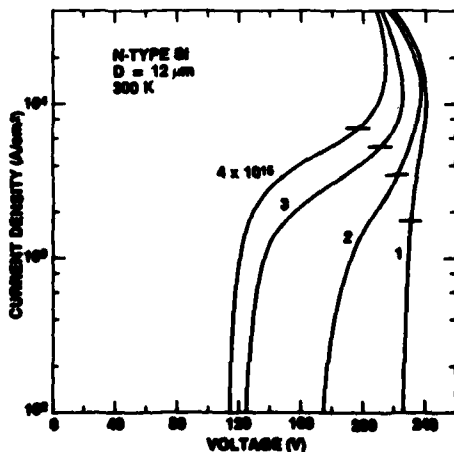


Figure 106. Static characteristics of 12- μ m N-type diodes. Doping levels are given as parameter. Horizontal lines indicate equality of mobile electron and of doping densities, a predictor of double avalanching.

The criterion that the mobile charge density not exceed the doping level is one that has been introduced previously. However, the physical justifications of the criterion have been faulty. It has often been correlated with "avalanche quenching," elimination of the "junction," or similar concepts. Supposedly, the removal of the high field at the junction allows the thermal current to "run away." While the present calculations show that the junction avalanche multiplication decreases with temperature, the junction field actually increases. In any case, avalanche quenching would reduce, not increase, the total current. The separation of the high resistivity region of a diode into junction and bulk regions is also misleading. Bulk regions should be limited to doping densities of $\sim 10^{19}$ to 10^{21} cm^{-3} . The high resistivity region of the diode may be correctly separated into depleted and undepleted regions. Then the undepleted region can be characterized by its resistivity. One must be aware that the edge of the depletion region moves as a function of V until the edge reaches the high doping region. Finally, if the "junction" were eliminated at high currents, the reverse-biased diode would be equivalent to the forward-biased diode. Since the forward-biased diode will sustain higher currents than the reverse-biased diode, a contradiction is evident. The presence of a negative resistance current regime in the reverse-biased diode and its absence in the forward-biased diode make the critical difference.

The other common criterion for second breakdown is that the temperature increase causes the diode to become "intrinsic." To quote Kalab:⁵ "The intrinsic state within the junction is achieved when minority carrier density becomes equal to the majority carrier density due to a temperature rise within the junction. At the critical intrinsic temperature, it was postulated that the device could no longer sustain the electric field stress necessary to maintain avalanche behavior, and thus would enter a second breakdown mode leading to eventual damage." Usually, the intrinsic temperature is identified from resistivity versus temperature curves (fig. 3). As discussed earlier (sect. 4), the low-field resistivity curves are not valid for the high-field junction region of the diode. The question has been asked, what replaces the resistivity versus temperature curves at high fields? Unfortunately there is no replacement. It is necessary to use the static characteristics at various temperatures for each device doping and width. Further, the intrinsic temperature defined by the equality of minority and majority carriers is a confused picture. As discussed in section 10, thermal generation is insignificant in the high-field region, since the recombination-thermal generation lifetime is three or more orders of magnitude greater than the carrier transit time. At very high currents, the minority and majority carriers do become nearly equal, forming a plasma.

⁵B. Kalab, *Analysis of Failure of Electronic Circuits for EMP Induced Signals--Review and Contribution*, Harry Diamond Laboratories, HDL-TR-1615 (August 1973).

The analogy between the glow and arc transitions in gases with the first and second breakdowns in semiconductors has often been made. I believe this analogy is more complete than has been postulated. First, all the basic equations used in the computer program are essentially the same for semiconductors and gases, except for the pressure variation in gases, the doping level in semiconductors, and the form of the recombination rate expressions. The doping level in the semiconductor is in many ways an inverse analog of pressure, p_g , in the gas. Gas breakdown is a function only of the $p_g d$ product, whereas in the semiconductor it is a function of $1/N$ (eq (26)) for d large and of d (eq (27)) for intrinsic material. In particular, the field dependence of the ionization coefficients (eq (12), (13)) and of the mobilities (eq (14), (15)) is the same in gases and semiconductors. In contrast, a major difference is that ions in a gas are orders of magnitude less mobile than are electrons, and consequently the same difference arises in the ionization coefficients, whereas each is of the same magnitude in semiconductors.

As is the case in semiconductors, breakdown in gases has been defined in many ways: appearance of a small fixed current, a certain large multiplication factor, attainment of a maximum voltage, and others. Studies of breakdown and of the glow and arc transition in gases have major advantages over those in semiconductors: visibility, larger physical dimensions, and a slower time scale. Although details are still controversial, the basic glow and arc transitions are well understood. The contraction into the glow is the consequence of an electrical negative resistance and the transition into the arc is a thermal electrode process. How close is the semiconductor analogy?

One test of the analogy is to compare field and charge distributions for the gaseous glow discharge and those of the semiconductor analog. The 400 K characteristics of the simulated 1N4148 diode, shown in a log plot in figure 62, are replotted on a linear scale in figure 107. As previously indicated, IMPATT oscillations occur at both low and high current densities, but may be damped out with the use of higher diffusion coefficients. Field distributions corresponding to the numbered points in figure 107 are shown in figure 108, and the corresponding charge distributions are shown in figure 109. In the negative slope region, the field and charge distributions are remarkably like those observed in gaseous glow discharges. In particular, cathode fall, plasma, and anode fall regions may be distinguished. The function of the cathode fall (high field at the PN junction) is to inject electrons (through avalanching) into the plasma. A smaller anode fall (high field at the NN^+ junction) is required to inject a smaller number of holes into the plasma.

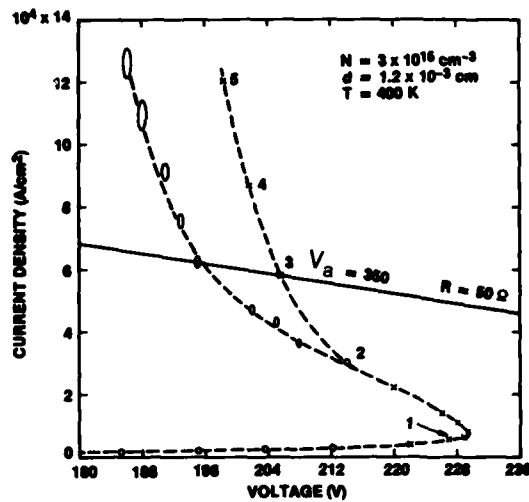


Figure 107. Characteristics of 12- μm N-type diode doped to $3 \times 10^{15} \text{ cm}^{-3}$ at 400 K. These same data are plotted on a log scale in figure 63. Ellipses indicate presence of IMPATT oscillations; 50- Ω load line for a diode area of $5 \times 10^{-5} \text{ cm}^2$ and $V_a = 350 \text{ V}$ is shown.

Dumin⁴¹ has observed visible radiation from plasmas in silicon diodes during second breakdown. He found that the junction was necessary to ignite the plasma. At the highest currents the average field was quite low. Visible radiation during second breakdown has also been observed at Harry Diamond Laboratories. Portnoy and Gamble⁴² found two or more stages (voltage steps) in second breakdown. It is quite likely that they observed the effect of one or more avalanche oscillations. As shown in figures 63 and 107, the voltage changes when oscillations appear or change modes.

⁴¹D. J. Dumin, *Emission of Visible Radiation from Extended Plasmas in Silicon Diodes During Second Breakdown*, *IEEE Trans. Electron Devices*, ED-16 (May 1969), 479-485.

⁴²W. M. Portnoy and F. R. Gamble, *Fine Structure and Electromagnetic Radiation in Second Breakdown*, *IEEE Trans. Electron Devices*, ED-11 (October 1964), 470-478.

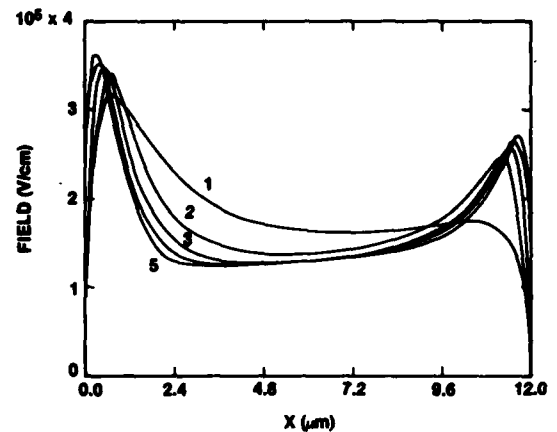


Figure 108. Field distributions for current density/voltage points as numbered in figure 107.

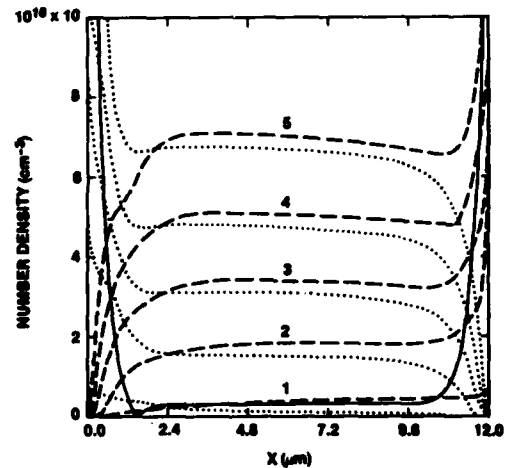


Figure 109. Distribution of electron and hole densities for numbered points of figure 107. Solid curve gives doping profile; dashed lines are for electrons and dotted lines for holes.

Gaseous glow discharges may be classified, in the order of increasing current, as subnormal, normal, or abnormal. The subnormal discharge is in the negative resistance region; it is usually oscillating. The normal discharge has a constant J ; the area changes as the applied voltage is increased. When the cathode is fully covered, a higher voltage is required to increase the current density, resulting in the abnormal glow. There are strong indications of a minimum voltage near the highest currents calculable in some of the present semiconductor computer calculations. The decreasing slope (from the vertical) of the characteristic is noted at the highest currents shown in figure 107. During oscillations, pulse currents can reach a much higher magnitude than can be calculated in static conditions. When the current peaks of the dynamic characteristics of differing applied voltages are joined, the voltage shows a minimum at a current slightly above that calculable for the static case and increases considerably for higher currents. As shown in figure 63, the current maxima and minima during oscillations are on the static characteristic.

The glow to arc transition in a gaseous discharge tube occurs as a result of cathode heating. Thermal emission replaces the cathode fall as an electron source. In the same way, the thermal injection current (sect. 10) in the semiconductor can negate the need for a high junction field. In the gaseous discharge, there is an exact correlation with the appearance of a negative resistance and the contraction of the visible discharge. Current densities can be calculated from the observed discharge area. The measured J-V characteristic then agrees with the calculated characteristic from breakdown to the abnormal glow. In the semiconductor, the channeling cannot be observed directly in conventional devices, but is evidenced by melt channels in damaged devices.

Relaxation oscillations in the gaseous subnormal glow discharge are well known. Section 14 shows that they are observed in silicon diodes. Moving striations are generally present in the positive column (plasma) of a gaseous glow discharge. While these striations are not completely understood, they have been proven to arise in the cathode and/or the anode fall regions. There is an almost complete analogy to what has been named the traveling-wave IMPATT mode (Ward²⁵). One must conclude that the analogy between the gaseous glow and arc discharges and the steps of the second breakdown process is a most useful one.

18. SUMMARY AND RECOMMENDATIONS

18.1 Summary

After a brief historical introduction to second breakdown, an electrothermal model computer program is described. The formulation and

²⁵A. L. Ward, *Modes of Avalanche Oscillations in Silicon Diodes*, *IEEE Trans. Electron Devices*, ED-25 (June 1978), 683-687.

procedures are listed and discussed. The material parameters of silicon are described. The various current regimes of the reverse-biased static characteristics are discussed. It is shown that space charge causes double avalanching, which in turn results in a negative differential resistance and current channeling. Dynamic characteristics are presented for constant overvoltages and for constant temporal rates of voltage increase. Both isothermal and adiabatic thermal calculations are made. It is shown that thermal injection currents are the critical thermal process. One-sided, two-sided, and linearly graded doping profiles are compared. Although direct calculations are limited to the nanosecond time scale, it is shown that longer times may be simulated by combining knowledge of the temperature variation of static characteristics, the rate of temperature rise as a function of current, and the thermal time constant of the diode. Good agreement has been obtained with published measurements of power as a function of breakdown time up to 100 μ s for the 1N4148 diode. The combined effect of ionizing radiation and high electrical stress is calculated. It is shown that the frequency of avalanche oscillations can be used as a dynamic temperature monitor of the junction region. High-current forward-bias static characteristics are calculated. It is shown that the higher power capability of the forward-biased diode results from the absence of a negative resistance. Reverse switching transients into reverse breakdown are calculated. The analogy of second breakdown processes in semiconductors with the glow and arc discharges in gases is discussed and found to be reasonably accurate.

18.2 Recommendations

Until recently, the experimental work on second breakdown far outpaced the theoretical studies. Now, the limitations on the available measurements are handicapping theoretical progress. This has resulted from the lack of pertinent information in the experimental publications. Very few papers furnish the diode area, doping profile (or even the doping level or diode width), and the thermal time constant (or the thermal resistance) needed for calculations. Close cooperation is needed between the theoretical and experimental work in second breakdown in order to expedite solutions to diode damage susceptibility problems.

It is planned to continue the exploitation of the electrothermal model computer program in simulating as wide a variety of problems as possible. Feasibility studies should be made in further improvements to the program. Of highest priority is the investigation of using larger time steps for thermal processes whenever the electrical processes are in quasi-equilibrium. Second priority should be given to extending the calculations to two dimensions. This would allow quantitative calculations of current channeling in the negative resistance regime and would allow nonplanar geometries to be studied.

At present, the time scale is extended by hand calculations. This could be programmed for computer calculation, either directly or by circuit simulation codes. Only lack of money and personnel has delayed this important step in developing an engineering model; it should be developed as soon as possible.



ACKNOWLEDGEMENTS

Bohdan Dobriansky, of Harry Diamond Laboratories, measured the diode areas, junction depths, and contact material of the 1N645 and the 1N4148.

Christian Fazi, also of Harry Diamond Laboratories, measured the avalanche oscillations and took the photograph of figure 72.

LITERATURE CITED

- (1) J. Tauc and A. Abraham, Thermal Breakdown in Silicon P-N Junctions, *Phys. Rev.*, 108 (1957), 936-937.
- (2) C. G. Thornton and C. D. Simmons, A New High Current Mode of Transistor Operation, *IRE Trans. Electron Devices*, ED-5 (January 1958), 6-10.
- (3) L. W. Ricketts, J. E. Bridges, and J. Miletta, *EMP Radiation and Protective Techniques*, John Wiley and Sons, New York (1976).
- (4) H. A. Schafft, Second Breakdown--A Comprehensive Review, *Proc. IEEE*, 55 (August 1967), 1272-1278.
- (5) B. Kalab, Analysis of Failure of Electronic Circuits for EMP Induced Signals--Review and Contribution, Harry Diamond Laboratories, HDL-TR-1615 (August 1973).
- (6) R. H. Dickhaut, Electromagnetic Pulse Damage to Bipolar Devices, Circuits and Systems (Magazine), 10 (April 1976), 8-21.
- (7) A. L. Ward, An Electro-Thermal Model of Second Breakdown, *IEEE Trans. Nucl. Sci.*, NS-23 (December 1976), 1679-1684.
- (8) W. Börsch-Supan and H. Oser, Numerical Computation of the Temporal Development of Currents in a Gas Discharge Tube, *J. Res., National Bureau of Standards*, 67B (January 1963), 41-60.
- (9) J. L. Scales and A. L. Ward, Effects of Space Charge on Mobility, Diffusion, and Recombination of Minority Carriers, *J. Appl. Phys.*, 39 (February 1968), 1692-1700.
- (10) A. L. Ward, Studies of Second Breakdown in Silicon Diodes, *IEEE Trans. Parts and Hybrids Packag.*, PHP-13 (December 1977), 361-368.
- (11) A. L. Ward, Calculations of Second Breakdown, *IEEE Trans. Nucl. Sci.*, NS-24 (December 1977), 2357-2360.
- (12) A. L. Ward, Doping Profiles and Second Breakdown, *Proceedings, 1979 Electrical Overstress/Electrostatic Discharge Conference, Denver, CO (1979)*, 25-77. Reliability Analysis Center, Rome Air Development Center, EOS-1, 109-115.
- (13) A. L. Ward, Effect of Space Charge Upon the Transport of Charge Carriers, *J. Appl. Phys.*, 35 (March 1964), 469-474.
- (14) R. Van Overstraeten and H. DeMan, Measurement of the Ionization Rates in Diffused Silicon p-n Junctions, *Solid-State Electron.*, 13 (1970), 583-608.

LITERATURE CITED (Cont'd)

- (15) C. R. Crowell and S. M. Sze, Temperature Dependence of Avalanche Multiplication in Semiconductors, *Appl. Phys. Lett.*, 9 (September 1966), 242-244.
- (16) S. M. Sze, *Physics of Semiconductor Devices*, Wiley-Interscience, New York (1969), 39-41, 57-59, 121-126.
- (17) C. Y. Duh and J. L. Moll, Electron Drift Velocity in Avalanche Silicon Diodes, *IEEE Trans. Electron Devices*, ED-14 (January 1967), 46-49.
- (18) C. Canali, G. Majni, R. Minder, and G. Ottaviani, Electron and Hole Drift Velocity Measurements and Their Empirical Relation to Electric Field and Temperature, *IEEE Trans. Electron Devices*, ED-22 (November 1975), 1045-1047.
- (19) L. H. Holway, Jr., Electron-Hole Avalanches with Constant Ionization Coefficients, *IEEE Trans. Electron Devices*, ED-26 (June 1979), 991-993.
- (20) A. S. Grove, *Physics and Technology of Semiconductor Devices*, John Wiley and Sons, New York (1967), 44-52, 194-201.
- (21) H. Yanai, H. Torizuka, N. Yamada, and K. Ohkubo, Experimental Analysis for the Large-Amplitude High-Efficiency Mode of Oscillation with Si Avalanche Diode, *IEEE Trans. Electron Devices*, ED-17 (December 1970), 1067-1076.
- (22) R. A. Sunshine and M. A. Lampert, Second Breakdown Phenomena in Avalanche Silicon-on-Sapphire Diodes, *IEEE Trans. Electron Devices*, ED-19 (July 1972), 873-885.
- (23) C. A. Lee, R. A. Logan, R. L. Batdorf, J. J. Kleimack, and W. Wiegmann, Ionization Rates of Holes and Electrons in Silicon, *Phys. Rev.*, A134 (May 1964), A761-773.
- (24) S. L. Miller, Ionization Rates for Holes and Electrons in Silicon, *Phys. Rev.*, 105 (February 1957), 1246-1249.
- (25) A. L. Ward, Modes of Avalanche Oscillations in Silicon Diodes, *IEEE Trans. Electron Devices*, ED-25 (June 1978), 683-687.
- (26) D. M. Tasca, J. C. Peden, and J. Miletta, Non-Destructive Screening for Second Breakdown, *IEEE Trans. Nucl. Sci.*, NS-19 (December 1972), 57-67.
- (27) W. N. Grant, Electron and Hole Ionization Rates in Epitaxial Silicon at High Electric Fields, *Solid-State Electron.*, 16 (1973), 1189-1203.

LITERATURE CITED (Cont'd)

- (28) W. L. Vault, Response of Integrated Circuits to a Simulated IEMP Environment, Harry Diamond Laboratories, HDL-TR-1649 (October 1973).
- (29) D. H. Habing, Response of Bipolar Transistors to Combined EMP and Ionization Environment, IEEE Trans. Nucl. Sci., NS-17 (December 1970), 360-363.
- (30) B. F. Hartman and D. C. Evans, Electrical Pulse Burnout of Transistors in Intense Ionizing Radiation, IEEE Trans. Nucl. Sci., NS-22 (December 1975), 2528-2532.
- (31) W. T. Read, A Proposed High-Frequency Negative Resistance Diode, Bell Syst. Tech. J., 37 (March 1958), 401-446.
- (32) R. L. Johnston, B. C. DeLoach, Jr., and B. G. Cohen, A Silicon Diode Microwave Oscillator, Bell Syst. Tech. J., 47 (1964), 369-372.
- (33) H. J. Prager, K. K. N. Chang, and S. Weisbrod, High-Power, High-Efficiency Silicon Avalanche Diodes at Ultra-High Frequencies, Proc. IEEE (Lett.), 55 (April 1967), 586-587.
- (34) R. L. Johnston, D. L. Scharfetter, and D. J. Bartelink, High-Efficiency Oscillations in Germanium Avalanche Diodes Below the Transit-Time Frequency, Proc. IEEE (Lett.), 56 (September 1968), 1611-1613.
- (35) A. L. Ward and B. J. Udelson, Computer Calculations of Avalanche-Induced Relaxation Oscillations in Silicon Diodes, IEEE Trans. Electron Devices, ED-15 (November 1968), 847-851.
- (36) A. L. Ward, Further Calculations of the Relaxation Avalanche Mode, Proc. 4th Cornell Electrical Engineering Conference, Ithaca, NY (1973), 391-400.
- (37) A. L. Ward and L. G. Schneekloth, Calculations of Relaxation Oscillations in Gas Tube Circuits, Harry Diamond Laboratories, HDL-TR-1166 (August 1963).
- (38) R. V. Garver, R. H. Femenias, Vasco C. Martins, J. L. Washington, Gary L. Roffman, R. J. Reyzer, Samuel A. Clark, Jr., and Morris Campi, Systems Performance Analysis of the Electromagnetic Pulse Effects on Defense Communications System Transmission Systems, Final Report (U), Harry Diamond Laboratories, HDL-TR-1951 (February 1982). (SECRET-RESTRICTED DATA/NOFORN)

LITERATURE CITED (Cont'd)

- (39) D. P. Kennedy, The Potential and Electric Field at the Metallurgical Boundary of an Abrupt p-n Semiconductor Junction, IEEE Trans. Electron Devices, ED-22 (November 1975), 988-994.
- (40) P. C. H. Chan and C. T. Sah, Experimental and Theoretical I-V Characteristics of Zinc-Doped Silicon p-n Junctions Using Exact DC Circuit Model, IEEE Trans. Electron Devices, ED-26 (June 1979), 937-941.
- (41) D. J. Dumin, Emission of Visible Radiation from Extended Plasmas in Silicon Diodes During Second Breakdown, IEEE Trans. Electron Devices, ED-16 (May 1969), 479-485.
- (42) W. M. Portnoy and F. R. Gamble, Fine Structure and Electromagnetic Radiation in Second Breakdown, IEEE Trans. Electron Devices, ED-11 (October 1964), 470-478.

SYMBOLS AND ACRONYMS

A	Diode area (cm)
A_i	Constants, electron ionization
B_i	Constants, hole ionization
C	Capacitance (F)
C_i	Constants, mobility
D, D_+, D_-	Diffusion coefficient (cm ² /s)
D_{th}	Thermal diffusivity (cm ² /s)
E	Electric field (V/cm)
E_g	Band gap of semiconductor (eV)
F	Fraction, defined by equation (8)
I	Total current (A)
J	Total current density (A/cm ²)
J_0	Boundary current density (A/cm ²)
J_+, J_-	Electron, hole current density (A/cm ²)
L	Distance to heat sink (cm)
L	Inductance (H)
M	$d/\Delta x$, multiplication factor
$N = N_D - N_A$	Net doping level (cm ⁻³)
P	Power (W)
R, R'	Recombination rate
R_s, R_d	Series resistance, diode resistance (Ω)
T	Temperature (K)
V	Voltage (V)
V_a	Applied voltage (V)

SYMBOLS AND ACRONYMS (Cont'd)

V_{B1}	First breakdown voltage (V)
V_{B2}	Second breakdown voltage (V)
W	Maximum depletable width (cm)
c	Heat capacity (J/g C)
d	Diode width (cm)
d_B	Depletion width at breakdown (cm)
e	Electron charge (Coulombs)
k	Boltzmann constant (J/C)
k_T	Thermal conductivity (W/cm C)
m	Index
n	Electron density (cm)
n_i	Intrinsic density (cm)
p	Hole density (cm)
$t, \Delta t$	Time, time step (s)
v	Carrier velocity (cm/s)
$x, \Delta x$	Distance, distance step (cm)
α	Ionization coefficient, electrons (cm)
β	Ionization coefficient, holes (cm)
ϵ_0	Permittivity of free space (F/cm)
θ	Thermal resistance (C/W)
θ	Phase lag (deg)
κ	Dielectric constant
λ	Growth constant
μ_0	Low-field mobility (cm/Vs)
μ_+, μ_-	Mobility of holes, electrons (cm/Vs)

SYMBOLS AND ACRONYMS (Cont'd)

ρ	Density (g/cm)
σ	Electrical conductivity (A/V cm)
τ	Dielectric relaxation time (s)
τ_p, τ_n	Recombination lifetime (s)
τ_{th}	Thermal time constant
EMP	Electromagnetic pulse
NDR	Negative differential resistance (resistivity)
PIN	Diode with intrinsic region
PTF	Punch-through factor
SCF	Space charge free
SCL	Space charge limited
RAM	Relaxing (or relaxation) avalanche mode

DISTRIBUTION

ADMINISTRATOR
DEFENSE TECHNICAL INFORMATION CENTER
ATTN DTIC-DDA (12 COPIES)
CAMERON STATION, VA 22314

COMMANDER
US ARMY RSCH & STD GP (EUR)
ATTN CHIEF, PHYSICS & MATH BRANCH
FPO NEW YORK 09510

COMMANDER
US ARMY MISSILE & MUNITIONS
CENTER & SCHOOL
ATTN ATSK-CTD-F
REDSTONE ARSENAL, AL 35809

DIRECTOR
US ARMY MATERIEL SYSTEMS
ANALYSIS ACTIVITY
ATTN DRXSY-MP
ATTN DRXSY-PO
ABERDEEN PROVING GROUND, MD 21005

DIRECTOR
US ARMY BALLISTIC RESEARCH LABORATORY
ATTN DRDAR-TSB-S (STINFO)
ATTN DRDAR-BLB, W. VANANTWERP
ATTN DRDAR-BLE
ABERDEEN PROVING GROUND, MD 21005

US ARMY ELECTRONICS TECHNOLOGY
& DEVICES LABORATORY
ATTN DELET-DD
FT MONMOUTH, NJ 07703

HQ USAF/SAMI
WASHINGTON, DC 20330

TELEDYNE BROWN ENGINEERING
CUMMINGS RESEARCH PARK
ATTN DR. MELVIN L. PRICE, MS-44
HUNTSVILLE, AL 35807

ENGINEERING SOCIETIES LIBRARY
ATTN ACQUISITIONS DEPARTMENT
345 EAST 47TH STREET
NEW YORK, NY 10017
CENTRAL INTELLIGENCE AGENCY
ATTN OSWR/NED
WASHINGTON, DC 20505

DEPARTMENT OF TRANSPORTATION
FEDERAL AVIATION ADMINISTRATION
HEADQUARTERS SEC DIV, ASE-300
800 INDEPENDENCE AVENUE, SW
ATTN SEC DIV ASE-300
WASHINGTON, DC 20591

DIRECTOR
FEDERAL EMERGENCY MANAGEMENT AGENCY
OFFICE OF RESEARCH/NPP
500 C STREET, SW
ATTN STATE & LOCAL PROG. SUPPORT
ATTN ASSISTANT ASSOCIATED DIR
WASHINGTON, DC 20472

FEDERAL PREPAREDNESS AGENCY
GENERAL SERVICES ADMINISTRATION
18TH & F STREETS, NW
ATTN ESTE-M. MURTHA
WASHINGTON, DC 20405

DEPARTMENT OF ENERGY
ALBUQUERQUE OPERATIONS OFFICE
PO BOX 5400
ATTN CTID
ATTN WSSB
ALBUQUERQUE, NM 87115

DEPARTMENT OF ENERGY
ECONOMIC REGULATORY ADMINISTRATION
OFFICE OF UTILITIES SYSTEMS
DIV OF POWER SUPPLY & RELIABILITY (EEPA)
1111 20TH STREET, NW
ATTN OFFICE OF UTILITY SYSTEMS/L. O'NEILL
WASHINGTON, DC 20461

ASSISTANT TO THE SECRETARY OF DEFENSE
(ATOMIC ENERGY)
ATTN MILITARY APPLICATIONS
ATTN EXECUTIVE ASSISTANT
WASHINGTON, DC 20301

DIRECTOR
DEFENSE COMMUNICATIONS AGENCY
ATTN CODE 330
ATTN CODE 312
ATTN CODE C313
WASHINGTON, DC 20305

DEFENSE COMMUNICATIONS ENGINEERING CENTER
ATTN CODE R400
ATTN CODE R720, C. STANSBERRY
ATTN CODE R123, TECH LIB
1860 WIENLE AVENUE
RESTON, VA 22090

DIRECTOR
DEFENSE INTELLIGENCE AGENCY
ATTN DB 4C2, D. SPOHN
ATTN RTS-2A, TECH LIB
WASHINGTON, DC 20301

DIRECTOR
DEFENSE NUCLEAR AGENCY
ATTN NATA
ATTN TITL
ATTN RAEV

DISTRIBUTION (Cont'd)

DEFENSE NUCLEAR AGENCY (Cont'd)
ATTN STNA
ATTN RAEH
WASHINGTON, DC 20305

COMMANDER
FIELD COMMAND
DEFENSE NUCLEAR AGENCY
ATTN FCTT, G. GANONG
ATTN FCPR, J. T. MCDANIEL
ATTN FCLMC, H. R. PUTNAM
ATTN FCTT, W. SUMMA
ATTN FCTT
KIRTLAND AFB, NM 87115

CHIEF
FIELD COMMAND
DEFENSE NUCLEAR AGENCY
LIVERMORE BRANCH
PO BOX 808 L-317
ATTN FCPL
LIVERMORE, CA 94550

DIRECTOR
ARMED FORCES RADIOBIOLOGY
RESEARCH INSTITUTE
DEFENSE NUCLEAR AGENCY
ATTN RESEARCH PROGRAM COORDINATING OFFICER
NATIONAL NAVAL MEDICAL CENTER
BETHESDA, MD 20014

DIRECTOR
DEFENSE ADVANCED RSCH PROJ AGENCY
ATTN TIO-A. LOWREY
ARCHITECT BUILDING
1400 WILSON BLVD.
ARLINGTON, VA 22209

DIRECTOR
INTERSERVICE NUCLEAR WEAPONS SCHOOL
ATTN TTV
KIRTLAND AFB, NM 87115

JOINT CHIEFS OF STAFF
ATTN J-3 RM 2D874
WASHINGTON, DC 20301

DIRECTOR
JOINT STRAT TGT PLANNING STAFF
OFFUTT AFB
ATTN JPST
ATTN JLA, THREAT APPLICATIONS DIV
ATTN JSAS
ATTN NRI-STINFO LIBRARY
OMAHA, NE 68113

NATIONAL COMMUNICATIONS SYSTEM
OFFICE OF THE MANAGER
DEPARTMENT OF DEFENSE
ATTN NCS-TS
WASHINGTON, DC 20305

DIRECTOR
NATIONAL SECURITY AGENCY
ATTN TDL
ATTN R-52, O. VAN GUNTEN
ATTN S-232, D. VINCENT
FT MEADE, MD 20755

UNDER SECY OF DEF FOR RSCH & ENGRG
DEPARTMENT OF DEFENSE
ATTN STRATEGIC & SPACE SYS
(OS) RM 3E129
WASHINGTON, DC, 20301

COMMANDER
BMD SYSTEMS COMMAND
DEPARTMENT OF THE ARMY
PO BOX 1500
ATTN BMDSC-AOLIB
ATTN BMDSC-HLE, R. WEBB
ATTN BMDSC-HW, R. DEKALB
HUNTSVILLE, AL 35807

COMMANDER
ERADCOM TECHNICAL SUPPORT ACTIVITY
DEPARTMENT OF THE ARMY
ATTN DELET-IR, E. HUNTER
FT MONMOUTH, NJ 07703

OPM SINGARS
DEPARTMENT OF THE ARMY
ATTN DRCPM-GARS-TM
HQ US ARMY COMMUNICATIONS & ELECTRONICS
MATERIEL READINESS COMMAND
FT MONMOUTH, NJ 07703

PROJECT OFFICER
US ARMY COMMUNICATIONS RES &
DEV COMMAND
ATTN DRCPM-ATC
ATTN DRDCO-SEI
ATTN DRCPM-TDS-BSI
FT MONMOUTH, NJ 07703

DIVISION ENGINEER
US ARMY ENGINEER DIV, HUNTSVILLE
ATTN HNDSD-SR
ATTN A. T. BOLT
PO BOX 1600, WEST STATION
HUNTSVILLE, AL 35807

COMMANDER
US ARMY MISSILE COMMAND
ATTN DRCPM-PE-EA, W. O. WAGNER
ATTN DRCPM-PE-EG, W. B. JOHNSON
ATTN DRCPM-LCEV, H. HENRIKSEN
ATTN DOCUMENTS SECTION, BLDG 4484
ATTN DRDMI TBD
ATTN DRDMI EAA
REDSTONE ARSENAL, AL 35809

DISTRIBUTION (Cont'd)

COMMANDER
US ARMY TEST & EVALUATION COMMAND
ATTN DRSTE-FA
ABERDEEN PROVING GROUND, MD 21005

COMMANDER
US ARMY TRAINING & DOCTRINE COMMAND
ATTN ATORI-OP-SW
FT MONROE, VA 23651

DEP CH OF STAFF FOR RSCH DEV & ACQ
DEPARTMENT OF THE ARMY
ATTN DAMA-N-CSS, E. DRISCOLL
WASHINGTON, DC 20310

COMMANDER
ELECTRONICS TECH & DEVICES LAB
US ARMY ELECTRONICS R&D COMMAND
ATTN DELCS-K, B. MARKOW
FT MONMOUTH, NJ 07703

COMMANDER
DEPARTMENT OF THE ARMY
ATTN CCH-PCA-TR
FT HUACHUCA, AZ 85613

COMMANDER
US ARMY ARMOR CENTER
ATTN TECHNICAL LIBRARY
FT KNOX, KY 40121

COMMANDER
US ARMY COMM-ELEC ENGRG INSTAL AGENCY
ATTN CCC-CED-SES
FT HUACHUCA, AZ 85613

COMMANDER
US ARMY COMMUNICATIONS COMMAND
ATTN CC-LOG-LEO
ATTN CC-OPS-PD
ATTN CC-OPS-OS
ATTN ATSI-CD-MD
FT HUACHUCA, AZ 85613

CHIEF
US ARMY COMMUNICATIONS SYS AGENCY
DEPARTMENT OF THE ARMY
ATTN CCM-AD-SV
ATTN CCM-RD-T
FT MONMOUTH, NJ 07703

DIVISION ENGINEER
US ARMY ENGINEER DIV HUNTSVILLE
PO BOX 1600, WEST STATION
ATTN HNDED-SR
HUNTSVILLE, AL 35807

US ARMY INTEL THREAT ANALYSIS DET
BLDG A, ROOM 2201
ARLINGTON HALL STATION
ATTN ADMIN OFFICER
ARLINGTON, VA 22212

COMMANDER
US ARMY INTELLIGENCE & SEC CMD
ARLINGTON HALL STATION
4000 ARLINGTON BLVD
ATTN TECH INFO FAC
ATTN TECHNICAL LIBRARY
ARLINGTON, VA 22212

COMMANDER
US ARMY NUCLEAR & CHEMICAL AGENCY
7500 BACKLICK ROAD
BUILDING 2073
ATTN MONA-WE
SPRINGFIELD, VA 22150

COMMANDER
US ARMY TEST & EVALUATION COMD
ATTN DRSTE-EL
ATTN DRSTE-FA
ABERDEEN PROVING GROUND, MD 21005

COMMANDER
US ARMY TRAINING & DOCTRINE COMD
ATTN ATCD-Z
FT MONROE, VA 23651

COMMANDER
US ARMY WHITE SANDS MISSILE RANGE
ATTN STEWS-TE-AN, J. OKUMA
WHITE SANDS MISSILE RANGE, NM 88002

COMMANDER
NAVAL AIR SYSTEMS COMMAND
ATTN AIR 350F
WASHINGTON, DC 20361

OFFICER-IN-CHARGE
CIVIL ENGINEERING LABORATORY
ATTN CODE LO8A (LIBRARY)
ATTN CODE LO8A
NAVAL CONSTRUCTION BATTALION CENTER
PORT HUENEME, CA 93041

COMMANDER
NAVAL ELECTRONIC SYSTEMS COMMAND
ATTN PME 117-21
WASHINGTON, DC 20360

COMMANDER
NAVAL OCEAN SYSTEMS CENTER
ATTN CODE 8123, S. LICHTMAN
ATTN CODE 08, J. ROCKWAY
ATTN CODE 54, C. FLETCHER
ATTN CODE 7309, R. GREENWELL
SAN DIEGO, CA 92152

DISTRIBUTION (Cont'd)

COMMANDING OFFICER
NAVAL ORDNANCE STATION
ATTN STANDARDIZATION DIVISION
INDIAN HEAD, MD 20640

SUPERINTENDENT
NAVAL POSTGRADUATE SCHOOL
ATTN CODE 2124, LIBRARY
MONTEREY, CA 93940

COMMANDING OFFICER
NAVAL RESEARCH LABORATORY
ATTN CODE 2000, J. BROWN
ATTN CODE 2627, D. FOLEN
ATTN CODE 6624
ATTN CODE 6623, R. STATLER
ATTN CODE 1434, E. BRANCATO
ATTN CODE 6750
WASHINGTON, DC 20375

OFFICER IN CHARGE
NAVAL SURFACE WEAPONS CENTER
WHITE OAK LABORATORY
ATTN CODE F32, E. RATHBUN
ATTN CODE F30
SILVER SPRING, MD 20910

COMMANDER
NAVAL SURFACE WEAPONS CENTER
ATTN CODE F-56
DAHLGREN, VA 22448

COMMANDER
NAVAL WEAPONS CENTER
ATTN CODE 233, TECH LIB
CHINA LAKE, CA 93555

COMMANDING OFFICER
NAVAL WEAPONS EVALUATION FACILITY
KIRTLAND AIR FORCE BASE
ATTN CODE AT-6
ALBUQUERQUE, NM 87117

COMMANDING OFFICER
NAVAL WEAPONS SUPPORT CENTER
ATTN CODE 11E
CRANE, IN 47522

OFFICE OF NAVAL RESEARCH
ATTN CODE 427
ARLINGTON, VA 22217

OFFICE OF THE CHIEF OF NAVAL OPERATIONS
ATTN OP 981N1
WASHINGTON, DC 20350

DIRECTOR
STRATEGIC SYSTEMS PROJECT OFFICE
DEPARTMENT OF THE NAVY
ATTN NSP-27334
ATTN NSP 23C, D. GOLD

STRATEGIC SYSTEMS PROJECT OFFICE (Cont'd)
ATTN NSP-2702, J. PITSENBERGER
ATTN NSP-43, TECH LIB
ATTN NSP-2342, R. COLEMAN
WASHINGTON, DC 20376

COMMANDER
AERONAUTICAL SYSTEMS DIVISION, AFSC
ATTN ASD/ENAMA, J. CORBIN
ATTN ASD/YYEF
ATTN ASD/ENFTV
WRIGHT-PATTERSON AFB, OH 45433

COMMANDER
AEROSPACE DEFENSE COMMAND/DE
DEPARTMENT OF THE AIR FORCE
ATTN DEE
ENT AFB, CO 80912

AIR FORCE TECHNICAL APPLICATIONS CENTER
ATTN TFS, M. SCHNEIDER
PATRICK AFB, FL 32925

SAMSO/IN
AIR FORCE SYSTEMS COMMAND
PO BOX 92960
ATTN IND
(INTELLIGENCE)
WORLDWAY POSTAL CENTER
LOS ANGELES, CA 90009

SAMSO, MN
AIR FORCE SYSTEMS COMMAND
ATTN MNNH, MAJ M. BARAN
ATTN MNNH, CAPT R. I. LAWRENCE
(MINUTEMAN)
NORTON AFB, CA 92409

SAMSO/YA
AIR FORCE SYSTEMS COMMAND
ATTN YAPC
PO BOX 92960
WORLDWAY POSTAL CENTER
LOS ANGELES, CA 90009

STRATEGIC AIR COMMAND/XPFS
ATTN NRI-STINFO LIBRARY
ATTN DEL
ATTN GARNET E. MATZKE
ATTN XPFS, MAJ BRIAN G. STEPHAN
OFFUTT AFB, NE 68113

AIR FORCE WEAPONS LABORATORY/DYC
ATTN NTYEE, C. BAUM
ATTN NTN
ATTN CA
ATTN NTYE, J. CASTILLO
ATTN NTYEP, W. PAGE
ATTN NT
ATTN SUL

DISTRIBUTION (Cont'd)

AIR FORCE WEAPONS LABORATORY/DYC (Cont'd)
ATTN NXS
ATTN NTYC, M. SCHNEIDER
KIRTLAND AFB, NM 87117

COMMANDER
AIR LOGISTICS COMMAND
DEPARTMENT OF THE AIR FORCE
ATTN OO-ALC/MM
ATTN OO-ALC/MMEDC, L. KIDMAN
ATTN OO-ALC/MMETH, P. BERTHEL
HILL AFB, UT 84056

DIRECTOR
AIR UNIVERSITY LIBRARY
DEPARTMENT OF THE AIR FORCE
ATTN AUL-LSE
MAXWELL AFB, AL 36112

BALLISTIC MISSILE OFFICE/DAA
AIR FORCE SYSTEMS COMMAND
ATTN ENSN, W. WILSON
ATTN ENSN, W. CLARK
NORTON AFB, CA 92409

DEPUTY CHIEF OF STAFF
RESEARCH, DEVELOPMENT, & ACQ
DEPARTMENT OF THE AIR FORCE
ATTN AFRDQI
WASHINGTON, DC 20330

HEADQUARTERS
ELECTRONIC SYSTEMS DIVISION/YS
ATTN YSEA
HANSCOM AFB, MA 01731

COMMANDER
FOREIGN TECHNOLOGY DIVISION, AFSC
ATTN NIIS LIBRARY
ATTN TQTD B. BALLARD
WRIGHT-PATTERSON AFB, OH 45433

NORTHERN AMERICAN AIR DEFENSE TREATY
ATTN JSYE, P. CASTLEBERRY
PETERSON AFB, CO 80914

COMMANDER
ROME AIR DEVELOPMENT CENTER, AFSC
ATTN TSLD
GRIFFISS AFB, NY 13441

COMMANDER
SACRAMENTO AIR LOGISTICS CENTER
DEPARTMENT OF THE AIR FORCE
ATTN MMCRS, H. DELMASTRO
ATTN MMIRA, J. DEMES
ATTN MMSREM, F. SPEAR
MCCLELLAN AFB, CA 95652

SPACE DIVISION/IN
PO BOX 92960
WORLDWAY POSTAL CENTER
ATTN IND
LOS ANGELES, CA 90009

SPACE DIVISION/YL
PO BOX 92960
WORLDWAY POSTAL CENTER
ATTN YLXT
LOS ANGELES, CA 90009

STRATEGIC AIR COMMAND
DEPARTMENT OF THE AIR FORCE
ATTN NRI, G. MATZKE
ATTN NRI-STINFO LIBRARY
ATTN DEL
ATTN XPFS, G. SKLUZACEK
OFFUTT AFB, NE 68113

AEROSPACE CORP
PO BOX 92957
ATTN C. GREENHOW
ATTN I. GARFUNKEL
ATTN C. PEARLSTON
ATTN R. CROLIUS
ATTN J. REINHEIMER
ATTN LIBRARY
LOS ANGELES, CA 90009

AGBABIAN ASSOCIATES
250 N NASH STREET
ATTN LIBRARY
EL SEGUNDO, CA 90245

AVCO RESEARCH & SYSTEMS GROUP
201 LOWELL STREET
ATTN LIBRARY A830
WILMINGTON, MA 01887

BATTELLE MEMORIAL INSTITUTE
505 KING AVENUE
ATTN E. LEACH
COLUMBUS, OH 43201

BDM CORP
7915 JONES BRANCH DRIVE
ATTN CORPORATE LIBRARY
MCLEAN, VA 22102

BDM CORP
PO BOX 9274
ATTN LIBRARY
ALBUQUERQUE, NM 87119

BENDIX CORP
COMMUNICATION DIVISION
E JOPPA ROAD
ATTN DOCUMENT CONTROL
BALTIMORE, MD 21204

DISTRIBUTION (Cont'd)

BENDIX CORP
BENDIX CENTER
ATTN M. FRANK
SOUTHFIELD, MI 48075

BENDIX CORP
NAVIGATION & CONTROL GROUP
ATTN DEPT 6401
TETERBORO, NJ 07608

BOEING CO
PO BOX 3707
ATTN KENT TECHNICAL LIBRARY
ATTN V. JONES
ATTN D. KEMLE
ATTN H. WICKLEIN
ATTN B. HANRAHAN
SEATTLE, WA 98124

BOEING WICHITA CO
3801 S OLIVER STREET
ATTN L. WELLER
WICHITA, KS 67210

BROWN ENGINEERING COMPANY, INC
CUMMINGS RESEARCH PARK
ATTN FRED LEONARD
HUNTSVILLE, AL 35807

CALSPAN CORP
PO BOX 400
ATTN LIBRARY
BUFFALO, NY 14225

CHARLES STARK DRAPER LAB, INC
555 TECHNOLOGY SQUARE
ATTN K. FERTIG
ATTN TIC MS 74
CAMBRIDGE, MA 02139

CINCINNATI ELECTRONICS CORP
2630 GLENDALE-MILFORD ROAD
ATTN L. HAMMOND
CINCINNATI, OH 45241

COMPUTER SCIENCES CORP
1400 SAN MATEO BLVD, SE
ATTN A. SCHIFF
ALBUQUERQUE, NM 87108

CUTLER-HAMMER, INC
COMAC ROAD
ATTN E. KARPEN
DEER PARK, NY 11729

DIKEWOOD CORPORATION
1613 UNIVERSITY BLVD, NE
ATTN TECHNICAL LIBRARY
ATTN TECH LIB FOR/C. JONES
ATTN TECH LIB FOR/L. DAVIS
ALBUQUERQUE, NM 87102

DIKEWOOD CORPORATION
LOS ANGELES OPERATIONS
2716 OCEAN PARK BLVD
ATTN K. LEE
SANTA MONICA, CA 90405

E-SYSTEMS INC
GREENVILLE DIVISION PO BOX 1056
ATTN J. MOORE
GREENVILLE, TX 75401

EFFECTS TECHNOLOGY, INC
5383 HOLLISTER AVENUE
ATTN TECHNICAL INFO ACQ S CLOW
SANTA BARBARA, CA 93111

EG&G WASH. ANALYTICAL SVCS CTR, INC
2450 ALAMO AVENUE, SE
ATTN C. GILES
ALBUQUERQUE, NM 87106

ELECTRO-MAGNETIC APPLICATIONS, INC
ATTN FEDERICK ERIKSEN
ATTN RAY ROSICH
1978 S GARRISON ST
DENVER, CO 80226

ELECTRO-MAGNETIC APPLICATIONS, INC
PO BOX 8482
ATTN D. MEREWETHER
ALBUQUERQUE, NM 87198

FORD AEROSPACE & COMMUNICATIONS CORP
3939 FABIAN WAY
ATTN TECHNICAL LIBRARY
PALO ALTO, CA 94303

FORD AEROSPACE & COMMUNICATIONS CORP
FORD & JAMBOREE ROADS
ATTN K. ATTINGER
NEWPORT BEACH, CA 92663

FRANKLIN INSTITUTE
20TH STREET & PARKWAY
ATTN R. THOMPSON
PHILADELPHIA, PA 19103

GENERAL DYNAMICS CORP
ELECTRONICS DIVISION
PO BOX 81127
ATTN RESEARCH LIBRARY
SAN DIEGO, CA 92138

GENERAL DYNAMICS CORP
INTER-DIVISION RESEARCH LIBRARY
KEARNY MESA
PO BOX 80986
ATTN RESEARCH LIBRARY
SAN DIEGO, CA 92138

DISTRIBUTION (Cont'd)

GENERAL ELECTRIC CO
SPACE DIVISION
VALLEY FORGE SPACE CENTER
PO BOX 8555
ATTN J. ANDREWS
PHILADELPHIA, PA 19101

GENERAL ELECTRIC CO
AEROSPACE ELECTRONICS SYSTEMS
FRENCH ROAD
ATTN C. HEWISON
UTICA, NY 13503

GENERAL ELECTRIC CO
PO BOX 5000
ATTN TECHNICAL LIBRARY
BINGHAMTON, NY 13902

GENERAL ELECTRIC CO TEMPO
ALEXANDRIA OFFICE
HUNTINGTON BUILDING, SUITE 300
ATTN DASIAC
2560 HUNTINGTON AVENUE
ALEXANDRIA, VA 22303

GEORGIA INSTITUTE OF TECHNOLOGY
GEORGIA TECH RESEARCH INSTITUTE
ATTN R. CURRY
ATLANTA, GA 30332

GTE SYLVANIA, INC
189 B STREET
ATTN DAVID D. FLOOD
ATTN EMIL P. MOTCHOK
ATTN H & V GROUP, MARIO A. NUREFORA
ATTN J. WALDRON
NEEDHAM HEIGHTS, MA 02194

GENERAL RESEARCH CORP
SANTA BARBARA DIVISION
PO BOX 6770
ATTN TECHNICAL INFORMATION OFFICE
SANTA BARBARA, CA 93111

GEORGIA INSTITUTE OF TECHNOLOGY
OFFICE OF CONTRACT ADMINISTRATION
ATTN RES & SEC COORD FOR H. DENNY
ATLANTA, GA 30332

GRUMMAN AEROSPACE CORP
S OYSTER BAY ROAD
ATTN L-01 35
BETHPAGE, NY 11714

HARRIS CORPORATION
HARRIS SEMI-CONDUCTOR
PO BOX 883
ATTN V PRES & MGR PRGMS DIV
ATTN A. STRAIN
MELBOURNE, FL 32901

HAZELTINE CORP
PULASKI ROAD
ATTN J. OKRENT
GREENLAWN, NY 11740

HONEYWELL, INC
AVIONICS DIVISION
2600 RIDGEWAY PARKWAY
PO BOX 312
ATTN R. JOHNSON
ATTN S&RC LIBRARY
MINNEAPOLIS, MN 55440

HONEYWELL, INC
AEROSPACE & DEFENSE GROUP
13350 US HIGHWAY 19 SOUTH
ATTN S. GRAFF
ATTN W. STEWART
CLEARWATER, FL 33516

HORIZONS TECHNOLOGY, INC
7830 CLAIREMONT MESA BLVD
ATTN R. KRUGER
SAN DIEGO, CA 92111

HUGHES AIRCRAFT CO
ELECTRO-OPTICAL DATA SYS GP
PO BOX 902
ATTN CTDC 6/E110
ATTN J. SINGLETARY
ATTN K. WALKER
EL SEGUNDO, CA 90245

HUGHES AIRCRAFT CO
EL SEGUNDO SITE
PO BOX 92919
ATTN A. NAREVSKY
LOS ANGELES, CA 90009

HUGHES AIRCRAFT CO
GROUND-SYSTEMS GROUP
PO BOX 3310
ATTN K. DOWNING MLS 100
FULLERTON, CA 92634

IIT RESEARCH INSTITUTE
ELECTROMAG COMPATABILITY ANALCTR
N SEVERN
ATTN ACOAT
ANNAPOLIS, MD 21402

IIT RESEARCH INSTITUTE
10 W 35TH STREET
ATTN J. BRIDGES
ATTN I. MINDEL
CHICAGO, IL 60616

INSTITUTE FOR DEFENSE ANALYSES
1801 N BEAUREGARD STREET
ATTN TECH INFO SERVICES
ALEXANDRIA, VA 22311

DISTRIBUTION (Cont'd)

INTERNATIONAL TEL & TELEGRAPH CORP
500 WASHINGTON AVENUE
ATTN A. RICHARDSON
ATTN TECHNICAL LIBRARY
NUTLEY, NJ 07110

ION PHYSICS CORP
S BEDFORD STREET
ATTN H. MILDE
ATTN R. EVANS
BURLINGTON, MA 01803

IRT CORP
PO BOX 81087
ATTN B. WILLIAMS
ATTN N. RUDIE
SAN DIEGO, CA 92138

JAYCOR
SANTA BARBARA FACILITY
PO BOX 30281
360 SOUTH HOPE AVE
ATTN W. RADASKY
SANTA BARBARA, CA 93105

JAYCOR
PO BOX 85154
ATTN R. STAHL
ATTN E. WENAAS
SAN DIEGO, CA 92138

JAYCOR
205 S WHITING STREET
ATTN LIBRARY
ALEXANDRIA, VA 22304

KAMAN SCIENCES CORP
PO BOX 7463
ATTN W. RICH
ATTN A. BRIDGES
ATTN F. SHELTON
ATTN N. BEAUCHAMP
COLORADO SPRINGS, CO 80933

KAMAN TEMPO
816 STATE STREET (PO DRAWER QQ)
ATTN W. MCNAMARA
ATTN DASIAC
ATTN R. RUTHERFORD
SANTA BARBARA, CA 93102

LAWRENCE LIVERMORE NATIONAL LAB
PO BOX 808
ATTN TECHNICAL INFO DEPT LIBRARY
ATTN L-96, T. DONICH
ATTN L-153, D. MEEKER
ATTN L-156, E. MILLER
ATTN L-156, H. CABAYAN
ATTN L-10, H. KRUGER
LIVERMORE, CA 94550

LITTON SYSTEMS, INC
DATA SYSTEMS DIVISION
8000 WOODLEY AVENUE
ATTN MS 64-61/E EUSTIS
VAN NUYS, CA 91409

LITTON SYSTEMS, INC
AMECOM DIVISION
5115 CALVERT ROAD
ATTN J. SKAGGS
COLLEGE PARK, MD 20740

LOCKHEED MISSILES & SPACE CO, INC
3251 HANOVER STREET
ATTN TECHNICAL INFORMATION CENTER
PALO ALTO, CA 94304

LOCKHEED MISSILES & SPACE CO, INC
PO BOX 504
ATTN B. KIMURA
ATTN G. HEATH
ATTN S. TAIMUTY DEPT 81-74
ATTN H. THAYN
ATTN L. ROSSI
SUNNYVALE, CA 94086

LOS ALAMOS NATIONAL LABORATORY
PO BOX 1663
ATTN MS 670, J. MALIK
ATTN C. BENTON
ATTN MS 670, J. HOPKINS
ATTN B. NOEL
LOS ALAMOS, NM 87545

LUTECH, INC
PO BOX 1263
ATTN F. TESCHE
BERKELEY, CA 94701

MARTIN MARIETTA CORP
PO BOX 5837
ATTN M. GRIFFITH
ORLANDO, FL 32855

MARTIN MARIETTA CORP
PO BOX 179
ATTN D-6074 G. FREYER
DENVER, CO 80201

MCDONNELL DOUGLAS CORP
5301 BOLSA AVENUE
ATTN S. SCHNEIDER
ATTN TECHNICAL LIBRARY SERVICES
HUNTINGTON BEACH, CA 92647

MCDONNELL DOUGLAS CORP
3855 LAKEWOOD BOULEVARD
ATTN M. POTTER
LONG BEACH, CA 90846

DISTRIBUTION (Cont'd)

MISSION RESEARCH CORP
5434 RUFFIN ROAD
ATTN V. VAN LINT
ATTN J. CHERVENAK
SAN DIEGO, CA 92123

MISSION RESEARCH CORP
PO DRAWER 719
ATTN W. CREVIER
ATTN C. LONGMIRE
ATTN EMP GROUP
SANTA BARBARA, CA 93102

MISSION RESEARCH CORP
EM SYSTEM APPLICATIONS DIVISION
1400 SAN MATEO BLVD, SE, SUITE A
ATTN A. CHODOROW
ALBUQUERQUE, NM 87108

MISSION RESEARCH CORP
PO BOX 7816
ATTN W. STARK
ATTN J. LUBELL
ATTN W. WARE
COLORADO SPRINGS, CO 80933

MISSION RESEARCH CORP
ATTN B. COPLEN
5503 CHEROKEE AVE
ALEXANDRIA, VA 22312

MITRE CORP
PO BOX 208
ATTN M. FITZGERALD
BEDFORD MA 01730

NORDEN SYSTEMS, INC
PO BOX 5300
NORDEN PLACE
ATTN TECHNICAL LIBRARY
ATTN D. LONGO
NORWALK, CT 06586

NORTHROP CORP
ELECTRONIC DIVISION
2301 W 120TH STREET
ATTN LEW SMITH
ATTN RAD EFFECTS GRP
ATTN B. AHLPORT
HAWTHORNE, CA 90250

PACIFIC-SIERRA RESEARCH CORP
1456 CLOVERFIELD BLVD
ATTN L. SCHLESSINGER
ATTN H. BRODE, CHAIRMAN SAGE
SANTA MONICA, CA 90404

PALISADES INST FOR RSCH SERVICES, INC
201 VARICK STREET
ATTN RECORDS SUPERVISOR
NEW YORK, NY 10014

PHYSICS INTERNATIONAL CO
2700 MERCED STREET
ATTN DOCUMENT CONTROL
SAN LEANDRO, CA 94577

R&D ASSOCIATES
PO BOX 9695
ATTN DOCUMENT CONTROL
ATTN W. GRAHAM
ATTN C. MO
ATTN M. GROVER
MARINA DEL REY, CA 90291

R&D ASSOCIATES
1401 WILSON BLVD
SUITE 500
ATTN J. BOMBARDT
ARLINGTON, VA 22209

RAND CORP
1700 MAIN STREET
ATTN LIB-D
ATTN W. SOLLFREY
SANTA MONICA, CA 90406

RAYTHEON CO
HARTWELL ROAD
ATTN G. JOSHI
BEDFORD, MA 01730

RAYTHEON CO
528 BOSTON POST ROAD
ATTN H. FLESCHER
ATTN M. NUCEFORA
SUDBURY, MA 01776

RCA CORP
DAVID SARNOFF RESEARCH CENTER
PO BOX 432
ATTN D. OCONNOR
ATTN L. MINICH
PRINCETON, NJ 08540

ROCKWELL INTERNATIONAL
PO BOX 92098
ATTN B-1 DIV TIC
LOS ANGELES, CA 90009

ROCKWELL INTERNATIONAL CORP
PO BOX 3105
ATTN D/243-068, 031-0A31
ATTN J. ERB
ATTN V. MICHEL
ANAHEIM, CA 92803

ROCKWELL INTERNATIONAL CORP
SPACE DIVISION
12214 SOUTH LAKEWOOD BOULEVARD
ATTN B. WHITE
DOWNEY, CA 90241

DISTRIBUTION (Cont'd)

ROCKWELL INTERNATIONAL CORP
PO BOX 369
ATTN F. SHAW
CLEARFIELD, UT 84015

S-CUBED
PO BOX 1620
ATTN A. WILSON
LA JOLLA, CA 92038

SANDERS ASSOCIATES, INC
95 CANAL STREET
ATTN R. DESPATHY
NASHUA, NH 03060

SANDIA NATIONAL LAB
PO BOX 5800
ATTN T. MARTIN
ATTN G. YONAS
ATTN C. VITTITOE
ATTN R. PARKER
ATTN DIV 4365, E. HARTMAN
ALBUQUERQUE, NM 87185

SCIENCE APPLICATIONS, INC
PO BOX 2351
ATTN R. PARKINSON
LA JOLLA, CA 92038

SCIENCE APPLICATIONS, INC
2109 W CLINTON AVENUE
SUITE 800
ATTN N. BYRN
HUNTSVILLE, AL 35805

SCIENCE APPLICATIONS, INC
PO BOX 1303
ATTN W. CHADSEY
MCLEAN, VA 22102

SINGER CO
1150 MCBRIDE AVENUE
ATTN TECHNICAL INFORMATION CENTER
LITTLE FALLS, NY 07424

SPERRY RAND CORP
SPERRY MICROWAVE ELECTRONICS
PO BOX 4648
ATTN M. CORT
CLEARWATER, FL 33518

SPERRY RAND CORP
SPERRY DIVISION
MARCUS AVENUE
ATTN TECHNICAL LIBRARY
GREAT NECK, NY 11020

SPERRY RAND CORP
SPERRY FLIGHT SYSTEMS
PO BOX 21111
ATTN D. SCHOW
PHOENIX, AZ 85036

SPIRE CORP
PO BOX D
ATTN R. LITTLE
BEDFORD, MA 01730

SRI INTERNATIONAL
333 RAVENSWOOD AVENUE
ATTN E. VANCE
ATTN A. WHITSON
MENLO PARK, CA 94025

SYLVANIA SYSTEMS GROUP
COMMUNICATION SYSTEMS DIVISION
GTE PRODUCTS CORPORATION 77 "A" STREET
ATTN C. THORNHILL
ATTN L. BLAISDELL
ATTN J. CONCORDIA
NEEDHAM, MA 02194

SYLVANIA SYSTEMS GROUP
ELECTRONICS SYSTEMS & SERVICES
ORGANIZATION
GTE PRODUCTS CORPORATION
189 B STREET
ATTN A. NOVENSKI
ATTN E. MOTCHOK
ATTN C. RAMSBOTTOM
ATTN J. WALDRON
ATTN D. FLOOD
NEEDHAM, MA 02194

STRATEGIC SYSTEMS DIV
SYLVANIA SYSTEMS GROUP
GTE PRODUCTS CORP
1 RESEARCH CORP
ATTN I. KOHLBERG
WESTBORO, MA 01581

TEXAS INSTRUMENTS, INC
PO BOX 225474
ATTN TECHNICAL LIBRARY
ATTN D MANUS
DALLAS, TX 75265

TEXAS TECH UNIVERSITY
PO BOX 5404
NORTH COLLEGE STATION
ATTN T. SIMPSON
LUBBOCK, TX 79417

TRW ELECTRONICS & DEFENSE SECTOR
ONE SPACE PARK
ATTN W. GARGARO
ATTN L. MAGNOLIA

DISTRIBUTION (Cont'd)

TRW ELECTRONICS & DEFENSE SECTOR (Cont'd)
ATTN R. PLEBUCH
ATTN O. ADAMS
ATTN H. HOLLOWAY
ATTN E. HORGAN
REDONDO BEACH, CA 90278

TRW ELECTRONICS & DEFENSE SECTOR
BALLISTIC MISSILE DIV
PO BOX 1310
ATTN R. MORTENSEN, BLDG 527, RM 706
SAN BERNARDINO, CA 92402

UNITED TECHNOLOGIES CORP
HAMILTON STANDARD DIVISION
BRADLEY INTERNATIONAL AIRPORT
ATTN CHIEF ELEC DESIGN
WINDSOR LOCKS, CT 06069

VARIAN ASSOCIATES, INC
611 HANSEN WAY
ATTN H. JORY
PALO ALTO, CA 94303

US ARMY ELECTRONICS RESEARCH
& DEVELOPMENT COMMAND
ATTN TECHNICAL DIRECTOR, DRDEL-CT

HARRY DIAMOND LABORATORIES
ATTN CO/TD/TSO/DIVISION DIRECTORS
ATTN RECORD COPY, 81200
ATTN HDL LIBRARY, 81100 (2 COPIES)
ATTN HDL LIBRARY, 81100 (WOODBRIDGE)
ATTN CHAIRMAN, EDITORIAL COMMITTEE
ATTN TECHNICAL REPORTS BRANCH, 81300
ATTN LEGAL OFFICE, 97000
ATTN CHIEF, 22000
ATTN CHIEF, 22100
ATTN CHIEF, 22300
ATTN CHIEF, 22800
ATTN CHIEF, 22900
ATTN CHIEF, 13300
ATTN CHIEF, 21000
ATTN CHIEF, 21100 (5 COPIES)
ATTN CHIEF, 21200
ATTN CHIEF, 21300 (3 COPIES)
ATTN CHIEF, 21400 (3 COPIES)
ATTN CHIEF, 21500
ATTN CHIEF, 20240
ATTN TRIMMER, P., 22100
ATTN VALLIN, J., 22100
ATTN VRABEL, M. J., 21300
ATTN FAZI, C., 13500
ATTN DOBRIANSKY, B., 13500
ATTN MEYER, O. L., 22300
ATTN EDWARDS, A. 13500
ATTN WARD, A. L., (20 COPIES)